Calcification by amorphous carbonate precursors: Towards a new paradigm for sedimentary and skeletal mineralization

Dongbo Wang

Dissertation submitted to the faculty of the
Virginia Polytechnic Institute and State University
in partial fulfillment of the requirements for the degree of

Doctor of Philosophy in Geosciences

Committee
Patricia M. Dove, Chair
James J. De Yoreo
Michael F. Hochella Jr.
J. Fred Read
J. Donald Rimstidt

29 November 2010
Blacksburg, VA

Keywords: ACC, biomineralization, magnesium, calcite, dolomite,
non-classical crystallization, Raman spectroscopy

Calcification by amorphous carbonate precursors: Towards a new paradigm for sedimentary and skeletal mineralization

Dongbo Wang

Abstract

A new paradigm for the formation of calcified skeletons suggests mineralization proceeds through amorphous calcium carbonate (ACC) precursors. The implications of this strategy in carbonate crystallization are widespread, particularly for understanding factors controlling impurity and isotopic signatures in calcium carbonates. The first chapter is a literature review of the biomineralization processes used by two important model organisms: the sea urchin larva and the foraminifera. Sea urchin larvae provide a thoroughly studied example of mineralization by an ACC pathway that is under biological control through regulation of protein chemistry and the local mineralization environment. A review of how foraminifera produce their test structures is also examined to explore the question of how organisms regulate the Mg content in proportion to the temperature their environments of formation. The second chapter demonstrates that acidic biomolecules regulate the composition of ACC for a suite of model carboxylated molecules. The physical basis for the systematic trend in Mg content is related to the ability of the affinity of the biomolecule for binding Ca versus Mg. The third chapter builds on these findings to explore the transformation of Mg-rich ACC precursors to calcites of exceptionally high Mg-contents that could not be produced by classical step-dominated growth processes. The data indicate that these materials are likely a result of a nucleation-dominated pathway. The final, fourth chapter develops Raman spectroscopy-based calibrations for determining Mg contents in ACC. The calibrations are based upon peak position or peak width of the carbonate υ_1 stretch.

To Ge Ma

Acknowledgements

Please excuse the comprehensive acknowledgement section, but I firmly believe this work would not have been possible without the extensive help I have received from all of those below.

To my advisor, Prof. Patricia Dove, I could not have arrived at this point without your patience and dedication to my training. I came to Virginia Tech filled with curiosity, yet not prepared for serious scientific inquiry. Somehow through these years you have taught me to focus and finish what I start. I know that most would not have undertaken the task to shape another person into something useful. But, you accepted this challenge and remained committed to it. To this I owe so much. To Jim De Yoreo, thank you for giving me the freedom and the tools to explore the world of carbonate mineralization. I will forever cherish the time spent in your lab. To Mike Hochella, I am indebted to you for your belief in me. So many times I thought that I did not possess what it took to be an independent researcher and each time you convinced me otherwise. To Don Rimstidt, I am indebted for your guidance at a critical time, when I did not know how to continue my work on amorphous calcium carbonates. You helped lay the groundwork of this dissertation. Thank you for teaching me to think like a geochemist. To Fred Read, I am thankful for our continuing dialog about carbonates sediments, you have given me real grounding. To Jerry Gibbs, thank you for your encouragement. To Callie, none of this could have been possible or worthwhile without you. To Jonathan Lee and Yong Han, I cannot express my gratitude towards you for helping me start this work. To Adam Wallace I am so thankful that you have continuingly listened to my ideas and for the depth you have given them. I continue to cherish every interaction. To Takuya Echigo, I cannot express how much I have learned from you. My natural propensity is to paint with broad brushes, but through our collaboration I have learned the value of being careful and deliberate. To John McIntosh, thank you for our long discussions. Without your help, I could not have completed the third chapter of this dissertation. To Selim Elhadj, thank you for your guidance and continued encouragement. To Laura Hamm, thank you for reading my manuscripts and your willingness to engage me in new ideas. To Bob Bodnar, thank you for trusting me in your laboratory. To Charles Farley, thank you for all of your extensive help. To Deborah Aruguete, I have enjoyed our varied conversations; you have added depth to my research. To Nizhou Han, thank you for all your help and guidance. To Mitsu Murayama, thank you for giving me a real appreciation of the ‘nanoscale’. Thank you to Tony Guiffre, Laura Wasylenki and Allison Stephenson for your constant support and living with the ever-expanding mess on our bench tops. Thank you to the entire EIGER faculty, especially Brenda Winkel, George Filz, John Little, Jim Mitchell and Rosanne Foti. Thank you, to my mentors at the University of Colorado, John Drexler, Scot Douglass, Jimmy McCuthchan and Dennis VanGurven. Thank you to all the members of the Hochella group, in particular Bojeong Kim, Harish Veeramani and Andrew Madden for your continued scientific dialog. Thank you to all my friends at Tech and in Colorado: Nate Moore, Jenn Moore, Ryan McAleer, Beth McAleer, Nick Wigginton, Krista Rule Wigginton, Deric Learman, Sarah Learman, Mimi Wallace, Liz Drexler, Ryan Lester, Beth Diesel, Wade Mattox, David Chinn, Wendy Chinn, Amanda

Davis, Sher Vogel, Meredith Katz, Tuan Pham, Kristen Murphy, Philip Prince, Keith Ball, Lisa Tranel, Roger Bannister, Cory Pavicich, Jessica Minck, Ben Drexler, Andie Pliner, Tom Varani and Ross Wrangham. To my pastors, Mike Swann and Scott Russell, thank you for teaching me that this time spent at Virginia Tech was about more than research. Thank you to the wonderful Geosciences administrative and technical staff in particular Linda Bland, Ellen Mathena, Mary McMurray, Connie Lowe, Miles Gentry, Dan Smith and Richard Godbee, who have helped me with everything under the Sun and shown me real friendship. Thank you to my grandmother Ge Ma, my parents Sen and Hui and brother Michael who have been my continuous support.

Attributions

Prof. Patricia M. Dove (C.P. Miles Professor of Science, Department of Geosciences, Virginia Tech) was the research advisor and committee chair. She provided scientific guidance in experimental design, data collection, data analysis and writing. Furthermore, DOE and NSF grants awarded to Prof. Dove provided the financial support for this dissertation.

Dr. Adam F. Wallace (Post Doctoral Associate, Earth Sciences Division, Lawrence Berkeley National Labs) was a collaborator on the second chapter of this dissertation. He performed the *ab initio* calculations, provided scientific input on the laboratory experiments that were performed, along with contributions to the manuscript.

Dr. James J. De Yoreo (Associate Director, Molecular Foundry, Lawrence Berkeley National Labs) was a collaborator on the second chapter of this dissertation.

Dr. Takuya Echigo (Post Doctoral Associate, Department of Geosciences, Virginia Tech; Japan International Research Center for Agricultural Sciences, Tsukuba, Japan) was a collaborator on the third chapter of this dissertation. The XRD measurements could not have been performed with his help. He provided significant input on the interpretation of the data.

Prof. Mitsuhiro Murayama (Assistant Professor, Department of Materials Science, Virginia Tech) was a collaborator on the third chapter of this dissertation. He provided much assistance in collection of the XRD data along with TEM measurements.

Prof. Robert J. Bodnar (University Distinguished Professor, Department of Geosciences, Virginia Tech) was a collaborator on the fourth chapter of this dissertation, who provided much technical insight that made the measurements possible. It was his suggestion that standardized Raman could systematically be used to correct for spectrometer drift in the data found in chapter four.

Laura M. Hamm (PhD. Candidate, Department of Geosciences, Virginia Tech) was a collaborator on the fourth chapter of this dissertation and provided much assistance in the analysis and interpretation of the data.

Table of Contents

Table of Figures

Table of Tables

Introduction

In recent years, the scientific community has realized the extensive occurrence of reactive amorphous phases and their likely roles in regulating mineralization. These precursor phases are now recognized in carbonate, oxide, phosphate and protein mineralizing systems. The first conclusive observations of amorphous calcium carbonate (ACC) precursors were made less than fifteen years ago in studies of the calcified skeletal structures of eukaryotic organisms. Since that time, more than 750 published works (ISI Web of Science) have investigated the formation and structure of ACC in synthetic and biological systems. They demonstrate the importance of these phases in regulating the location, composition, and rates of carbonate mineralization. This dissertation develops a case for the importance of ACC in geological systems and begins to establish new geochemical principles for the fractionation of elements in the carbonate amorphous precursors and their crystalline products.

Chapter 1 is a literature review that considers the properties and roles of ACC in calcium carbonate skeletal formation of two model organisms, the sea urchin embryo and foraminifera. The goal is to present biological mineralization with a focus on skeletal formation in context of the overall organism. Findings from biological studies of the sea urchin embryo are used as an example of how organisms control mineralization by utilizing amorphous precursors. A discussion of foraminiferan test formation highlights the importance of understanding the physical basis for the elemental and isotopic signatures that are measured in these structures. Their signatures in the carbonate rock record are widely used as indicators of past environments.

Chapter 2 investigates the finding that acidic biomolecules regulate Mg content in ACC. A series of inorganic control experiments were conducted to establish the dependence of Mg/Ca ratios in ACC on solution composition. Then a suite of model carboxylated molecules, were selected based upon their relative binding affinities for Ca versus Mg. Molecules with a strong affinity for binding Ca compared to Mg promote the formation of Mg-enriched ACC (35-50 mol % $MgCO_3$) compared to the inorganic control. Measurements show Mg/Ca ratios are controlled by a predictable dependence upon the

binding properties of the organic molecules. The mechanism of incorporation is likely a cooperative effect between organic molecules changing the hydration environment of the Mg^{2+} and also altering local solution speciation. The findings reiterate the controls of microenvironment on mineralization and suggest an origin of compositional offsets, or vital effects in biominerals.

Chapter 3 establishes a new baseline for calcite formation from ACC precursors under geologically relevant Mg/Ca ratios (0-6). At relatively low Mg/Ca (1-3), transitory ACC particles are observed. Yet, calcite forms through the classical crystal growth process of step propagation as 'single' crystals of relatively large sizes (greater than 400 nm). Magnesium content of these crystals increases as a linear function of solution Mg/Ca. However, at higher solution Mg/Ca (4-6), the mineralization process undergoes an abrupt transition to a non-classical nucleation-dominated mechanism. ACC initially forms as a continuous sheet and later transforms into discs of aggregated nanocrystalline calcite. Crystalline end products are high Mg-calcites of dolomitic composition with approximately constant Mg contents (35-50 mol % $MgCO_3$) and sizes (30-80 nm) regardless of solution Mg/Ca. These findings suggest a physical basis for shifts in textures and patterns of calcification may be rooted in mineralization pathways and their dependence upon environmental conditions and could have major implications for interpreting ancient carbonates.

Chapter 4 describes a new Raman spectroscopy-based calibration for determining the Mg-content of ACC. Mg contents from 0 to 43 mol % can be estimated from a simple relationship based upon carbonate υ_1 peak position or to the peak full width at half maximum. This method provides a simple, direct and nondestructive chemical probe with small spatial resolution, sensitive only to ACC. Estimates of ACC composition using this method may be very useful when analyzing heterogeneous samples common in biological and environmental specimens.

Chapter One

Towards an Understanding of Calcium Carbonate Mineralization Pathways via an Amorphous Precursor: Insights from Sea Urchins and Foraminiferan

Dongbo Wang and Patricia M. Dove

Department of Geosciences, Virginia Tech, Blacksburg VA 24061 USA

Accepted for publication – as a part of A.F. Wallace, D. Wang, L.H. Hamm, A. Knoll, and P.M. Dove in Eukaryotic skeletal formation *Fundamentals of Geobiology*, edited by A. Knoll, D. Canfield, and K. Konhauser, Blackwell

1. Introduction

Over the last 540 million years organisms have developed the ability to control the precipitation of calcium carbonate skeletal components. Marine organisms live in well-defined marine ecosystems and their skeletal remains are thought of as faithful witnesses of past Earth environments. These biominerals remind us of simple chemical precipitates that have defined and understood chemical properties, highly suitable for geochemical analysis for understanding of paleo-environments. However, it is necessary to remember that carbonate skeletons are highly regulated, evolutionarily refined, and integral functional components of eukaryote organisms, whose properties are defined by the microenvironment within the organism, where they form. It is the purpose of this chapter to construct a more holistic picture of mineralizing organisms drawing on insights from intersecting fields of molecular biology, materials science, and geosciences. Researchers from across the disciplines have interests in mineralizing organisms, but each perspective is different. Molecular biologists are interested in calcium carbonate mineralizing organisms as models for interrogating the genetics and biochemistry of skeletal formation. Materials scientists use these organisms as examples of how morphologically; structurally and chemically tuned composite structures can be synthesized at room temperatures with simple proteins and small molecules. Geoscientists use these organisms and their preserved skeletons for reconstructing past environments.

Biomineralizing systems, though diverse and sophisticated, can be conceptualized into a simple model illustrated in **Fig 1.1**. At the heart of the system is a confined environment where mineral formation occurs. This environment's saturation state is controlled through active transport of ions or introduction of mineral precursors, which are regulated through genetic mechanisms. Also under genetic control is the expression and transport of biomineralization associated proteins, which are responsible for the initiation and regulation of mineral growth.

The classical understanding of crystal growth both in the laboratory and organisms has been based upon terrace-ledge-kink understanding of growth out of vapor pioneered by Burton et al. (1951). A new and developing picture from detailed *in vivo*

studies of organisms is quite different, as a generality controlled mineralization in organisms occurs in spatially confined environments that lack bulk water and crystallization occurs in a two-step process. The first step is the precipitation of a hydrated amorphous precursor that may contain large amounts of organic and inorganic impurities, which is followed by the transformation of the amorphous phase to the crystalline end product.

We will explore and elaborate on this new idea that crystallization in organisms occurs by an amorphous intermediate phase by examining two model organisms. We begin by reviewing sea urchin embryo development. Here, protein expression and use of amorphous precursors allow the organism to form a sophisticated calcite skeleton that behaves as a single crystal. Importantly this system has given significant insight into the crystallization process inside a living and intact organism. A clear understanding of the sea urchin embryo system provides a non-classical crystal growth model for how mineralization proceeds and is regulated from amorphous precursors. The second example is a unicellular model organism generally considered to utilize a simple biomineralizing system, the Foraminifera. These two were chosen because of their importance as in paleo-temperature reconstructions. A third discussion briefly follows on environmental proxies that are contained in corals.

2. The Sea urchins: Non-classical routes to $CaCO_3$ crystallization

Sea urchins, members of the phylum Echinodermata, hold remarkable promise for understanding cellular environments and the detailed chemistry and roles of their macromolecules during mineralization. Studies of sea urchins are motivated in part by their prevalence in the fossil record and the modern ocean, but again, efforts to interpret embedded compositional signatures for climate reconstruction are complicated by vital effects. From a biological point of view, spicule structure influences the shape, orientation and motility of larvae (PENNINGTON and STRATHMANN, 1990). Of particular interest in biomineralization studies are the factors that control the onset of spicule calcification and morphological development. Compared to most multicellular organisms, sea urchin larvae offer unique advantages to biomineralization research that include small physical size, short time scale for spicule development, ease for probing cellular processes by confocal microscopy, and relative ease of extracting spicule-

associated macromolecules (CHEERS and ETTENSOHN, 2005; WILT, 1999; WILT and ETTENSOHN, 2007; WILT, 2002; WILT et al., 2003). Here we consider how the organism develops in tandem with spicule mineralization.

2.1 Embryo development

The process of embryo development involves the synchronous formation of the organism and its skeleton. Upon fertilization, the cell quickly divides; at the 16-cell stage an unequal equatorial division results in small cells at the vegetal pole, called large micromeres. These specialized cells are ultimately responsible for controlling mineralization within the larvae (SUMMERS et al., 1993). Cell cleavage ends at the 128-cell stage when the cells reorganize to form the blastula, a hollow sphere of cells with a central cavity. During blastula formation, 16 or 32 descendents of the large micromeres are incorporated into the epithelial wall and undergo a round of cell division resulting in groups of 32 or 64 cells (TAKAHASHI and OKAZAKI, 1979). In the mid-blastula phase the large micromeres ingress into the vegetal pole of the central cavity, and are subsequently known as Primary Mesenchyme Cells (PMCs). While the PMCs are reorienting, the simultaneous invagination of the embryo results in gut formation. During this stage of development the PMCs organize into two clusters and form protrusions that fuse to form a network known as the syncytium (**Fig 1.2**), which is where mineral formation occurs (WOLPERT and GUSTAFSON, 1961). It is within the two syncytia that the initial calcite deposits appear as tri-radiate spicule rudiments. As the larvae mature into the pluteus stage, the two spicule rudiments continue to elongate along the symmetrically equivalent directions parallel to [100] (OKAZAKI and INOUE, 1976; WOLPERT and GUSTAFSON, 1961).

2.2 Primary mesenchyme cells: Directors of spiculegenesis

PMCs receive ectoderm-derived signals that regulate the synthesis of proteins directly related to spiculogenesis and also allow for the cell to cell fusion that forms the syncytial networks (ARMSTRONG et al., 1993; GUSS and ETTENSOHN, 1997; HODOR and ETTENSOHN, 1998). These signals also direct PMCs to reorient during spiculogenesis, which influences the morphology of growing spicules (MALINDA and ETTENSOHN, 1994; WOLPERT and GUSTAFSON, 1961). Through protein labeling methods, Wilt et al. (2008) demonstrated that spicule-associated proteins produced and excreted by PMCs do not

travel more than 5-10 μm within the syncytium, indicating that the local crystallization environment is strongly influenced by protein regulation within nearby PMCs. PMCs apparently carry out all tasks related to spiculogenesis in the urchin embryo by producing an extra-cellular site for mineral deposition, supplying the growing spicule with calcium carbonate, and producing and transporting proteins necessary for controlling mineral growth.

In the initial phase of mineral deposition, the syncytial network forms a microenvironment that is conducive to the nucleation and growth of crystalline calcium carbonate. Ultrastructural studies indicate that the synctium and the central cavity are interconnected; introduction of calcium chelators and low pH conditions results in spicule dissolution (DECKER et al., 1987). Beniash et al. (1999) carefully characterized this environment and found conclusive evidence that at most there could be 2-4 nm of solution between the sheath and the crystalline component. Incidentally, this thickness correlates with the amount of water that would condense on a calcite surface in a humid environment (CHIARELLO et al., 1993), perhaps giving a clue for an analogous environment.

2.3 Integral spicule matrix proteins

To develop a rigorous model for biomineralization in sea urchin embryos, it is necessary to understand the role of PMC synthesized proteins in the synctium, since they are likely responsible for stabilizing amorphous precursors to crystalline calcium carbonate (ACC), and initiating calcite nucleation. The first step towards this end is to differentiate those proteins involved in biomineralization from those with other functions in the cell. The traditional method has been to study those proteins directly associated with the spicule (AMEYE et al., 2001; AMEYE et al., 1999; KILLIAN and WILT, 1996; KITAJIMA and URAKAMI, 2000; SETO et al., 2004; URRY et al., 2000). However, it is known that there are membrane proteins that may serve as substrates for crystal formation that are not contained within spicules (CHEERS and ETTENSOHN, 2005). The function(s) of specific proteins within a cell or organism are generally determined by employing strategies to knockout or suppress the expression of the gene(s) that code for the proteins of interest. For eukaryotes, development of this technology can be a challenging process. To meet this need, a new loss of function tool has been utilized,

Morpholino Oligos (MO), which can block mRNA translation in specific genes and effectively inhibit protein synthesis (HEASMAN, 2002); when introduced to cells at the proper stage. When applied to sea urchin embyos these tools clarify the function of certain proteins in spiculegenesis (CHEERS and ETTENSOHN, 2005; PELED-KAMAR et al., 2002).

The main goals of studies on spicule-associated proteins have been to characterize their structural and physical properties, their localization in both PMCs and the spicule, and their effects on the growth of the spicule in vivo. Killian and Wilt (1996) used 2D-gel electrophoresis to identify 40-45 proteins associated with urchin spicules. The majority of these proteins (35 out of 45) is acidic (with isolelectric points below 6.0), and contain large quantities of Asp/Asn and Glu/Gln amino acid residues. The remaining ten proteins are basic in nature. Within the basic group, five proteins SM50, SM37, SM32, SM29, and PM27, have been characterized, of which SM50 and PM27 have been the focus of most investigations (HARKEY et al., 1995; ILLIES et al., 2002; LEE et al., 1999; LIVINGSTON et al., 2006; ZHU et al., 2001). These proteins are abundant in the extra-cellular matrix and on the surface of the spicule (KITAJIMA and URAKAMI, 2000; SETO et al., 2004; WILT et al., 2008). MO knock-out experiments show that spicule elongation is not observed in the absence of SM50 (PELED-KAMAR et al., 2002) which strongly indicates that SM50 plays an integral role in directing spicule growth along the <100> directions (KITAJIMA and URAKAMI, 2000). Wustman et al. (2002) suggested that a glycine loop motif found in PM27 may play a role in altering the mechanical properties of the carbonate spicule, as suggested by Berman (1988) and Berman (1990).

From the acidic group, the glycosylated SM30 protein (and its derivatives) has been characterized, revealing the presence of a highly conserved C-type lectin calcium-binding motif (LIVINGSTON et al., 2006). Investigations with immunogold protein labeling and green fluorescent protein tagged SM30 mutants show that these proteins are a major component of the spicule-associated protein assemblage (KITAJIMA and URAKAMI, 2000; SETO et al., 2004; WILT et al., 2008), suggesting that SM30 promotes elongation in the c crystallographic direction. However, some have suggested that its main function is to make the spicule more resistant to cleavage or fracture (WILT and ETTENSOHN, 2007).

The discovery of P16 represents a new mode of discovering biomineralization related proteins, because it was found with a complementary DNA (cDNA) library which was used to screen proteins that are up-regulated within the PMCs during spiculegenesis rather than by traditional protein purification methods (ILLIES et al., 2002). Subsequent MO investigations show that PMC function remains normal when P16 expression is suppressed, but spicule elongation does not occur. Its precise chemical role in the mineralization process is, however, not known (CHEERS and ETTENSOHN, 2005). P16 is a small protein 16kD (172 residues) that includes a glycine, aspartic acid-rich domain, a transmembrane domain and short C-terminal domain and has a predicted isoelectric point of 3.6 (ILLIES et al., 2002).

2.4 Development of the spicule and lessons for the future of biomineralization

There is convincing evidence that spicule formation proceeds through a metastable disordered calcium carbonate phase (ACC) en route to the final crystalline product, rather than by direct nucleation of calcite from solution. The resulting calcite spicule contains about 5 mole percent Mg and 0.1% organic material (OKAZAKI and INOUE, 1976). Under optical crossed nichols, spicules behave as a single crystals, however studies using synchrotron-based XRD suggest a reduction in the coherence length of the signal, which implies the presence of oriented micro crystals that may be held in place by organic material localized at grain boundaries (BERMAN et al., 1990; BERMAN et al., 1988; BERMAN et al., 1993). Beniash et al. (1997) reports that the triradiate spicule rudiments isolated from developing larva contain significant amounts of ACC. Furthermore, Politi et al. (2006) conclusively demonstrated with X-ray absorption spectroscopy that the initially deposited tri-radiate spicules were up to 90% ACC, and that the ACC to calcite ratio decreased at more advanced stages of larval development. Politi et al. (2008) have mapped similar spicules at up 40 nm resolution using X-ray photoelectron emission spectromicroscopy. They demonstrated that there are three phases present in the developing spicules, one very similar to crystalline calcite and two forms of ACC. The first is a hydrated ACC very similar to the synthetic form, that is only present in fast growing regions, which transforms to the second, which is a disordered, un-hydrated phase that subsequently transforms into calcite. These results may suggest that crystallization in these systems may occur in two steps, first starting as a fully amorphous

and hydrated material then transforming to an un-hydrated and more ordered phase before finally transforming to a fully crystalline phase. There is similar evidence demonstrating that this strategy is generalized in the sea urchin, as researchers have made similar observations in both adult spines (POLITI et al., 2004) and teeth (NUDELMAN et al., 2007). To understand the source of an ACC precursor phase, researchers have looked for physiological structures in PMCs that are responsible for calcium and carbonate storage. Decker et al. (1987) found electron dense granules around the nucleus and suggested that these granules are necessary to support the mineralization process. Beniash et al. (1997) later confirmed this finding by identifying the granules in TEM sections of PMCs. In a more recent study, Wilt et al. (2008) stained these granules with a fluorescent calcium binding molecule, calcein and demonstrated that the PMCs actively concentrate ACC in vacuoles and most likely transport them to the sites of mineralization, in the synctium. These biologically oriented studies are leading to a more detailed picture of calcium carbonate biomineralization in which non-classical crystal growth mechanisms are central. The nature of the ACC to calcite transformation remains controversial because the physical and chemical conditions in vivo are substantially different from those that have been employed in classical studies of calcite nucleation and growth. New experimental approaches need to be developed to explore the effects proteins, low water activity, and spatial confinement on crystal growth, that more closely replicate biological conditions. Moreover, additional work is required to more accurately determine the roles matrix proteins in vitro (ELHADJ et al., 2006; FU et al., 2005; GAYATHRI et al., 2007; PIANA et al., 2007).

3. The Foraminifera: Chemical signatures as paleoenvironmental indicators

Foramanifera comprise one of the most diverse groups of microscopic protists in the modern ocean. Many of these protozoans, members of the eukaryotic superkingdom Rhizaria, develop a variety of carbonate biominerals as shells, or tests. Of the 15 formainiferal orders recognized by the micropaleontological community, seven are capable of secreting calcite exoskeletons (ARMSTRONG and BRASIER, 2006; SEN GUPTA, 1999). Others mineralize aragonite and opaline silica, and two groups can assemble foreign particles into tests using carbonate or organic matter as cements. Early

foramanifera did not form mineralized skeletons and their lack of preservation has likely skewed older models of how these organisms evolved over deep time. However, with the emergence of techniques that combine molecular and fossil data, new studies suggest a significant radiation of non-skeletonized forms that eventually gave rise to the wide variety of forms recognized today (PAWLOWSKI et al., 2003). Rhizarian microfossils in 750 million year old rocks support the phylogenetic inference that forams began to diversify well before their Cambrian appearance as fossils.

Because they combine large population sizes, excellent preservation, well-understood environmental distributions, and rapid evolutionary turnover, foraminferans have long been the focus on paleo-environmental research, especially for Cenozoic oceans (e.g. (SEN GUPTA, 1999). These remarkable organisms occur in both planktonic and benthic settings, enabling them to document conditions throughout the water column in ancient oceans. Moreover, aspects of their test chemistry record ambient environments at the time and place of mineral precipitation. Over the last decade, an ever-increasing variety of compositional signatures have emerged that can be correlated with or calibrated to the formation environment (e.g. **Table 1.1**). In particular, a significant effort has been directed at using the tests of calcifying forams to quantify relationships between stable isotopes and/or trace elements and the paleo-chemistry of marine water masses. For example, δO^{18} and Mg contents have been used to determine simultaneously the temperature and salinity of past oceans (LEA, 2006; LEAR et al., 2000). A number of field and laboratory studies show that the Mg/Ca ratio in foram tests can faithfully record paleotemperatures of the oceans (ANAND et al., 2003; LEA, 2006; LEA et al., 1999; LEAR et al., 2000; LEAR et al., 2002; NURNBERG et al., 1996; ROSENTHAL et al., 1997; TOYOFUKU et al., 2000). As discussed later, however, there are significant caveats to making the recognized proxy models more robust and to testing the many new proxies that are being introduced in current literature.

3.1 Mineralization of calcareous tests

Extensive in vivo observations suggest that the mineralization strategies employed by foraminifera should allow these organisms to serve as faithful indicators of the ambient conditions during test formation. In particular, some forams undergo mineralization by processes that, at least in part, i) utilize classical nucleation and growth

processes; and ii) use captured seawater as starting material for the calcification process (EREZ, 2003). From biological studies, Erez and colleagues have developed a model for the stepwise mineralization of foram tests— a process called "seawater vacuolization" (J. Erez, pers. comm.). As seen in **Fig 1.3 ABC**, mineralization begins when the organism extends a pseudopod to form a delimited or compartmentalized space that engulfs ambient seawater. From this packet of solution, calcification occurs on the compartment walls as a thin layer that eventually becomes a new test chamber while also overgrowing onto the mineral surfaces of preexisting chambers (EREZ, 2003).

At first glance, this simple vacuolization process would seem to be a straightforward mineralization model for eukaryotes. However, numerous species are known to produce tests that are depleted in Mg to levels significantly below those expected for mineralization from seawater as well as variations within single species (SEGEV and EREZ, 2006). This variability suggests that biological factors must be active and is evidence that mineralization cannot simply be a passive reflection of seawater chemistry at the time of entrapment. Clearly, there is an ongoing need to assess whether/when forams begin to modify the composition of the seawater packet after the compartment is formed. For example, the organism could modify: i) local chemical conditions at the site of mineralization (local pH, supersaturation, rate of precipitation); ii) supply or removal of ions via channels and pumps; iii) selective reaction with organic macromolecules, including proteins, polysaccharides, or other organic matrix components; or iv) mineralogy, texture and/or preferred orientation of crystals in the developing mineralized structure. The simple model in **Fig 1.4** (EREZ, 2003) illustrates how biological processes can significantly modulate the local chemistry. In particular, acidic vacuoles supply CO_2 to the symbionts found in many foram species and to the basic vacuoles contained within the organism, thereby influencing pH and superaturation that, in turn, could affect trace element contents. Moreover, assuming that the system is a semi-closed environment, this results in a CO_2 competition that could also influence isotopic fractionation. Investigations of the in vivo environment is a critical research area that is poised to advance rapidly with new microelectrode techniques to measure pH and ion activities within these micro-compartments. Coupled biological-chemical models such as **Fig 1.4** suggest that key variables such as pH and ion activities likely vary

significantly over length scales of just a few microns. Given that microelectrode measurements were used to constrain this physical picture, it would seem this model merits further testing. This kind of knowledge will be essential to establishing a robust understanding of mineralization processes in vivo.

3.2 Decoupling vital effects from true environmental signatures

New studies of foram mineralization processes have rejuvenated interest in the long-recognized problem of 'vital effects' and their influence on trace element and isotopic signatures. The concept of the vital effect was first introduced by (UREY et al., 1951) to explain why oxygen isotopes measured in echinoderm shells depart from temperature curves calibrated for inorganically precipitated carbonates. Urey and colleagues described these deviations as 'physiological offsets' that likely had both 'kinetic' and 'taxonomic' origins (EPSTEIN and LOWENSTAM, 1954; MCCREA, 1950; WEBER and RAUP, 1966). Despite the fact these offsets were found in many subsequent studies of isotopic and elemental signatures, the difficulty of interpreting this complicating factor has been largely 'swept under the rug.' By necessity, researchers have selected species that were the most faithful recorders of the environments in which they formed or, worse, proposed new proxies that simply ignore the potential for significant biological overprinting (WEINER and DOVE, 2003). Over the last few years, efforts have become refocused toward understanding how mineralization processes occur and, hence, how the inherent biochemical/biological bias in measured chemical signatures originates. This holds the long-term promise of converting vital effects from nuisances to sharper tools in paleoenvironmental reconstruction (WEINER and DOVE, 2003). Here we highlight examples from recent studies of foram mineralization that are leading the way toward sorting out the physiological processes that give rise to vital effects.

As noted above, Foraminifera display a large variability in the Mg content of their tests. Species can contain from near-zero to almost 20 mol% $MgCO_3$, with significant deviations from Mg/Ca ratios expected for inorganically formed calcite (BENTOV and EREZ, 2006; SEGEV and EREZ, 2006). These variations are reported for different species from the same environment as well as for individual shells that are themselves are highly heterogeneous. Until recently, only a few studies (DELANEY et al., 1985) had

unambiguously determined if this variability could be attributed solely to species-specific differences or if it was a true an indicator of the ambient chemical and thermal conditions. Recent culturing studies such (HINTZ et al., 2006; RUSSELL et al., 2004) have been particularly useful in assessing this kind of question for Mg as well as other elemental and isotopic signals. Similar questions extend to whether latitudinal differences could also influence Mg/Ca dependencies for paleotemperature reconstructions. For example, Von Langen (2005) showed that temperate and polar foraminiferans have similar Mg/Ca temperature calibration equations but with a considerable offset in the pre-exponential constant. Similarly, parallel ship-board studies are critical to testing and validating assumptions that underlie reconstruction models of sea surface temperatures to constrain models for climate periodicities (LEA et al., 2005; LEAR et al., 2002; MEDINA-ELIZALDE and LEA, 2005; MEDINA-ELIZALDE et al., 2008; WALDEAB et al., 2007) and habitat migration (EGGINS et al., 2003).

With so many factors at play, a concerted effort to discern first and second order controls must include novel approaches to studying foram mineralization. At this writing, new in vivo studies are revealing mechanism-based explanations for Mg signatures to be complex. Even for the relatively simple forams, multiple mineralization processes may be involved. For example, Bentov and Erez (2005) showed that tests of the perforate foram Amphistegina lobifera are a composite of two types of calcite: a thin high Mg primary layer (1-10 microns) and thicker low-Mg layers (3-35 microns) that cover both sides of the primary layer. The high Mg layer (up to 20 mol% $MgCO_3$) is associated with an organic matrix, consistent with the idea that this type of calcite is formed via an amorphous intermediate (RAZ et al., 2000). The idea that forams may use multiple pathways to calcite crystallization in such close temporal and physical proximity raises the question of whether there is a general relationship between high and low Mg-calcites and non-classical versus classical mineralization processes, respectively. Different processes could explain aspects of the reported heterogeneity in foram shells, their different temperature dependencies, and possibly aspects of the vital effect. Bentov and Erez (2006) have assembled what may be the most comprehensive roadmap available to uncover the factors that regulate foram mineralization and the origins of vital effects. Recognizing the significance of their finding that forams employ the multiple

mineralization processes discussed above, Bentov and Erez synthesized available data to emphasize influences on Mg signatures that merit further investigation (**Table 1.2**). Electron microprobe analyses of bulk tests from *Amphistegina lobifera* and *A. lessonii* support the idea that a physiological mechanism must exist to exclude or reduce the activity of Mg at the site of calcification or within the compartment that is created by their pseudopods (SEGEV and EREZ, 2006). Support for physiological influence is found in measurements showing that biogenic calcites do not incorporate Mg in similar proportion to inorganically grown calcite crystals (WASYLENKI et al., 2005). Perhaps these foram species optimize skeletal growth at the lower Mg/Ca characteristic of seawater for much of the Cenozoic Era (HARDIE, 1996) and have evolved pathways to remove Mg from the engulfed packet of solution. Possible processes include passive membrane transport systems for Mg diffusion (PRESTON, 1998) chemical buffering with ATP binding reactions (ROMANI and MAGUIRE, 2002), and sequestration by nearby organelles (BENTOV and EREZ, 2006). A second mode of controlling Mg levels in foram shells is through the activity of an organic matrix. Macromolecules of polysaccharides, carboxyl-rich peptides and proteins are known to influence carbonate polymorph (KOTACHI et al., 2006; LEVI et al., 1998; WADA et al., 1999; XU et al., 2008), mineralization processes (Raz et al., 2000) and Mg partitioning into crystallographically unique faces (DAVIS et al., 2004; LOWENSTAM and WEINER, 1989; STEPHENSON et al., 2008; WASYLENKI et al., 2005). Again, the highest Mg calcites (before diagenesis) are clearly and intimately associated with the organic matrix, particularly the first layer that begins as an amorphous transient phase and will subsequently form a new chamber (**Fig 1.3 D**).

Mention of an amorphous precursor brings us to the third aspect of understanding how organisms influence the signals of elemental and isotopic signatures. It is important to note that this alternative pathway has implications for understanding chemical signatures. After all, if bulk shell composition indeed reflects multiple crystallization processes, then it follows that interpretations of composition must make assumptions about the signals contained in the calcite produced by each process. **Table 1.2** shows how variations in the relative quantities of each type of calcite produced for an individual test chamber can account for some of the reported intra-shell variability. To answer these

questions, we point again to the need to understand underlying chemical processes. Finally, the less glamorous but nonetheless critical roles of in vivo pH and the coupled $CO_3^=$ chemistry are critical to determining the chemical driving force for mineralization within the organism. While pH control on mineralization is known, some evidence also suggests Mg levels are influenced by pH (RUSSELL et al., 2004). At this writing, it is clear that we have only first glimpses of how organic chemistry influences the formation and chemical properties of inorganic components in foram shells. The new in vivo evidence, however, suggests that we are entering an exciting time of rapid advances.

4. Mineralization from seawater: Insights for elemental signatures in corals?

I will not develop a full discussion of coral mineralization, but we would be remiss to not mention these important animals. In some parts of the world, corals have a significant impact on carbon chemistry. Approximately 40% of net oceanic $CaCO_3$ precipitation occurs in tropical areas along coastal zones where coral reefs predominate (GATTUSO et al., 1998), but in recent years, ocean acidification has been severely decreasing their productivity (BELLWOOD et al., 2004). Unlike planktonic organisms whose carbonate products are largely recycled on short time scales, the corals sequester carbonate for long periods. Corals are also considered good recorders of ocean chemistry because their calcification process is based upon capturing seawater and bringing it to the site of mineralization (SILVERMAN et al., 2007a; SILVERMAN et al., 2007b).

Despite marked differences in overall biology, corals and forams share number of common features in calcification. Analogous to the pseudopods of forams, corals are believed to utilize a tissue pumping mechanism to capture seawater and create a locally supersaturated area while possibly modifying compositions of intracellular fluids. In particular, recent evidence suggests that, like forams, corals shift the pH of captured seawater to values well above 8 (AL-HORANI et al., 2003; COHEN and MCCONNAUGHEY, 2003; SCHNEIDER and EREZ, 2006). By creating a local calcification environment analogous to the semi-closed system utilized by forams, it is possible that corals also influence chemical signatures of resulting minerals (COHEN and MCCONNAUGHEY, 2003; RAZ-BAHAT et al., 2006). Finally, corals produce biomineral structures with different levels of trace elements suggesting that, again, multiple crystallization pathways may be involved. (MEIBOM et al., 2008; MEIBOM et al., 2006) have shown that isotopic and trace

element (including Mg and Sr) abundances differ between center of calcification (the earliest aragonite, precipitated on an organic template) and an enveloping coat of fibrous aragonite. As in the case of forams, this suggests that bulk chemical analyses may record a mixing line between two distinct mineralization processes. And, again, as in forams, the intertwined roles of symbionts are part of the picture, at least for reef-forming hermatypic corals. In vivo approaches that include tracer and microelectrode methods are certain to shift research of corals from a descriptive to mechanism-based understanding.

5. Summary

In this chapter, mineralization by two eukaryotic model organisms has been described. Using the sea urchin embryo we developed a detailed account of non-classical crystal growth in organisms. Sea urchin embryo spicule genesis is not a simple precipitation process, but rather a carefully regulated system, which controls the site of mineral deposition, formation and transport of amorphous precursors and expression of proteins that modulate mineral growth and morphology. Future investigations will undoubtedly unravel the precise roles of proteins in directing the transformation of the amorphous precursor to the crystalline end product. Complementary characterization of the deposited biominerals will likely yield information on the mechanism of the ACC to calcite transformation in a confined cellular environment. Also of importance are the chemical and isotopic signatures that can be derived from skeletal fossils. It is through these signatures that past environments can be revealed; yet our interpretation is wholly dependent on our understanding of the mechanisms of mineralization that occur *in vivo*.

Our current mechanistic understanding of Mg/Ca signatures in biogenic calcium carbonates is based on classical crystal growth, and synthetic calcium carbonates grown in this manner are known to be much different than their biogenic counterparts. It is likely formation pathway is responsible. If we are to extend our understanding of chemical signatures in biogenic carbonate the effect of the amorphous precursor pathway on the Mg/Ca ratio of calcites must be measured. There are three defined tasks to understand this phenomenon. 1) What are the possible Mg/Ca ratios contained in the amorphous phase and how organics can alter that signal? 2) What are the conditions that would cause ACC to transform to calcite that replicates the *in vivo* system? It is well

documented that amorphous calcium carbonates form in high driving force systems, yet the transformation to calcite is very clearly dissolution/re-precipitation in the bulk solution, which is not case *in vivo*. 3) What is the Mg/Ca signature that results from a true ACC to calcite transformation?

Table 1.1. Summary of tracers and proxies being used in paleooceanography based upon signatures in carbonate skeletons.

Mg/Ca	Paleo-temperature, paleo Mg concentration
Cd/Ca	Paleo-phosphate, paleo-ocean circulation
Ba/Ca	Paleo-alkalinity, paleo-ocean circulation
U/Ca	Redox potential and paleo CO_3^{2-}
V/Ca	Redox potential
SO_4^{2-}/CO_3^{2-}	Paleo CO_3^{2-}
$\delta^{11}B$	Paleo pH
$\delta^{13}C$	Paleo-productivity, paleo-ocean circulation
$\delta^{18}O$	Paleo-isotopic composition of seawater, paleo-temperature
$\delta^{44}Ca$	Calcium concentration, temperature, possible biomineralization pathway
$\delta^{24,25,26}Mg$	Paleo-temperature
$\delta^{88}Sr$	Salinity, chemical weathering rates

Table 1.2. Summary of possible mechanisms for controlling Mg:Ca ratio in foram tests (BENTOV and EREZ, 2006).

Cellular controls on Mg composition by regulating chemistry of the parent solution
Transport systems that allow passive-Mg diffusion
Cellular buffering by ATP binding
Sequestration within cellular organelles, mitochondria
Possible influence of the organic matrix on the mineralization process
Polymorph selection
Incorporation of impurities and trace elements
Selective development of crystal facets
Skeleton growth by classical and nonclassical crystallization pathways
Deposition of amorphous transient phase and transformation process favors high Mg
Ion by ion growth may limit maximum Mg uptake
Proportions of these processes may affect intrashell variability

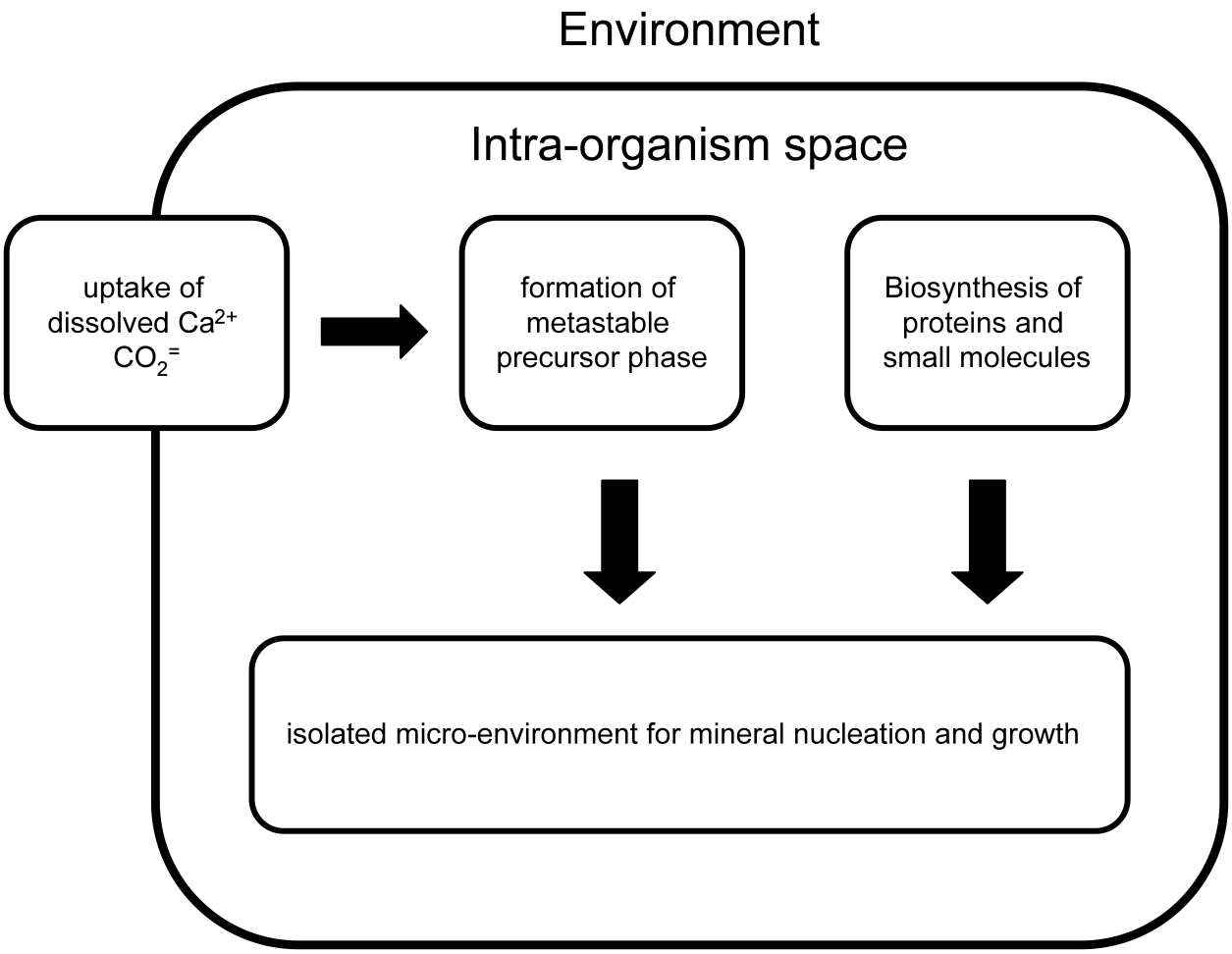

Figure 1.1. Elements of active mineralization strategies employed by eukaryotic organisms. Elucidating the molecular level details of these processes, the interplays amongst them, and their interactions with the surrounding genetically-controlled environment are the main objectives of biomineral research.

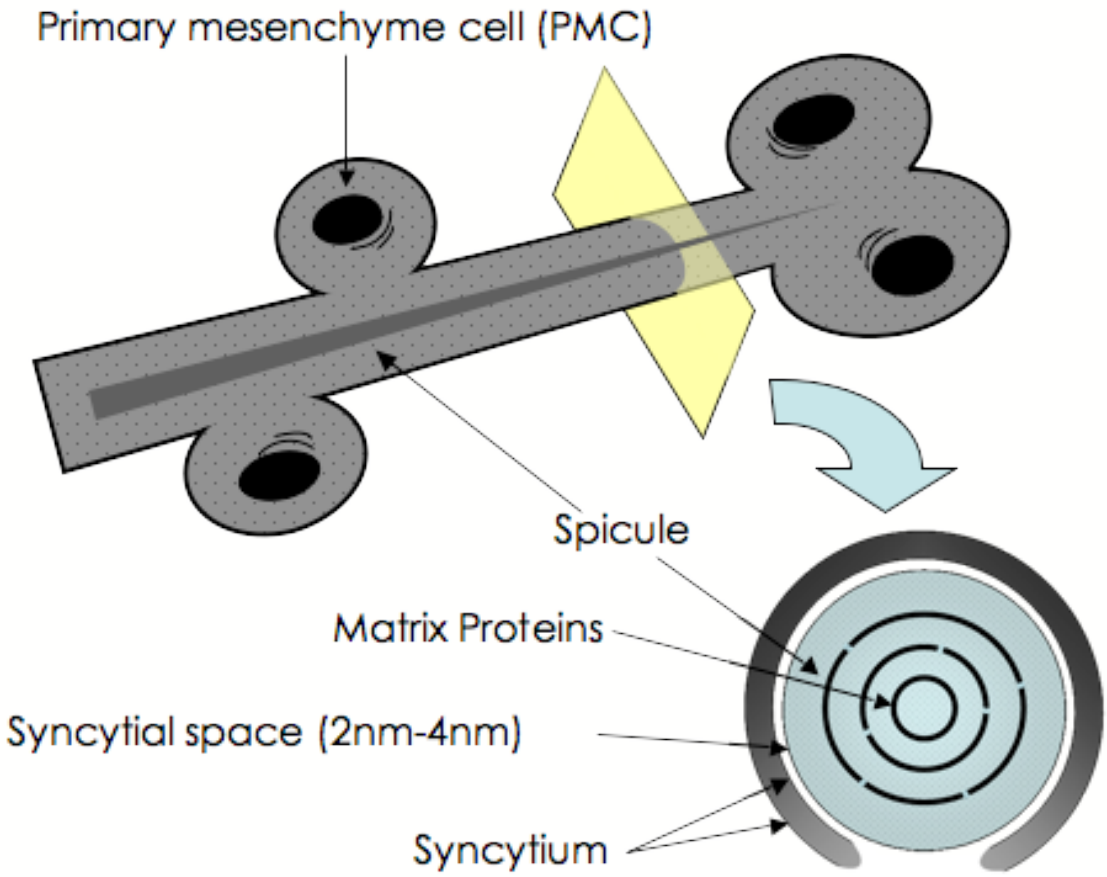

Figure 1.2. A schematic representation of the depositional environment of the larval spicule, where water can only exist as a thin film (2-4 nm). The spicule develops from calcium carbonate and proteins transported to the growing spicule from the primary mesenchyme cells (PMC). Matrix proteins like SM50 and SM30 are incorporated into the spicule. After WILT (1999).

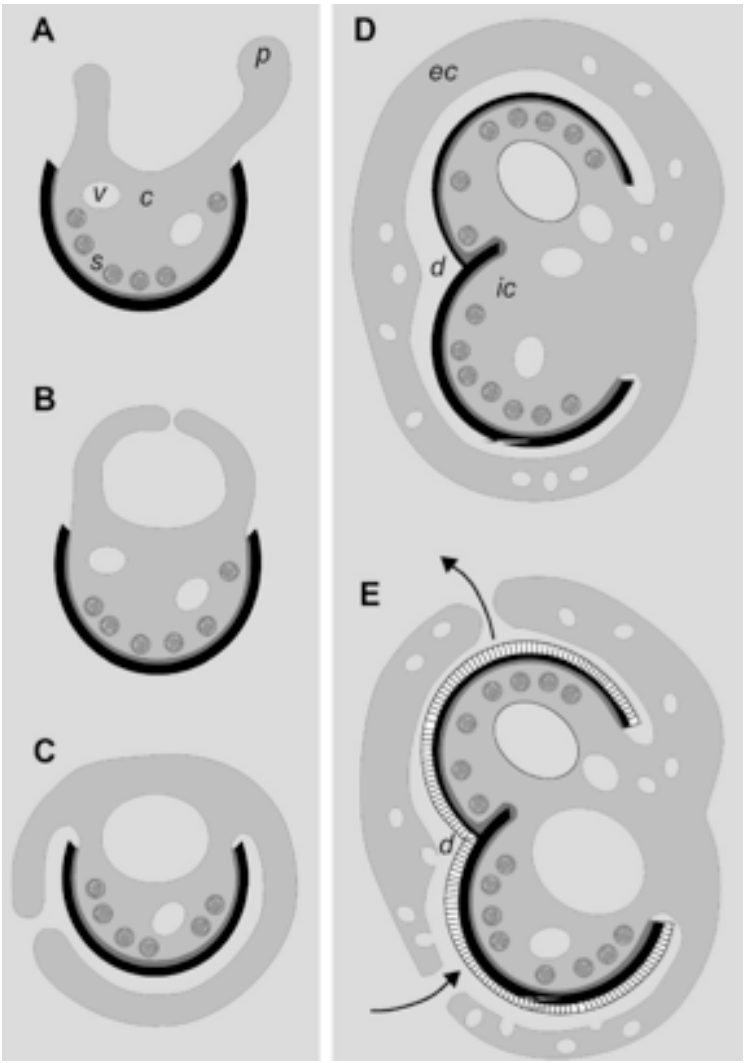

Figure 1.3. Stepwise model for calcification by perforate foraminifera. **a)** The process begins when pseudopods extend into the surrounding seawater, creating **b)** an enclosed compartment of seawater for mineralization. **c, d)** Portions of the calcified test can also act as templates for mineral deposition through a similar process whereby pseudopods form seawater filled compartments around preexisting mineral chambers. Evidence suggests mineralization within these compartments proceeds by accumulation of an amorphous CaCO3 phase that subsequently transforms to calcite; **e)** seawater flux through a compartment creates chemical conditions to thicken overgrowths as a secondary layer, likely by classical mineralization

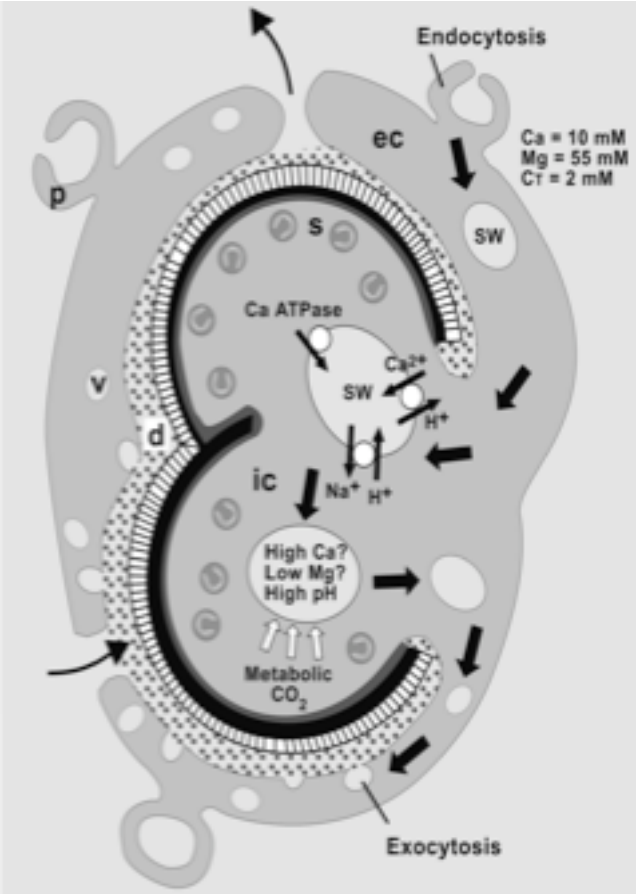

Figure 1.4. Simplified model of ion fluxes between the mineralization environment and seawater in perforate foraminifer (Erez, 2003). Future studies will likely show how the organic molecules within the deposition environment impose another layer onto this construct to influence the formation of specific CaCO3 polymorphs and their compositions.

6. References

Al-Horani, F. A., Al-Moghrabi, S. M., and de Beer, D., 2003. The mechanism of calcification and its relation to photosynthesis and respiration in the scleractinian coral Galaxea fascicularis. *Marine Biology* **142**, 419-426.

Ameye, L., De Becker, G., Killian, C., Wilt, F., Kemps, R., Kuypers, S., and Dubois, P., 2001. Proteins and saccharides of the sea urchin organic matrix of mineralization: Characterization and localization in the spine skeleton. *Journal of Structural Biology* **134**, 56-66.

Ameye, L., Hermann, R., Killian, C., Wilt, F., and Dubois, P., 1999. Ultrastructural localization of proteins involved in sea urchin biomineralization. *J. Histochem. Cytochem.* **47**, 1189-1200.

Anand, P., Elderfield, H., and Conte, M. H., 2003. Calibration of Mg/Ca thermometry in planktonic foraminifera from a sediment trap time series. *Paleoceanography* **18**, 1-15.

Armstrong, H. A. and Brasier, M. D., 2006. *Microfossils*. Blackwell, Malden.

Armstrong, N., Hardin, J., and McClay, D. R., 1993. Cell-cell interactions regulate skeleton formation in the sea urchin embryo. *Development* **119**, 833-840.

Bellwood, D. R., Hughes, T. P., Folke, C., and Nystrom, M., 2004. Confronting the coral reef crisis. *Nature* **429**, 827-833.

Beniash, E., Aizenberg, J., Addadi, L., and Weiner, S., 1997. Amorphous calcium carbonate transforms into calcite during sea urchin larval spicule growth. *Proceedings of the Royal Society of London Series B-Biological Sciences* **264**, 461-465.

Bentov, S. and Erez, J., 2006. Impact of biomineralization processes on the Mg content of foraminiferal shells: A biological perspective. *Geochemistry, Geophysics, Geosystems* **7**.

Berman, A., Addadi, L., Kvick, A., Leiserowitz, L., Nelson, M., and Weiner, S., 1990. Intercalation of sea-urchin proteins in calcite - study of a crystalline composite-material. *Science* **250**, 664-667.

Berman, A., Addadi, L., and Weiner, S., 1988. Interactions of sea-urchin skeleton macromolecules with growing calcite crystals - a study of intracrystalline proteins. *Nature* **331**, 546-548.

Berman, A., Hanson, J., Leiserowitz, L., Koetzle, T. F., Weiner, S., and Addadi, L., 1993. Biological control of crystal texture: A widespread strategy for adapting crystal properties to function. *Science* **259**, 776-779.

Cheers, M. S. and Ettensohn, C. A., 2005. P16 is an essential regulator of skeletogenesis in the sea urchin embryo. *Developmental Biology* **283**, 384-396.

Chiarello, R. P., Wogelius, R. A., and Sturchio, N. C., 1993. In-situ synchrotron X-ray reflectivity measurements at the calcite-water interface. *Geochimica Et Cosmochimica Acta* **57**, 4103-4110.

Cohen, A. L. and McConnaughey, T. A., 2003. Geochemical perspectives on coral mineralization, *Biomineralization*. Mineralogical Soc America, Washington.

Davis, K. J., Dove, P. M., Wasylenki, L. E., and De Yoreo, J. J., 2004. Morphological consequences of differential Mg2+ incorporation at structurally distinct steps on calcite. *American Mineralogist* **89**, 714-720.

Decker, G. L., Morrill, J. B., and Lennarz, W. J., 1987. Characterization of sea urchin primary mesenchyme cells and spicules during biomineralization in vitro. *Development* **101**, 297-312.

Delaney, M., B*é,* A. W. H., and Boyle, E. A., 1985. Li, Sr, Mg and Na in foraminiferal calcite shells from laboratory culture, sediment traps, and sediment cores. *Geochimica Cosmochimica Acta* **49**, 1327-1341.

Eggins, S., De Deckker, P., and Marshall, J., 2003. Mg/Ca variation in planktonic foraminifera tests: implications for reconstructing palaeo-seawater temperature and habitat migration. *Earth and Planetary Science Letters* **212**, 291-306.

Elhadj, S., De Yoreo, J. J., Hoyer, J. R., and Dove, P. M., 2006. Role of molecular charge and hydrophilicity in regulating the kinetics of crystal growth. *Proceedings of the National Academy of Sciences of the United States of America* **103**, 19237-19242.

Epstein, S. and Lowenstam, H. A., 1954. Temperature-shell-growth relations of recent and interglacial Pleistocene shoal-water biota from Bermuda. *Journal of Geology* **61**.

Erez, J., 2003. The source of ions for biomineralization in foraminifera and their implications for paleoceanographic proxies. In: Rosso, J. J. (Ed.),*Reviews in Mineralogy and Geochemistry*. Mineralogical Society of America, Washington.

Fu, G., Qiu, S. R., Orme, C. A., Morse, D. E., and De Yoreo, J. J., 2005. Acceleration of calcite kinetics by abalone nacre proteins. *Advanced Materials* **17**, 2678-+.

Gattuso, J. P., Frankignoulle, M., and Wollast, R., 1998. Carbon and carbonate metabolism in coastal aquatic ecosystems. *Annual Review of Ecology and Systematics* **29**, 405-434.

Gayathri, S., Lakshminarayanan, R., Weaver, J. C., Morse, D. E., Kini, R. M., and Valiyaveettil, S., 2007. In vitro study of magnesium-calcite biomineralization in the skeletal materials of the seastar Pisaster giganteus. *Chemistry-a European Journal* **13**, 3262-3268.

Guss, K. A. and Ettensohn, C. A., 1997. Skeletal morphogenesis in the sea urchin embryo: Regulation of primary mesenchyme gene expression and skeletal rod growth by ectoderm-derived cues. *Development* **124**, 1899-1908.

Hardie, L. A., 1996. Secular variation in seawater chemistry: An explanation for the coupled secular variation in the mineralogies of marine limestones and potash evaporites over the past 600 my. *Geology* **24**, 279-283.

Harkey, M. A., Klueg, K., Sheppard, P., and Raff, R. A., 1995. Structure, expression, and extracellular targeting of PM27, a skeletal protein associated specifically with growth of the sea urchin larval spicule. *Developmental Biology* **168**, 549-566.

Heasman, J., 2002. Morpholino Oligos: Making Sense of Antisense? *Developmental Biology* **243**, 209-214.

Hintz, C. J., Shaw, T. J., Chandler, G. T., Bernhard, J. M., McCorkle, D. C., and Blanks, J. K., 2006. Trace/minor element: calcium ratios in cultured benthic foraminifera. Part 1. Inter-species and inter-individual variability. *Geochimica Cosmochimica Acta* **70**, 1952-1963.

Hodor, P. G. and Ettensohn, C. A., 1998. The dynamics and regulation of mesenchymal cell fusion in the sea urchin embryo. *Developmental Biology* **199**, 111-124.

Illies, M. R., Peeler, M. T., Dechtiaruk, A. M., and Ettensohn, C. A., 2002. Identification and developmental expression of new biomineralization proteins in the sea urchin Strongylocentrotus purpuratus. *Development Genes and Evolution* **212**, 419-431.

Killian, C. E. and Wilt, F. H., 1996. Characterization of the proteins comprising the integral matrix of Strongylocentrotus purpuratus embryonic spicules. *Journal of Biological Chemistry* **271**, 9150-9159.

Kitajima, T. and Urakami, H., 2000. Differential distribution of spicule matrix proteins in the sea urchin embryo skeleton. *Development Growth & Differentiation* **42**, 295-306.

Kotachi, A., Miura, T., and Imai, H., 2006. Polymorph control of calcium carbonate films in a poly(acrylic acid)-chitosan system. *Crystal Growth & Design* **6**, 1636-1641.

Lea, D. W., 2006. The oceans and marine geochemistry. In: Elderfield, H. (Ed.), *Treatise on Geochemistry*. Elsevier.

Lea, D. W., Maschiotta, T. A., and Spero, H. J., 1999. Controls on magnesium and strontium uptake in planktonic foraminifera determined by live culturing. *Geochimica Cosmochimica Acta* **63**, 2369-2379.

Lea, D. W., Pak, J. K., and Paradis, G., 2005. Influence of volcanic shards on foraminferal Mg/Ca in a core from the Galapagos region. *Geochemistry, Geophysics, Geosystems* **6**.

Lear, C. H., Elderfield, H., and Wilson, P. A., 2000. Cenozoic deep-sea temperatures and global ice volumes from Mg/C in benthic foramaniferal calcite. *Science* **287**, 269-272.

Lear, C. H., Rosenthal, Y., and Slowey, N., 2002. Benthic foraminifera Mg/Ca-paleothermometry: A revised core-top calibration. *Geochimica Cosmochimica Acta* **66**, 3375-3387.

Lee, Y. H., Britten, R. J., and Davidson, E. H., 1999. SM37, a skeletogenic gene of the sea urchin embryo linked to the SM50 gene. *Development Growth & Differentiation* **41**, 303-312.

Levi, Y., Albeck, S., Brack, A., Weiner, S., and Addadi, L., 1998. Control over aragonite crystal nucleation and growth: An in vitro study of biomineralization. *Chemistry-a European Journal* **4**, 389-396.

Livingston, B. T., Killian, C. E., Wilt, F., Cameron, A., Landrum, M. J., Ermolaeva, O., Sapojnikov, V., Maglott, D. R., Buchanan, A. M., and Ettensohn, C. A., 2006. A genorne-wide analysis of biomineralization-related proteins in the sea urchin Strongylocentrotus purpuratus. *Developmental Biology* **300**, 335-348.

Lowenstam, H. A. and Weiner, S., 1989. *On Biomineralization*. Oxford University Press, New York.

Malinda, K. M. and Ettensohn, C. A., 1994. Primary mesenchyme cell migration in the sea urchin embryo: Distribution of directional cues. *Developmental Biology* **164**, 562-578.

McCrea, J. M., 1950. On the isotopic chemistry of carbonates and a paleotemperature scale. *Journal of Physical Chemistry* **18**, 849-857.

Medina-Elizalde, M. and Lea, D. W., 2005. The mid-Pleistocene transition in the tropical pacific. *Science* **310**, 1009-1012.

Medina-Elizalde, M., Lea, D. W., and Fantle, M. S., 2008. Implications of seawater Mg/Ca variability for Plio-Pleistocene tropical climate reconstruction. *Earth and Planetary Science Letters* **269**, 585-595.

Meibom, A., Cuif, J. P., Houlbreque, F., Mostefaoui, S., Dauphin, Y., Meibom, K. L., and Dunbar, R., 2008. Compositional variations at ultra-structure length scales in coral skeleton. *Geochim. Cosmochim. Acta* **72**, 1555-1569.

Meibom, A., Yurimoto, H., Cuif, J. P., Domart-Coulon, I., Houlbreque, F., Constantz, B., Dauphin, Y., Tambutte, E., Tambutte, S., Allemand, D., Wooden, J., and Dunbar, R., 2006. Vital effects in coral skeletal composition display strict three-dimensional control. *Geophys. Res. Lett.* **33**, 4.

Nudelman, F., Chen, H. H., Goldberg, H. A., Weiner, S., and Addadi, L., 2007. Spiers memorial lecture: Lessons from biomineralization: comparing the growth strategies of mollusc shell prismatic and nacreous layers in Atrina rigida. *Faraday Discussions* **136**, 9-25.

Nurnberg, D., Bijma, J., and Hemleben, C., 1996. Assessing the reliability of magnesium in foraminiferal calcite as a proxy for water mass temperatures. *Geochimica Cosmochimica Acta* **63**, 2369-2379.

Okazaki, K. and Inoue, S., 1976. Crystal property of the larval sea urchin spicule. *Development Growth & Differentiation* **18**, 413-434.

Pawlowski, J., Holzmann, M., Berney, C., Gooday, A. J., Cedhagen, T., Habura, A., and Bowser, S. S., 2003. The evolution of early foraminifera. *Proceedings of the National Academy of Science* **100**, 11494-11498.

Peled-Kamar, M., Hamilton, P., and Wilt, F. H., 2002. Spicule matrix protein LSM34 is essential for biomineralization of the sea urchin spicule. *Experimental Cell Research* **272**, 56-61.

Pennington, J. T. and Strathmann, R. R., 1990. Consequences of the calcite skeletons of planktonic echinoderm larvae for orientation, swimming, and shape. *Biol. Bull.* **179**, 121-133.

Piana, S., Jones, F., and Gale, J. D., 2007. Aspartic acid as a crystal growth catalyst. *Crystengcomm* **9**, 1187-1191.

Politi, Y., Arad, T., Klein, E., Weiner, S., and Addadi, L., 2004. Sea urchin spine calcite forms via a transient amorphous calcium carbonate phase. *Science* **306**, 1161-1164.

Politi, Y., Levi-Kalisman, Y., Raz, S., Wilt, F., Addadi, L., Weiner, S., and Sagi, I., 2006. Structural characterization of the transient amorphous calcium carbonate precursor phase in sea urchin embryos. *Advanced Functional Materials* **16**, 1289-1298.

Politi, Y., Metzler, R. A., Abrecht, M., Gilbert, B., Wilt, F. H., Sagi, I., Addadi, L., Weiner, S., and Gilbert, P., 2008. Transformation mechanism of amorphous calcium carbonate into calcite in the sea urchin larval spicule. *Proceedings of the National Academy of Sciences of the United States of America* **105**, 17362-17366.

Preston, R. R., 1998. Transmembrane Mg2+ currents and intracellular free Mg2+ concentration i Parmecium tetraurmelia. *Journal of Membrane Biology* **164**, 11-24.

Raz, S., Weiner, S., and Addadi, L., 2000. Formation of high magnesian calcites via an amorphous precursor phase: Possible biological implications. *Advanced Materials* **12**, 38-42.

Raz-Bahat, M., Erez, J., and Rinkevich, B., 2006. In vivo light-microscopic documentation for primary calcification processes in the hermatypic coral *Stylophora pistillata*. *Cell Tissue Research* **325**, 361-368.

Romani, A. and Maguire, M. E., 2002. Hormonal regulation of Mg2+ transport and homeostasis in eukaryotic cells. *Biometals* **15**, 271-283.

Rosenthal, Y., Boyle, E. A., and Slowey, N., 1997. Temperature control on the incorporation of mangesium, strontium, fluorine, and cadmium into benthic foraminiferal shells from Little Bahama Bank: Prospects for thermocline paleoceanography. *Geochimica Cosmochimica Acta* **61**, 3633-3643.

Russell, A. D., Hönisch, B., Spero, H. J., and Lea, D. W., 2004. Effects of seawater carbonate ion concentration and temperature on shell U, Mg, and Sr in cultured planktonic foraminifera. *Geochimica Cosmochimica Acta* **68**, 4347-4361.

Schneider, K. and Erez, J., 2006. The effect of carbonate chemistry on calcification and photosynthesis in the hermatypic coral Acropora eurystoma. *Limnology Oceanography* **51**, 1284-1293.

Segev, E. and Erez, J., 2006. Effect of Mg/Ca ratio in seawater on shell composition in shallow benthic foraminifera. *Geochemistry, Geophysics, Geosystems* **7**.

Sen Gupta, B. K., 1999. Modern Foraminifera. Kluwer Academic Publishers, Dordrecht.

Seto, J., Zhang, Y., Hamilton, P., and Wilt, F., 2004. The localization of occluded matrix proteins in calcareous spicules of sea urchin larvae. *Journal of Structural Biology* **148**, 123-130.

Silverman, J., Lazar, B., and Erez, J., 2007a. Community metabolism of a coral reef exposed to naturally varying dissolved inorganic nutrient loads. *Biogeochemistry* **84**, 67-82.

Silverman, J., Lazar, B., and Erez, J., 2007b. Effect of aragonite saturation, temperature, and nutrients on the community calcification rate of a coral reef. *Journal of Geophysical Research* **112**.

Stephenson, A. E., DeYoreo, J. J., Wu, L., Wu, K. J., Hoyer, J., and Dove, P. M., 2008. Peptides Enhance Magnesium Signature in Calcite: Insights into Origins of Vital Effects. *Science* **322**, 724-727.

Summers, R. G., Morrill, J. B., Leith, A., Marko, M., Piston, D. W., and Stonebraker, A. T., 1993. A sterometric analysis of karyokinesis, cytokineis and cell arrangements during and following 4th cleavage period in the sea-urchin, Lytechinus variegatus. *Development Growth & Differentiation* **35**, 41-57.

Takahashi, M. M. and Okazaki, K., 1979. Total cell number and number of the primary mesenchyme cells in whole, 1/2 and 1/4 larvae of Clypeaster japonicus. *Development Growth & Differentiation* **21**, 553-566.

Toyofuku, T., Kitazato, H., Kawahata, H., Tsuchiya, M., and Nohara, M., 2000. Evaluation of Mg/Ca thermometry in foraminifera: Comparison of experimental results and measurements in nature. *Paleoceanography* **15**, 456-464.

Urey, H. C., Lowenstam, H. A., Epstein, S., and McKinney, C. R., 1951. Measurement of paleotemperatures and temperatures of the Upper Cretaceous of England,

Denmark, and the southeastern United States. *Bulletin of the Geological Society of America* **62**, 399-416.

Urry, L. A., Hamilton, P. C., Killian, C. E., and Wilt, F. H., 2000. Expression of spicule matrix proteins in the sea urchin embryo during normal and experimentally altered spiculogenesis. *Developmental Biology* **225**, 201-213.

von Langen, P. J., Pak, J. K., Spero, H. J., and Lea, D. W., 2005. Effects of temperature on Mg/Ca in neogloboquadrinid shells determined by live culturing. *Geochemistry, Geophysics, Geosystems* **6**.

Wada, N., Yamashita, K., and Umegaki, T., 1999. Effects of carboxylic acids on calcite formation in the presence of Mg2+ ions. *J. Colloid Interface Sci.* **212**, 357-364.

Waldeab, S., Lea, D. W., Schneider, R., and Anderson, N., 2007. 155,000 years of West African monsoon and ocean thermal evolution. *Science* **316**, 1303-1307.

Wasylenki, L. E., Dove, P. M., and De Yoreo, J. J., 2005. Effects of temperature and transport conditions on calcite growth in the presence of Mg2+: Implications for paleothermometry. *Geochimica Cosmochimica Acta* **69**, 4227-4236.

Weber, J. N. and Raup, D. N., 1966. Fractionation of the stable isotopes of carbon and oxygen in marine calcareous organisms—the Echinoidea. Part II. Environmental and genetic factors. *Geochimica Cosmochimica Acta* **30**, 705-736.

Weiner, S. and Dove, P. M., 2003. An overview of biomineralization processes and the problem of the vital effect. In: Rosso, J. J. (Ed.), *Reviews in Mineralogy and Geochemistry*. Mineralogical Society of America, Washington.

Wilt, F., 1999. Matrix and mineral in the sea urchin larval skeleton. *Journal of Structural Biology* **126**, 216-226.

Wilt, F. and Ettensohn, C. A., 2007. The Morphogensis and Biomineralization of the Sea Urchin Larval Skeleton. In: Baeuerlein, E. and Behrens, P. Eds.), *Handbook of Biomineralization*. Wiley-VCH.

Wilt, F. H., 2002. Biomineralization of the spicules of sea urchin embryos. *Zoological Science* **19**, 253-261.

Wilt, F. H., Killian, C. E., Hamilton, P., and Croker, L., 2008. The dynamics of secretion during sea urchin embryonic skeleton formation. *Experimental Cell Research* **314**, 1744-1752.

Wilt, F. H., Killian, C. E., and Livingston, B. T., 2003. Development of calcareous skeletal elements in invertebrates. *Differentiation* **71**, 237-250.

Wolpert, L. and Gustafson, T., 1961. Studies on the cellular basis of morphogenesis of the sea urchin embryo , : Development of the skeletal pattern. *Experimental Cell Research* **25**, 311-325.

Xu, A. W., Dong, W. F., Antonietti, M., and Colfen, H., 2008. Polymorph switching of calcium carbonate crystals by polymer-controlled crystallization. *Advanced Functional Materials* **18**, 1307-1313.

Zhu, X. D., Mahairas, G., Illies, M., Cameron, R. A., Davidson, E. H., and Ettensohn, C. A., 2001. A large-scale analysis of mRNAs expressed by primary mesenchyme cells of the sea urchin embryo. *Development* **128**, 2615-2627.

Chapter Two

Biomolecules influence calcification by controlling magnesium content of amorphous calcium carbonate

Dongbo Wang[1], Adam F. Wallace[1], James J. DeYoreo[2] and Patricia M. Dove[1]

[1]*Department of Geosciences, Virginia Tech, Blacksburg VA 24061 USA*

[2]*Molecular Foundry, Lawrence Berkeley National Laboratory, Berkeley CA 94720 USA*

Minimally modified version of the paper published in *Proceedings of the National Academies of Sciences U.S.A.* **106**, 21511-21516. DOI: 10.1073/pnas.0906741106

1. Abstract

With the realization that many calcified skeletons form by processes involving a precursor phase of amorphous calcium carbonate (ACC), a new paradigm for mineralization is emerging. There is evidence the Mg content in biogenic ACC is regulated by carboxylated (acidic) proteins and other macromolecules, but the physical basis for such a process is unknown. We test the hypothesis that ACC compositions express a systematic relationship to the chemistry of carboxyl-rich biomolecules. A series of inorganic control experiments are conducted to establish the dependence of Mg/Ca ratios in ACC on solution composition. We then determine the influence of a suite of simple carboxylated organic acids on Mg content. Molecules with a strong affinity for binding Ca compared to Mg promote the formation of Mg-enriched ACC that is compositionally equivalent to high Mg-calcites and dolomite. Measurements show Mg/Ca ratios are controlled by a predictable dependence upon the binding properties of the organic molecules. The trend appears rooted in the conformation and electrostatic potential topology of each molecule but dynamic factors may also be involved. The dependence suggests a physical basis for reports that specific sequences of calcifying proteins are critical to modulating mineralization. Insights from this study may provide a plausible explanation for why some biogenic carbonates and carbonaceous cements often contain higher Mg signatures than are possible by classical crystal growth processes. The findings reiterate the controls of microenvironment on mineralization and suggest an origin of compositional offsets, or vital effects, long-recognized by the paleoclimate community.

2. Introduction

The carbonate skeletons of marine organisms contain variable and, in some species, exceptionally high levels of magnesium (SILLIMAN, 1846). Good examples are found in calcitic portions of mollusk shells that possess near-zero levels of Mg while certain calcareous skeletons of algae and echinoderms contain up to 30 mol% $MgCO_3$ (RAZ et al., 2003; WEBER, 1969; WEINER et al., 2003) and up to 50 mol% in the specialized teeth of sea urchins (ROBACH et al., 2006). Over the last 50 years, the origins of these high Mg levels have been elusive because calcites grown in the laboratory rarely contain more than 10-12 mol% Mg (BERNER, 1975; CHAVE et al., 1962; WALTER and HANOR, 1979). Although some alcohols and carboxylic acids can induce somewhat higher Mg levels (FALINI et al., 1996), synthetic calcites never acquire the high Mg signatures achieved in nature. Despite an extensive literature on the growth of carbonate minerals, explanations for the marked compositional differences between inorganic and biogenic carbonates have not been entirely satisfactory.

In recent years, a new paradigm for carbonate formation has emerged with the realization that many calcified skeletons develop by non-classical mineralization processes that involve a transient amorphous calcium carbonate phase (ACC) (AIZENBERG et al., 1996; BENIASH et al., 1997; MA et al., 2008; POLITI et al., 2004; POLITI et al., 2008; RAZ et al., 2000; WEISS et al., 2002). In contrast to classical crystal growth by step growth via the terrace-ledge-kink (TLK) model (BURTON et al., 1951), this type of mineral formation begins by stabilizing ACC as a reactive intermediate that later transforms to one or more crystalline carbonate polymorphs such as calcite or aragonite (BENIASH et al., 1997; RAZ et al., 2000). Evidence from studies of calcifying tissues shows organisms employ this mineralization strategy across the phylogenetic tree (WEINER et al., 2003). The process is not well understood, however, and significant compositional differences in biominerals raise the question of how mineralization by this pathway affects the Mg signatures. This question is significant because Mg contents are extensively utilized to infer past environmental conditions from the carbonate sedimentary record. Hundreds of studies are founded upon the assumption that biological calcification occurs by classical crystal growth (MACKENZIE et al., 1983), but how far do

insights from mineralization by terrace-ledge-kink (TLK) processes apply to biomineral formation? Moreover, emerging evidence from sedimentary systems suggest that alternative mineralization pathways may also explain the occurrence of some dolomites and carbonate cements in organic-rich environments.

Several studies suggest the formation and stability of biogenic ACC is regulated by proteins and other macromolecules. Investigations show that, where tested, ACC contains significant levels of proteins that are intimately associated with the carbonate phase (GOTLIV et al., 2003; WEINER et al., 2003). The detailed chemistry and structure of these macromolecules vary over the course of mineralization (RAZ et al., 2003), but their overall compositions are significantly enriched in acidic side chains (LOWENSTAM and WEINER, 1989). For example, the ACC of crustaceans contain proteins that have unusually high proportions of glutamate and glutamine residues (AIZENBERG et al., 1996) while corals and mollusks contain up to 35% aspartate (GOTLIV et al., 2003; LOWENSTAM and WEINER, 1989). Although, it is difficult to conduct *in vivo* studies that demonstrate a direct relationship between the presence of acidic proteins and ACC formation, insights from *in vitro* studies show these macromolecules must modulate mineral formation and growth (GOTLIV et al., 2003).

Almost all known forms of naturally occurring ACC contain Mg at levels comparable to those measured in biogenic carbonate minerals (WEINER et al., 2003). There is also evidence that a relationship exists between the Mg content of biogenic ACC and the chemistry of local biomolecules. For example, certain glycoproteins may affect skeleton composition (LEVI et al., 1998). An *in vitro* study showed carbonates formed from ACC in the absence of macromolecules contained up to 21 mol% Mg, but Mg contents were increased up to 34% when proteinaceous extracts from coraline algae and acidic polymers were present (RAZ et al., 2000). Similar Mg-promoting effects are reported in studies of calcification that use polyelectrolytes (polyacrylic acid and polyaspartic acid) to induce carbonate crystallization through an ACC intermediate (CHENG et al., 2007). Moreover, *in vivo* studies of calcification in foraminifera also note the probable role of biomolecules, specifically those in the organic matrix, in modulating species-specific levels of Mg incorporation through ion-specific interactions with Mg versus Ca ions in the biological crystallization environment (SEGEV and EREZ, 2006).

Stephenson et al. (2008) showed that the Mg content of calcite is increased by up to 3 mol% when grown in the presence of aspartic acid-rich polypeptides. These studies suggest the possibility that biomolecule chemistry has a systematic and potentially predictable control on Mg content.

Building from the findings of previous studies, we test the hypothesis that carboxylated biomolecules have chemistry-specific interactions with calcium and magnesium in the local mineralization environment to affect Mg signatures in ACC. We further consider that these signatures, as Mg/Ca ratios, are modulated by the interactions of these biomolecules with calcium and magnesium in a systematic way. To approach this problem, we first establish the relationship between Mg uptake into ACC and the solution concentration of Mg in the *absence* of biomolecules. Working from this baseline, we then measure the ratio of Mg to Ca in ACC produced in the presence of a suite of small carboxylic acids. These compounds are simple proxies for the macromolecules within biological crystallization environments but there is precedent for building an understanding of macromolecule influences on mineralization by investigating small molecules (ELHADJ et al., 2006). We find the Mg-enhancing effect follows a systematic relationship that correlates with the ability of carboxyl groups to interact with calcium relative to magnesium, suggesting biomolecules influence the formation of amorphous metal carbonate ion-pair clusters. Further analysis suggests carboxylated molecules, which have the strongest electrostatic potential can greatly increase Mg content to levels that are comparable to the compositions of high magnesium calcites and some dolomites.

3. Methods

Precipitation of ACC used the ammonium carbonate diffusion method (HAN and AIZENBERG, 2008). For each experimental condition three replicate samples were produced by pipetting six mL of Ca and Mg chloride solution into a petri dish and then sealing in a dessicator with 0.6-0.7 g of freshly opened ammonium carbonate salt ($(NH_4)_2CO_3$, Sigma). Solutions were visually monitored until becoming cloudy and then removed. The resulting solution plus ACC material was then quickly vacuum filtered through 0.2 μM nylon membranes (Whatman) and rinsed with anhydrous ethanol (99.5%, Sigma). Filter membranes holding the captured ACC was subsequently dried overnight in a vacuum desiccator at ambient temperature. The resulting materials were confirmed to

be ACC by SEM and Raman microanalysis (see **Supplementary Information Fig S.2.1**). Thermogravimetric analyses showed that all of the ACC, formed in the absence or presence of biomolecules, contained approximately one water molecule per unit of calcium carbonate (**Fig S.2.2**).

The materials used in the synthesis were comprised of 25mM $CaCl_2 \cdot 2H_2O$ (99.99%, Sigma) with variable amounts of $MgCl_2 \cdot 6H_2O$ (99.995%, Sigma) to produce Mg/Ca ratios of 0.0, 1.0, 2.0, 3.0, 4.0, 5.0, and 6.0. For each Mg/Ca ratio, L-aspartic acid sodium monohydrate ($C_4H_6NNaO_4 \bullet H_2O$, 99.0%, Fluka) and L-Glutamic acid sodium monohydrate ($C_5H_8NNaO_4 \bullet H_2O$, 98.0%, Sigma) was introduced to give concentrations of 0.0, 0.01, 0.025, 0.05, and 0.10 M. The same procedure was used in experiments that contained 0.025 M of oxydiacetic acid ($C_4H_6O_5$, 98%, Sigma), citric acid ($C_6H_8O_7$, 99.5%, Sigma, malonic acid($C_3H_4O_4$, Sigma), D-tartaric acid ($C_4H_6O_6$, 99%, Sigma).

The Mg and Ca concentrations in the resulting ACC were determined by first dissolving the precipitate by placing the filter in 0.1 M nitric acid (99.999%, Sigma) for 30 minutes. The three replicate solutions were analyzed for Mg and Ca by ICP-OES (Spectro CirOS VISION) from calibration curves prepared from Plasma Grade single element standards (SPEX CertiPreps Inc.). Levels of oxydiacetic acid, D-tartaric acid, citric acid, malonic acid were determined by HPLC-DAD detector with a Resteck Pinnacle DC C18 column. Aspartic acid levels were measured by HPLC by established methods (1997)

Electrostatic potential maps were calculated for fully deprotonated versions of imino-, thio-, and oxy-diacetic acid with the Gaussian03 software package (FRISCH et al., 2004). Solvent effects were treated with a self-consistent isodensity polarizable continuum model (FORESMAN et al., 1996) having a dielectric constant equal to that of bulk water at 25°C (78.36). The solvent cavity was defined as the 0.0004 e/a_o^3 isosurface of the electron density, and a grid size of 974 points was used for numerical surface integration. This same approach was used in conjunction with normal mode analysis to compute the change in free energy associated with the transfer of the neutral carboxylic acid species (aspartate, glutamate, malonate, D-tartarate, citrate, imino-, thio-, and oxy-diacetate) from the gas phase to solution ($\Delta G_{transfer} = G_{soln} - G_{gas}$). This quantity is a measure of the hydrophilic versus hydrophobic character of a molecule. Previous studies have employed

other hydrophilicity scales to explain enhanced rates of growth and impurity incorporation into calcite in the presence of biocarboxylic acids.

4. Results and Discussion

A previous study (GEBAUER et al., 2008) suggested ACC formation is initiated in inorganic environments with aggregation of aqueous $CaCO_3$ ion-pairs into prenucleation clusters. Their stability is determined by thermodynamic equilibrium between solvent, individual hydrated ions and hydrated clusters by the general reaction:

$$zCa^{2+} + zCO_3^{=} = z(CaCO_3)_{aq} \quad (1)$$

where z is the number of $CaCO_3$ units in a cluster. For the situation where ACC is formed in the presence of magnesium ion, we assume an analogous reaction for the formation of an amorphous magnesium calcium carbonate:

$$yMg^{2+} + zCa^{2+} + y+z(CO_3^{=}) = (Ca_zMg_y(CO_3)_{y+z})_{aq} \quad (2)$$

where y is the number of $MgCO_3$ units in a cluster and the resulting solid solution has z plus y units in the solid solution cluster that forms. The equilibrium constant for rxn (2) and the absolute values of y and z are yet unknown and cannot be assessed in this study. The ratio of y/z, however, gives the fraction of Mg/Ca that forms in ACC without the constraint of having to know the total of y+z at this time, which may vary with solution conditions. By this approach, we assess the dependence of Mg/Ca ratio in ACC on solution composition and carboxylic acid chemistry.

To establish the baseline relationship between the solution Mg/Ca ratio and Mg content of the ACC that forms, experiments were first conducted for a series of inorganic controls. The Mg/Ca molar ratio was varied in solution from 0 to 6.0 by holding Ca concentration constant at 25 mM while increasing the Mg level. Characterization of these materials shows ACC forms as spherical particles and with characteristic Raman spectra (see Supplementary Information). **Figure 2.1ABC** shows that for the range of conditions used in this study, Mg/Ca ratio in ACC is linearly dependent upon the ratio of Mg/Ca in solution (blue symbols, **Fig 2.1ABC**) as predicted by the stoichiometry in rxn

(2). The distribution of Mg and Ca between the solution and precipitated phases is quantified by the simple empirical relationship:

$$K_D = (Mg/Ca)_{ACC} / (Mg/Ca)_{solution} \quad (3)$$

where K_D is the partition coefficient specific to the conditions of these experiments (ambient temperature, pH range of precipitation: 9.5-10.3). The ACC that forms in solutions containing Mg/Ca levels of seawater (5.0) produces a Mg/Ca ratio of approximately 0.45. To put this into perspective using a simple calcium carbonate stoichiometry, this corresponds to a composition of $Mg_{0.31}Ca_{0.69}CO_3$.

From the inorganic baseline, two types of experiments were conducted. The first measured Mg/Ca in ACC that forms from solutions containing different concentrations of Aspartic (Asp) or Glutamic (Glu) acids. These amino acids were chosen for their prevalence in biocalcification environments. **Fig 2.1A and 2.1B** show that Asp and Glu, respectively, significantly increase the Mg/Ca ratio of ACC above that measured for the control experiments. When Asp and Glu concentrations are low, Mg/Ca ratios increase with an approximately linear dependence on solution composition, similar to the inorganic controls. At higher levels, Asp and Glu (0.1M), increase Mg/Ca ratios in ACC to much larger values of 2.2 ($Mg_{0.68}Ca_{0.32}CO_3$) and 2.5 ($Mg_{0.71}Ca_{0.29}CO_3$), respectively. As Asp or Glu concentration increases, the data show these compounds become less effective at promoting Mg uptake to give a sublinear dependence on Mg/Ca in solution. This suggests ACC and/or the Asp and Glu are becoming saturated in their ability to interact with Ca.

A second type of experiment was conducted to probe the ability of carboxylated compounds to influence magnesium content of ACC. Employing five different carboxylic acids (e.g. **Table 2.1**), we measured their effect on Mg/Ca ratios in ACC in experiments that held Ca^{2+} concentration at 25 mM. **Fig 2.1ABC** shows all of these compounds promote Mg uptake into ACC and their influence is highly dependent upon the type and concentration of carboxylic acid in solution. To better illustrate these biomolecule-specific differences, **Fig 2.2A** shows a subset of data from experiments with a solution Mg/Ca ratio = 2.0 and a biomolecule concentration = 0.025 M. These measurements are

plotted versus the Mg and Ca binding constants reported for each molecule (**Table 2.1**) as the log of ($K_{Mg\text{-ligand}}/K_{Ca\text{-ligand}}$). The correlation shows a systematic trend whereby Mg content of ACC increases with the ability of each multicarboxylic acid to complex Ca relative to Mg. The Mg/Ca values measured in ACC increase in the order: malonic < aspartic < citric < glutamic < D-tartaric < oxydiacetic acid. Similar trends are exhibited for ACC grown at higher Mg/Ca solution levels = 4.0 and 5.0 (**Fig 2.2BC**). As expected for the higher Mg/Ca growth solutions, ACC compositions are offset to higher Mg/Ca levels. Although **Fig 2.2B and 2.2C** have greater compositional variability, all data show a dependence on binding constants. Solutions containing low levels of oxydiacetic acid at the highest solution ratio of Mg/Ca (**Fig 2.2C**), produced ACC with a remarkably high Mg/Ca ratio of 1.1 ($Mg_{0.52}Ca_{0.48}CO_3$).

Evidence from the data and previous studies suggest two plausible explanations for how biomolecules might influence the Mg content of ACC. First we consider if compositions reflect the degree of carboxylic acid incorporation in the solid. To test this idea a series of samples were synthesized in solutions containing 0.025 M aspartic, malonic, D-tartaric, oxydiacetic or citric acids (at 2.0, 4.0 and 5.0 Mg/Ca of solution). Compositional analysis by HPLC found little organic in any of the resulting ACC with an average of 1.7 mol% and a maximum of approximately 4 mol% for D-tartaric acid. There was no correlation between the Mg level and carboxylic acid content of the ACC. In the absence of a relationship between Mg/Ca ratio and carboxylic acid incorporation, even with high organic concentrations in solution, we conclude that direct incorporation of organo-magnesium complexes is not the origin of variable Mg/Ca ratios.

An alternative explanation considers that because ACC forms from solution, the specific ability of organic molecules to bind aqueous Ca versus Mg could affect the activities of these ions in solution. That is, carboxylic acids may modify Mg/Ca ratios in ACC by modulating solution chemistry. Reported binding constants for Mg and Ca with these multicarboxylated compounds show a wide range of affinities and cation selectivity (**Table 2.1**). From this, we consider a physical model whereby carboxylic acids regulate the relative abundance of calcium carbonate and magnesium carbonate ion-pairs in solution through differential binding of free Ca^{2+} and Mg^{2+}. When conditions are biased to favor formation of $MgCO_3°$ species, a higher magnesian ACC can be produced.

To understand changes in ACC compositions within a thermodynamic framework, we begin by assuming cation desolvation is an initial and critical step to forming these amorphous solids (KOWACZ and PUTNIS, 2008). A simple construct for producing an amorphous solid calls for pairing charged ionic components into neutral species that associate with similar species to form small clusters, perhaps by water displacement and hydrolysis. This is consistent with experimental and TEM evidence from studies (GEBAUER et al., 2008; POUGET et al., 2009) that led to rxn (2). To first consider the effect of Mg on ACC stoichiometry in the absence of organics, we rewrite rxn (2) into two statements that explicitly consider the formation of the neutral ion pairs, $Mg_y(CO_3)_y°$ and $Ca_z(CO_3)_z°$, as intermediate species such that:

$$yMg^{2+} + zCa^{2+} + y+z(CO_3^{=}) = Mg_y(CO_3)_y° + Ca_z(CO_3)_z° \qquad (4a)$$

where the equilibrium constants for these reactions are unknown. Rxn (4a) shows the distribution and abundance of the resulting ion pairs is dependent upon the local activity of the free (hydrated) Mg^{2+} or Ca^{2+} ions. The distribution of these ion pair species therefore modulates ACC composition by influencing the activities of reactants that subsequently coalesce to form the Ca-Mg final product:

$$Mg_y(CO_3)_y° + Ca_z(CO_3)_z° = Ca_zMg_y(CO_3)_{y+z,\ aq} \qquad (4b)$$

Thus, ACC composition results from the distribution of ion pair species that are available to form clusters (rxn 4b). Like rxn (2), presumably both of these hypothetical reactions are in thermodynamic equilibrium with the local environment.

With the introduction of organic ligands, activities of free $Mg^{2+}$and Ca^{2+} are reduced by molecule-specific interactions with carboxyl groups to influence (rxn 4a), which subsequently shifts compositions to the final ACC product (rxn 4b). The extent of this effect can be seen in reported values (**Table 1**) of first association constants for binding Ca^{2+} and Mg^{2+} to the carboxyl group(s) of each organic by the reaction:

$$Mg^{2+} + \text{ligand} = Mg(\text{ligand})° \qquad K_{\text{Mg-ligand}} \qquad (5a)$$

Ca^{2+} + ligand = Ca(ligand)° $K_{Ca\text{-}ligand}$ (5b)

For example, dioxyacetic acid has a significantly stronger interaction with Ca^{2+} compared to Mg^{2+} with equilibrium constants of $10^{3.38}$ and $10^{1.8}$, respectively (**Table 2.1**). In contrast, aspartic acid shows some preference for Mg^{2+} with a binding constant of $10^{2.43}$ compared to the smaller value of $10^{1.6}$ for Ca^{2+}. This suggests that when the organic is highly selective for calcium over magnesium, the equilibrium distribution of metal carbonate ion pairs shifts towards a greater proportion of $MgCO_3$°, resulting in an increased concentration of this component in the amorphous phase.

To test this model, we return to **Fig 2.2ABC** and consider the apparent relationship between Mg/Ca ratios measured in ACC and the binding constants of these molecules. The data show ACC formed in the presence of oxydiacetic acid has the greatest Mg enrichment for all of the solution ratios of Mg/Ca. Indeed, oxydiacetic has a $K_{Ca\text{-}ligand}$ that is a remarkable 63 times larger than the $K_{Mg\text{-}ligand}$ (**Table 2.1** and x axis of **Fig 2.2ABC)**. According to the proposed physical model, oxydiacetate is the most effective at reducing free Ca activity compared to Mg, and is thus shifts the reaction to favor the larger $Mg_y(CO_3)_y$° population that subsequently coalesces to form high Mg ACC. The model predicts that as $K_{Ca\text{-}ligand}$ decreases relative to $K_{Mg\text{-}ligand}$ for a given organic compound, then the Mg/Ca ratio in the resulting ACC should decrease towards the value measured for the inorganic baseline. Indeed, **Fig. 2.2ABC** shows a direct correspondence between Mg enrichment in ACC and the selectivity of individual carboxylic acids for Mg and Ca from solution.

While the simple thermodyamic model posed here gives a good explanation for the experimental data, a closer inspection of **Fig 2.2ABC** suggests that additional factors must also be at work. If Mg/Ca ratios were solely dependent upon changes in free Mg and Ca, one would expect that ligands, which have no specificity for Mg vs. Ca (e.g. log ($K_{Mg\text{-}ligand}/K_{Ca\text{-}ligand}$) = 0), should plot on the baseline and those which are selective for Mg would suppress Mg/Ca levels to plot below those measured for inorganic control. However, the data show that every type of molecule used in this study promotes the Mg content above baseline. This 'offset' indicates additional factors, possibly kinetic, must also influence the Mg/Ca level. Indeed, evidence from previous studies of biomolecule-

carbonate interactions suggest that dynamic influences could alter the local solvation environment about acidic biomolecules and hydrated ions to favor greater Mg uptake (ELHADJ et al., 2006; KOWACZ and PUTNIS, 2008; PIANA et al., 2007; STEPHENSON et al., 2008).

To better understand how other types of molecules might influence ACC compositions, we consider the character of oxydiacetic acid (ODA) and the origin of its strong affinity for Ca relative to Mg. **Fig 3A** shows that negative electrostatic potential is most strong between the two distal carboxyl groups, and adjacent to the central oxygen atom. Metal binding occurs in this region, and ODA generally maintains planar and facial conformations upon complex formation. Many factors contribute to the stability of these complexes (i.e. electrostatic attraction of the ion for the ligand, the radius, charge density and solvation dynamics of the ion, and steric limitations within the ligand). The strengths of metal-oxydiacetate complexes have been roughly correlated with ligand flexibility and the amount of entropy gain upon ion association (FORSTER and CHEETHAM, 2004; NASH et al., 1991). As ODA forms tridentate complexes with metals in solution, interactions with hard ions such as Mg can force the ligand-ion complex to adopt a very specific configuration (GRIRRANE et al., 2005), effectively reducing the entropic contribution to complex stability. However, for softer ions, like Ca, entropy gain confers stability unto the ODA complex. By contrast, the imino (IDA) and thio (TDA) derivatives of ODA have substitutions of NH and S, respectively, for the central oxygen atom. The reduction in the negative electrostatic potential that occurs alongside these substitutions (**Fig 2.3BC**) results in the loss of binding preference for Ca over Mg (for example log ($K_{\text{Mg-IDA}}$ / $K_{\text{Ca-IDA}}$) = 0.35) (ANDEREGG et al., 2005). Additionally, crystal structures show IDA and TDA adopt more twisted configurations when bound to metals (FORSTER and CHEETHAM, 2004; GRIRRANE et al., 2005; GRIRRANE et al., 2007), suggesting that sizeable steric barriers may also oppose complex formation in solution.

The marked differences in the electrostatic potential of these chemically similar derivatives provide an opportunity to test this formation-based explanation. Because electronic distributions suggest IDA and TDA are unable to preferentially interact with either cation, these organics would be expected to have little effect on the resulting ACC compositions. Indeed, experimental measurements show the Mg/Ca ratio of the ACC that

forms in the presence of IDA and TDA are approximately the same as the inorganic control (**Fig 2.3D**). These findings are consistent with model expectations.

These experimental data and structural models demonstrate that multicarboxylic character is, in itself, insufficient to promote a high Mg content in ACC. Rather, the evidence suggests that adjacent chemical moieties impose an additional level of regulation on the ability of carboxyl-rich compounds to bind Mg^{2+} and Ca^{2+}. This suggests a mechanistic basis for how macromolecules could modulate local activities of Ca^{2+} and Mg^{2+} to give differences that are not recorded in compositional analyses of tissues at sites of calcification. The findings also suggest a predictive tool for building from these concepts to design polypeptides and other molecules that give *a priori* controls on impurity levels in carbonate and possibly other mineral phases.

5. Implications

Insights from this study raise a number of questions regarding calcification processes in organisms. Because many carbonate skeletons crystallize from ACC, we ask how the macromolecule chemistry within these biomineralization microenvironments affect ACC compositions. Our study cannot provide a quantitative answer, but there is evidence the influences of small molecules such as those used in this study can be scaled to understand some aspects of how proteins and other large macromolecules influence carbonate growth (ELHADJ et al., 2006; FU et al., 2005). Another example is found in casequetrin, a protein which has specificity for Ca^{2+} over Mg^{2+} (BEARD et al., 2004). This protein is found in cardiac and muscle cells, but biomineral-associated proteins have similar abilities such as the 'acidic' region of Asp-rich calcification proteins which have up to 68% homology with the 'acidic' region of calsequestrin (GOTLIV et al., 2005). Interestingly, another region of Asprich (DEAD repeat) is known to bind Mg (GOTLIV et al., 2005). While several studies have examined the composition of these types of macromolecules and made inferences regarding their ability promote and stabilize ACC formation, our findings suggest they may have additional roles in modulating composition. Evidence from this study indicates that molecule stereochemistry should also influence composition. That is, specific sequence and secondary structure must also be part of the story.

The findings raise another intriguing question for biogenic carbonates that cannot be answered in this study— If biomolecule chemistry influences ACC composition, could this modulate the Mg content of the final calcite or aragonite that comprises a calcified carbonate skeleton? Organisms living within *similar* environments are known to produce skeletons with different Mg contents, suggesting internal or genetic controls that are not strongly correlated with their environment of formation. These 'vital effects' are believed to arise from kinetic and taxonomic differences but the physical basis for these variations are not well understood (WEINER and DOVE, 2003). Insights from this study suggest the possibility that a mechanistic explanation for understanding species-specific differences could be rooted in biomolecule controls on the composition of the precursor carbonate phase.

Our findings also have broad implications for better understanding the origins of dolomites and other high magnesian calcites that are found throughout the geologic record. Many of these sedimentary environments are organic graveyards that are rich with macromolecules and microbial activity (CARTER and MITTERER, 1978). Anecdotal evidence has long-suggested these environments influence mineralization (CARTER and MITTERER, 1978) and our findings suggest a physical basis for this observation. **Fig 2.4** shows the simple organics used in this study can readily push Mg/Ca levels into the compositional ranges reported for the high magnesium carbonates (HMC) and dolomites of biological and sedimentary carbonates. Moreover, this enhancement is possible in solutions with Mg/Ca ratios of only 2.0 and the 5.0 of modern seawater without requiring the extreme levels of Mg enrichment in solution that have been suggested (FOLK and LAND, 1975).

It is particularly intriguing that dolomites are notoriously difficult to synthesize at low temperatures by experiment (FOLK and LAND, 1975), but Vasconcelos and McKenzie (1997) have shown that active dolomite formation is occurring in organic rich environments as chemical precipitates that are most likely microbially derived (SANCHEZ-ROMAN et al., 2008; VAN LITH et al., 2003; WARTHMANN et al., 2000; WRIGHT and WACEY, 2005). Our observations raise the question of whether the Mg-rich carbonates that are so widespread in biogenic and sedimentary environments are formed by nonclassical processes from a transient phase such as ACC. It would seem possible

because the initial precipitates in these environments are aggregates of nanoparticles (50-100 nm), which may start as amorphous precursors (SCHMIDT et al., 2005). The experimental data from this study support the idea that carboxyl rich molecules in the environment provide a means for greatly increasing Mg content in the amorphous precursors (**Fig 2.4**) that later transform into dolomite. By deciphering the influences of local biochemistry on composition and stability, a new view may be emerging into the mechanistic basis by which organic and physical factors interplay to influence Mg content and possibly polymorph selection in biogenic and inorganic environments alike.

6. Acknowledgements.

We are grateful to Prof. J.D. Rimstidt for many thoughtful discussions. We thank Prof. D.L. Popham and J. Smiley for HPLC analysis; H. Motegi, N. Dixit and Prof. R.B. Moore for assistance with TGA. The research was supported by awards to PMD from the US Dept. of Energy (grant FG02-00ER15112) and NSF (grant OCE-052667). The work was also performed under the auspices of the US DOE by an award to JJD at the Univ. of Calif., Lawrence Livermore National Laboratory, under Contract No. W-7405-Eng-48. Opinions, findings, and conclusions or recommendations expressed in this material are those of the authors and do not necessarily reflect the views of NSF or DOE.

Table 2.1. Summary of binding constants for multicarboxylic acids used in this study, their net charge at pH 8.5, induction time and pH at induction.

	Binding Constant [1]			Net Charge	Induction	
	$\log K_{Ca}^{2+}$	$\log K_{Mg}^{2+}$	$\log\left(\frac{K_{Mg^{2+}}}{K_{Ca^{2+}}}\right)$		Time (min)	pH
$C_4H_6O_5$ (dioxyacetic acid)	3.38	1.8	-1.58	-2.0	136	9.79
$C_4H_6O_6$ (D-tartaric acid)	1.8	1.36	-0.44	-2.0	66.5	9.37
$C_6H_8O_7$ (citric acid)	3.5	3.37	-0.130	-3.0	114.5	9.58
$C_5H_9O_4N$ (glutamic acid)	1.43	1.9	0.47	-1.7	50	9.80
$C_3H_4O_4$ (malonic acid)	1.51	2.11	0.60	-2.0	88.5	9.66
$C_4H_7O_4N$ (aspartic acid)	1.6	2.43	0.830	-1.7	68	9.80
HCO_3^- (hydrogen carbonate)	1.0	0.95	-0.05	-1.0		
CO_3^{2-} (carbonate)	3.15	2.88	-0.27	-2.0	40.5	10.34

[1] Binding constant K for the generalized association reaction: M+L ⇔ ML with M representing the metal and L the ligand

Smith and Martell 1976

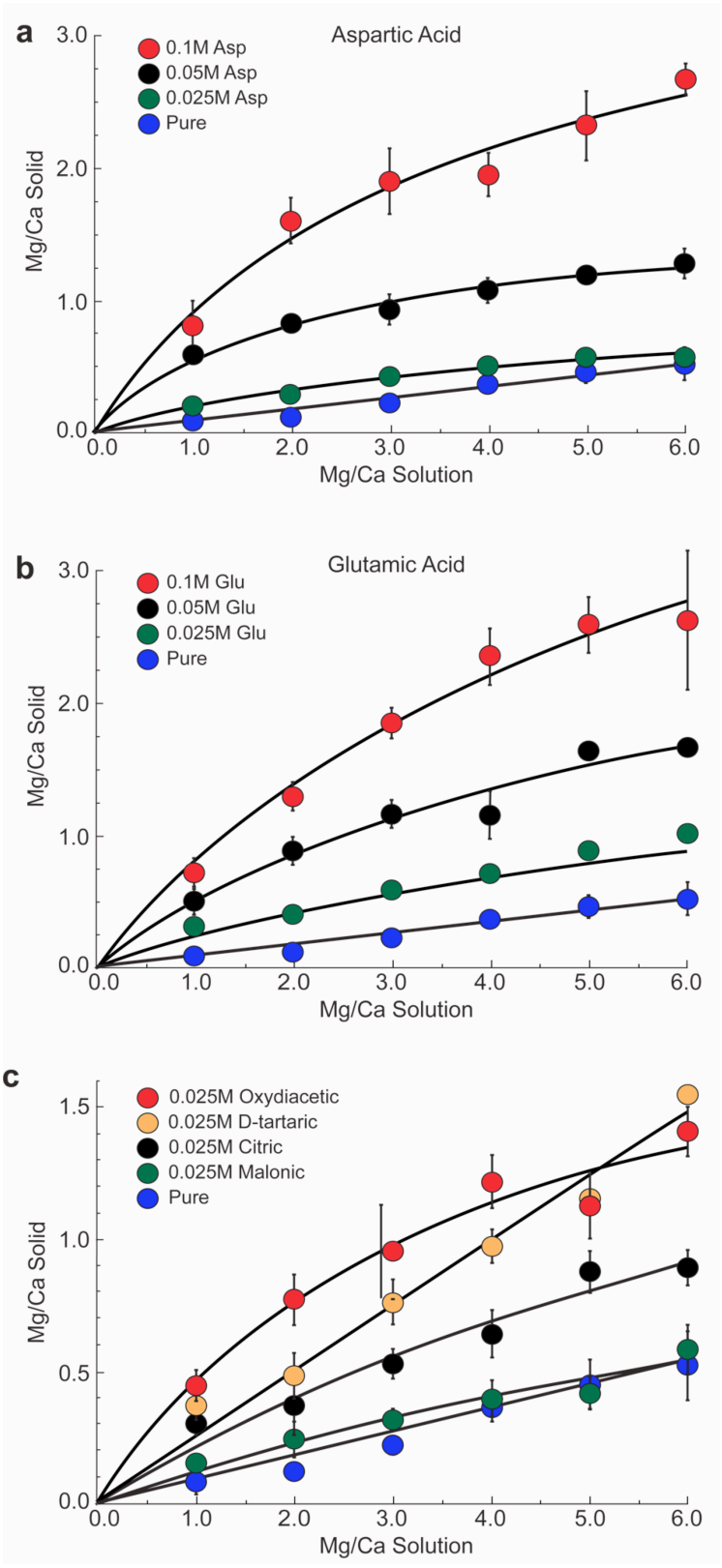

Figure 2.1. Mg/Ca ratio in solution vs. Mg/Ca in ACC for the inorganic control experiments **a)** for aspartic acid at 0.1M, 0.05 M and 0.025; M **b)** for glutamic acid at 0.1M, 0.05 M and 0.025 M; **c)** four carboxylic acids at 0.025M: oxydiacetic, D-tartaric, citric and malonic acids.

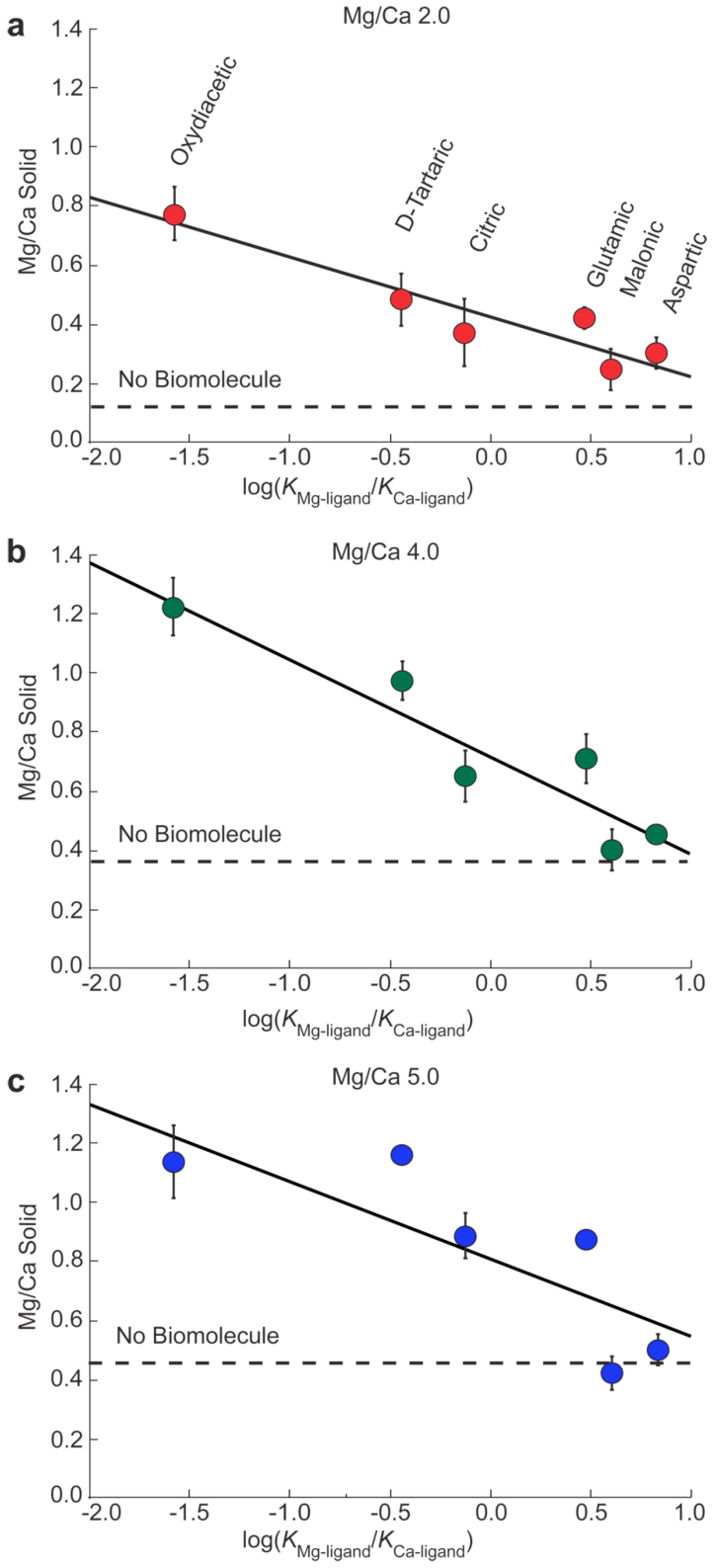

Figure 2.2. Mg/Ca ratio in ACC vs. log ($K_{Mg\text{-}ligand}/K_{Ca\text{-}ligand}$) at 0.025 M of oxydiacetic, D-tartaric, citric, glutamic, malonic and aspartic acids. **a)** Solution Mg/Ca ratio = 2.0 **b)** Solution Mg/Ca ratio = 4.0 **c)** Solution Mg/Ca ratio = 5.0 (modern seawater).

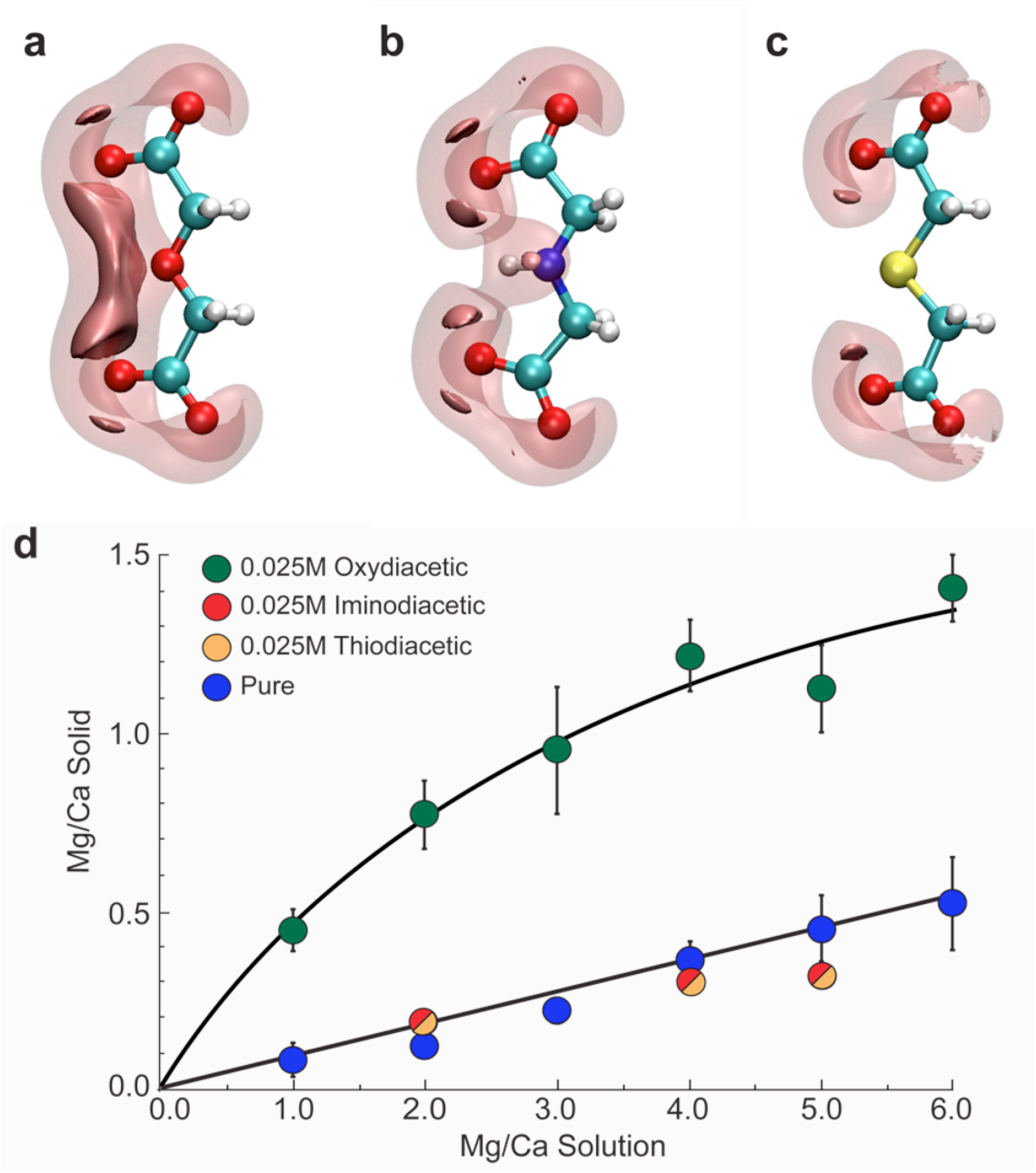

Figure 2.3. Isosurfaces of the negative electrostatic potential about **a)** oxydiacetate (ODA), **b)** iminodiacetate(IDA); and **c)** thiodiacetate (TDA). The transparent and opaque surfaces are contoured at -0.35 and -0.40 a.u. respectively. **d)** Measured Mg/Ca of ACC formed in the presence of 0.025 M ODA, IDA or TDA relative to the inorganic baseline.

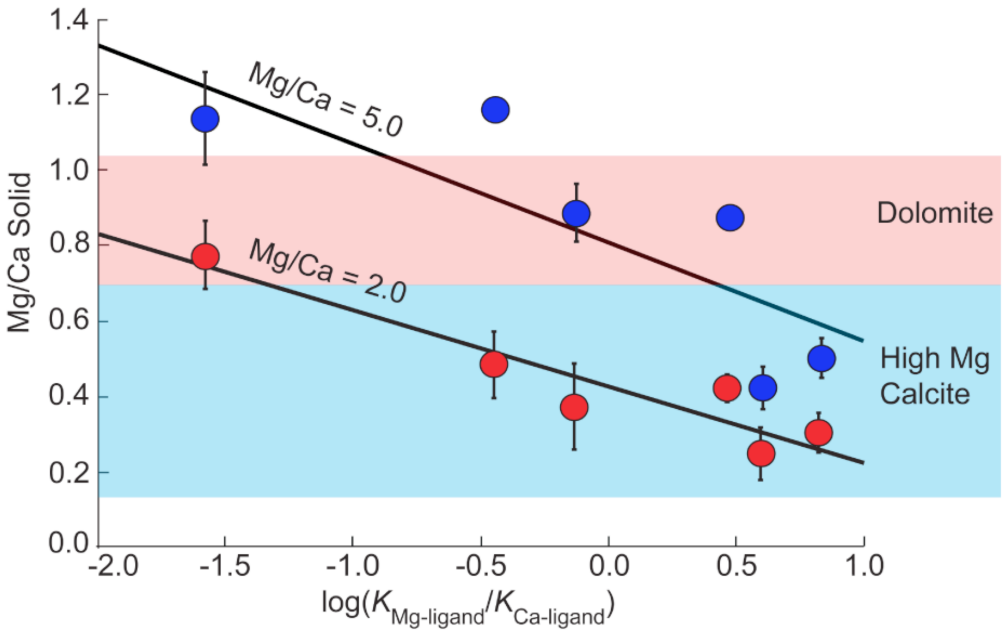

Figure 2.4. Mg/Ca ratio in the solid vs. log ($K_{Mg\text{-}ligand}/K_{Ca\text{-}ligand}$) for 0.025M oxydiacetic, D-tartaric, citric, glutamic, malonic and aspartic acids. Shaded boxes show compositional ranges of high magnesian calcite and dolomite.

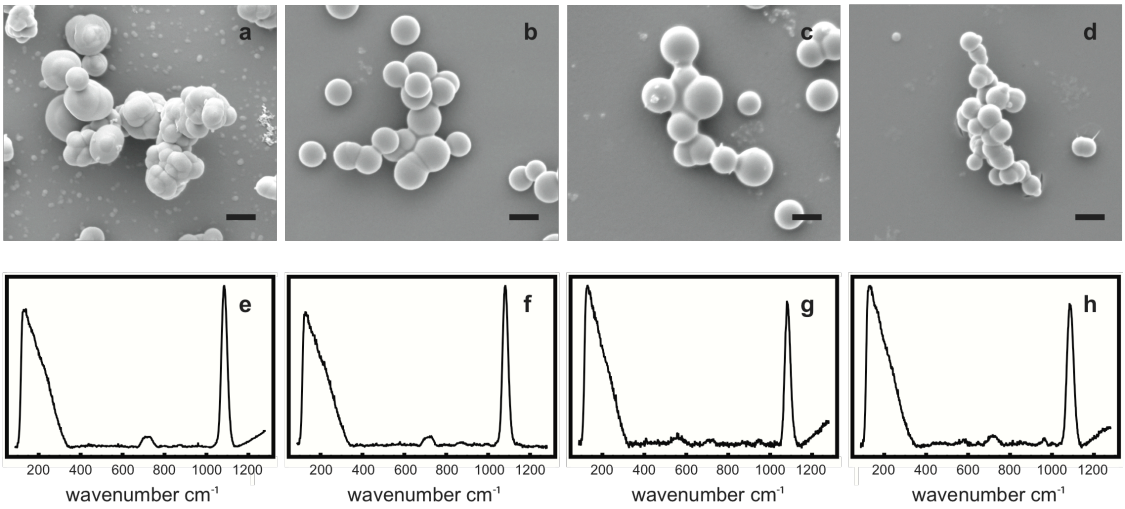

Figure S.2.1. SEM images of particles produced from solutions with Mg/Ca = 4.0 with A) no impurities; B) 0.025M aspartic acid; C) 0.025M glutamic acid; and D) 0.025 oxydiacetic acid (scale bars = 1μM). Particles have smooth and spherical morphologies indicative of amorphous carbonates. These samples were prepared by precipitation onto glass slides and coated with 8nm Pd-Au, and then imaged using a FEI Quanta FE-SEM, operated at 5kV. Raman spectra of particles produced from solutions with Mg/Ca = 4.0 that contained E) no impurities; F) 0.025M aspartic acid; G) 0.025M glutamic acid; and H) 0.025 oxydiacetic acid. All spectra show peak broading of v1 (~1085 cm-1) and v4 (~714 cm-1) and the absence of lattice modes at (~155 cm-1) and (~270 cm-1) that is characteristic of amorphous carbonates. Spectra were collected on a JY Horiba LabRam HR equipped with a 632nm HeNe using an Olympus 100X objective (N.A. = 0.9). 300s collection times were used.

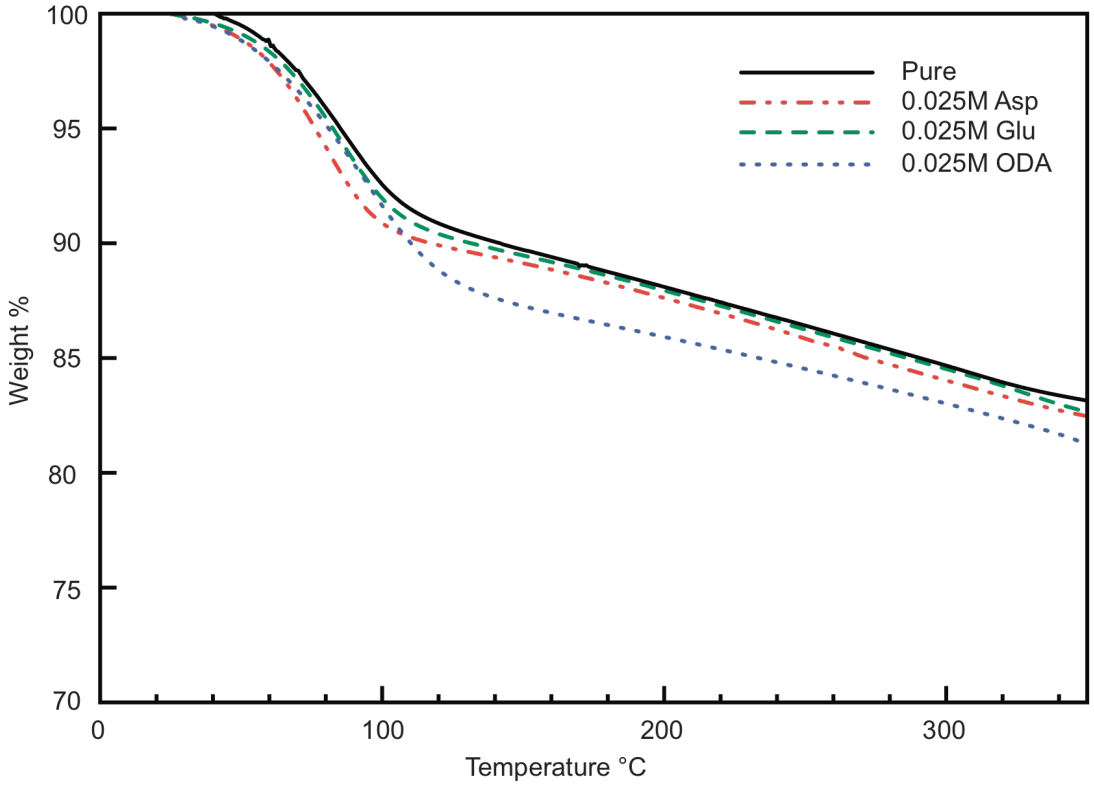

Figure S.2.2 Thermogravimetric analysis performed on a TA-TGA 2950 of particles filtered from solutions with Mg/Ca = 4.0, washed in ethanol and dried under vacuum overnight. ACC prepared in solutions without impurities (Pure), 0.025M aspartic acid (Asp), and 0.025M glutamic (Glu) yielded particles with approximately 14% weight loss between ambient and 250 °C. In solutions with 0.025M oxydiacetic acid (ODA) particles show an approximately 15.5% weight loss between ambient and 250 °C. The data demonstrates a stoichiometery of approximately one water molecule per calcium carbonate.

7. References

Aizenberg, J., Lambert, G., Addadi, L., and Weiner, S., 1996. Stabilization of amorphous calcium carbonate by specialized macromolecules in biological and synthetic precipitates. *Advanced Materials* **8**, 222-226.

Anderegg, G., Arnaud-Neu, F., Delgado, R., Felcman, J., and Popov, K., 2005. Critical evaluation of stability constants of metal complexes of complexones for biomedical and environmental applications. *Pure Appl. Chem.* **77**, 1445-1495.

Beard, N. A., Laver, D. R., and Dulhunty, A. F., 2004. Calsequestrin and the calcium release channel of skeletal and cardiac muscle. *Progress in Biophysics and Molecular Biology* **85**, 33-69.

Beniash, E., Aizenberg, J., Addadi, L., and Weiner, S., 1997. Amorphous calcium carbonate transforms into calcite during sea urchin larval spicule growth. *Proceedings of the Royal Society of London Series B-Biological Sciences* **264**, 461-465.

Berner, R. A., 1975. The role of magnesium in the crystal growth of calcite and aragonite from sea water. *Geochim. Cosmochim. Acta* **39**, 489-494.

Burton, W. K., Cabrera, N., and Frank, F. C., 1951. The growth of crystals and the equilibrium structure of their surfaces. *Philosophical Transactions of the Royal Society A* **243**, 299-358.

Carter, P. W. and Mitterer, R. M., 1978. Amino acid composition of organic matter associated with carbonate and non-carbonate sediments. *Geochim. Cosmochim. Acta* **42**, 1231-1238.

Chave, K. E., Deffeyes, K. S., Weyl, P. K., Garrels, R. M., and Thompson, M. E., 1962. Observations on the Solubility of Skeletal Carbonates in Aqueous Solutions. *Science* **137**, 33-34.

Cheng, X., Varona, P. L., Olszta, M. J., and Gower, L. B., 2007. Biomimetic synthesis of calcite films by a polymer-induced liquid-precursor (PILP) process: 1. Influence and incorporation of magnesium. *J. Cryst. Growth* **307**, 395-404.

Elhadj, S., De Yoreo, J. J., Hoyer, J. R., and Dove, P. M., 2006. Role of molecular charge and hydrophilicity in regulating the kinetics of crystal growth. *Proc. Natl. Acad. Sci. U. S. A.* **103**, 19237-19242.

Falini, G., Gazzano, M., and Ripamonti, A., 1996. Magnesium calcite crystallization from water-alcohol mixtures. *Chemical Communications*, 1037-1038.

Folk, R. L. and Land, L. S., 1975. Mg/Ca ratio and salinity - controls over crystallization of dolomite. *Bulletin-American Association of Petroleum Geologists* **59**, 60-68.

Foresman, J. B., Keith, T. A., Wiberg, K. B., Snoonian, J., and Frisch, M. J., 1996. Solvent effects .5. Influence of cavity shape, truncation of electrostatics, and electron correlation ab initio reaction field calculations. *J. Phys. Chem.* **100**, 16098-16104.

Forster, P. M. and Cheetham, A. K., 2004. The role of reaction conditions and ligand flexibility in metal-organic hybrid materials - examples from metal diglycolates and iminodiacetates. *Microporous Mesoporous Mat.* **73**, 57-64.

Frisch, M. J., Trucks, G. W., Schlegel, H. B., Scuseria, G. E., Robb, M. A., Cheeseman, J. R., Montgomery, J., J. A., Vreven, T., Kudin, K. N., Burant, J. C., Millam, J. M., Iyengar, S. S., Tomasi, J., Barone, V., Mennucci, B., Cossi, M., Scalmani, G., Rega, N., Petersson, G. A., Nakatsuji, H., Hada, M., Ehara, M., Toyota, K.,

Fukuda, R., Hasegawa, J., Ishida, M., Nakajima, T., Honda, Y., Kitao, O., Nakai, H., Klene, M., Li, X., Knox, J. E., Hratchian, H. P., Cross, J. B., Bakken, V., Adamo, C., Jaramillo, J., Gomperts, R., Stratmann, R. E., Yazyev, O., Austin, A. J., Cammi, R., Pomelli, C., Ochterski, J. W., Ayala, P. Y., Morokuma, K., Voth, G. A., Salvador, P., Dannenberg, J. J., Zakrzewski, V. G., Dapprich, S., Daniels, A. D., Strain, M. C., Farkas, O., Malick, D. K., Rabuck, A. D., Raghavachari, K., Foresman, J. B., Ortiz, J. V., Cui, Q., Baboul, A. G., Clifford, S., Cioslowski, J., Stefanov, B. B., Liu, G., Liashenko, A., Piskorz, P., Komaromi, I., Martin, R. L., Fox, D. J., Keith, T., Al-Laham, M. A., Peng, C. Y., Nanayakkara, A., Challacombe, M., Gill, P. M. W., Johnson, B., Chen, W., Wong, M. W., Gonzalez, C., and Pople, J. A., 2004. Gaussian 03, revision C.02. Gaussian, Inc., Wallingford, CT.

Fu, G., Qiu, S. R., Orme, C. A., Morse, D. E., and De Yoreo, J. J., 2005. Acceleration of calcite kinetics by abalone nacre proteins. *Advanced Materials* **17**, 2678-2683.

Gebauer, D., Volkel, A., and Colfen, H., 2008. Stable Prenucleation Calcium Carbonate Clusters. *Science* **322**, 1819-1822.

Gonzalez-Castro, M. J., Lopez-Hernandez, J., Simal-Lozano, J., and Oruna-Concha, M. J., 1997. Determination of amino acids in green beans by derivatization with phenylisothiocianate and high-performance liquid chromatography with ultraviolet detection. *J. Chromatogr. Sci.* **35**, 181-185.

Gotliv, B. A., Addadi, L., and Weiner, S., 2003. Mollusk shell acidic proteins: In search of individual functions. *ChemBioChem* **4**, 522-529.

Gotliv, B. A., Kessler, N., Sumerel, J. L., Morse, D. E., Tuross, N., Addadi, L., and Weiner, S., 2005. Asprich: A novel aspartic acid-rich protein family from the prismatic shell matrix of the bivalve Atrina rigida. *ChemBioChem* **6**, 304-314.

Grirrane, A., Pastor, A., Alvarez, E., and Galindo, A., 2005. Magnesium dicarboxylates: First structurally characterized oxydiacetate and thiodiacetate magnesium complexes. *Inorg. Chem. Commun.* **8**, 453-456.

Grirrane, A., Pastor, A., Alvarez, E., Moyano, R., and Galindo, A., 2007. Structural diversity of thiodiacetate compounds of group II metals: Synthesis and X-ray characterization of 2D coordination polymers of calcium and strontium. *Inorg. Chem. Commun.* **10**, 1125-1128.

Han, T. Y. J. and Aizenberg, J., 2008. Calcium carbonate storage in amorphous form and its template-induced crystallization. *Chem. Mater.* **20**, 1064-1068.

Kowacz, M. and Putnis, A., 2008. The effect of specific background electrolytes on water structure and solute hydration: Consequences for crystal dissolution and growth. *Geochim. Cosmochim. Acta* **72**, 4476-4487.

Levi, Y., Albeck, S., Brack, A., Weiner, S., and Addadi, L., 1998. Control over aragonite crystal nucleation and growth: An in vitro study of biomineralization. *Chemistry-a European Journal* **4**, 389-396.

Lowenstam, H. A. and Weiner, S., 1989. *On Biomineralization*. Oxford University Press, New York.

Ma, Y., Cohen, S. R., Addadi, L., and Weiner, S., 2008. Sea urchin tooth design: An "All-Calcite" polycrystalline reinforced fiber composite for grinding rocks. *Advanced Materials* **20**, 1555-1559.

Mackenzie, F. T., Bischoff, W. D., Bishop, F. C., Loijens, M., Schoonmaker, J., and Wollast, R., 1983. Magnesian calcites; low-temperature occurrence, solubility and solid-solution behavior. *Reviews in Mineralogy and Geochemistry* **11**, 97-144.

Nash, K. L., Horwitz, E. P., Gatrone, R. C., and Rickert, P. G., 1991. The effect of ligand rigidity on the stability of Europium(III) complexes with substituted diglycolic acids*19th Conf on Rare Earth Research*. Elsevier Science Lausanne, Lexington, Ky.

Piana, S., Jones, F., and Gale, J. D., 2007. Aspartic acid as a crystal growth catalyst. *CrystEngComm* **9**, 1187-1191.

Politi, Y., Arad, T., Klein, E., Weiner, S., and Addadi, L., 2004. Sea urchin spine calcite forms via a transient amorphous calcium carbonate phase. *Science* **306**, 1161-1164.

Politi, Y., Metzler, R. A., Abrecht, M., Gilbert, B., Wilt, F. H., Sagi, I., Addadi, L., Weiner, S., and Gilbert, P., 2008. Transformation mechanism of amorphous calcium carbonate into calcite in the sea urchin larval spicule. *Proc. Natl. Acad. Sci. U. S. A.* **105**, 17362-17366.

Pouget, E. M., Bomans, P. H. H., Goos, J., Frederik, P. M., de With, G., and Sommerdijk, N., 2009. The Initial Stages of Template-Controlled CaCO3 Formation Revealed by Cryo-TEM. *Science* **323**, 1555-1458.

Raz, S., Hamilton, P. C., Wilt, F. H., Weiner, S., and Addadi, L., 2003. The transient phase of amorphous calcium carbonate in sea urchin larval spicules: The involvement of proteins and magnesium ions in its formation and stabilization. *Adv. Funct. Mater.* **13**, 480-486.

Raz, S., Weiner, S., and Addadi, L., 2000. Formation of high-magnesian calcites via an amorphous precursor phase: Possible biological implications. *Advanced Materials* **12**, 38-42.

Robach, J. S., Stock, S. R., and Veis, A., 2006. Mapping of magnesium and of different protein fragments in sea urchin teeth via secondary ion mass spectroscopy. *J. Struct. Biol.* **155**, 87-95.

Sanchez-Roman, M., Vasconcelos, C., Schmid, T., Dittrich, M., McKenzie, J. A., Zenobi, R., and Rivadeneyra, M. A., 2008. Aerobic microbial dolomite at the nanometer scale: Implications for the geologic record. *Geology* **36**, 879-882.

Schmidt, M., Xeflide, S., Botz, R., and Mann, S., 2005. Oxygen isotope fractionation during synthesis of CaMg-carbonate and implications for sedimentary dolomite formation. *Geochim. Cosmochim. Acta* **69**, 4665-4674.

Segev, E. and Erez, J., 2006. Effect of Mg/Ca ratio in seawater on shell composition in shallow benthic foraminifera. *Geochemistry Geophysics Geosystems* **7**, 8.

Silliman, B., 1846. On the chemical composition of calcareous corals. *Am. J. Sci.* **1**, 189-199.

Stephenson, A. E., DeYoreo, J. J., Wu, L., Wu, K. J., Hoyer, J., and Dove, P. M., 2008. Peptides Enhance Magnesium Signature in Calcite: Insights into Origins of Vital Effects. *Science* **322**, 724-727.

Van Lith, Y., Warthmann, R., Vasconcelos, C., and McKenzie, J. A., 2003. Microbial fossilization in carbonate sediments: a result of the bacterial surface involvement in dolomite precipitation. *Sedimentology* **50**, 237-245.

Vasconcelos, C. and McKenzie, J. A., 1997. Microbial mediation of modern dolomite precipitation and diagenesis under anoxic conditions (Lagoa Vermelha, Rio de Janeiro, Brazil). *Journal of Sedimentary Research* **67**, 378-390.

Walter, L. M. and Hanor, J. S., 1979. Ortho phosphate - effect on the relative stability of aragonite and magnesian calcite during early diagenesis. *Journal of Sedimentary Petrology* **49**, 937-944.

Warthmann, R., van Lith, Y., Vasconcelos, C., McKenzie, J. A., and Karpoff, A. M., 2000. Bacterially induced dolomite precipitation in anoxic culture experiments. *Geology* **28**, 1091-1094.

Weber, J. N., 1969. The incorporation of magnesium into the skeletal calcites of echinoderms. *Am. J. Sci.* **267**, 537-566.

Weiner, S. and Dove, P. M., 2003. An overview of biomineralization processes and the problem of the vital effect. *Reviews in Mineralogy and Geochemistry* **54**, 1-29.

Weiner, S., Levi-Kalisman, Y., Raz, S., and Addadi, L., 2003. Biologically formed amorphous calcium carbonate. *Connective Tissue Research* **44**, 214-218.

Weiss, I. M., Tuross, N., Addadi, L., and Weiner, S., 2002. Mollusc larval shell formation: Amorphous calcium carbonate is a precursor phase for aragonite. *J. Exp. Zool.* **293**, 478-491.

Wright, D. T. and Wacey, D., 2005. Precipitation of dolomite using sulphate-reducing bacteria from the Coorong Region, South Australia: significance and implications. *Sedimentology* **52**, 987-1008.

Chapter Three

Control of mineralization pathway on Mg content of calcite and consequences for sedimentary environments

Dongbo Wang[1], Takuya Echigo[1,2], James J. De Yoreo[3], Mitsuhiro Murayama[4] and Patricia M. Dove[1]

[1]*Department of Geosciences, Virginia Tech, Blacksburg VA 24061 USA*

[2] *Japan International Research Center for Agricultural Sciences, Ohwashi 1-1, Tsukuba 305-8686, Ibaraki, Japan*
[3]*Molecular Foundry, Lawrence Berkeley National Laboratory, Berkeley, CA 94720*
[3]*Department of Materials Science, Virginia Tech, Blacksburg VA 24061 USA*

A manuscript in preparation for submission to *Science*

1. Summary

Extensive occurrences of high magnesium carbonates in the early geologic record suggest a rich history of inorganic and biological origins. Efforts to reconstruct paleoenvironmental conditions from these deposits are hindered by the need for process-based models that explain observed shifts in carbonate chemistry and textures. We show the pathway to mineralization has distinct controls on calcite composition and morphology. Calcites form by the classical crystal growth process of step propagation as individual crystal from low Mg solutions (Mg:Ca = 1-3). As solution Mg:Ca is increased, the mineralization process undergoes an abrupt transition to a nonclassical mechanism whereby a precursor phase of amorphous calcium carbonate (ACC) forms and then transforms into sheets of calcite mesocrystals. The mesocrystalline products are high-Mg calcites of dolomitic composition with approximately constant Mg contents (35-50 %) and sizes (30-60 nm) regardless of solution Mg:Ca, the addition of aspartic acid, or of sulfate; suggesting possible energetic controls of Mg content on the maximum crystal size that can develop. Observations that carboxylated surfaces increase the quantity of ACC that initially forms (and the calcite product) indicate organic-rich environments promote the extent of mineralization without requiring active biological involvement. The mesocrystalline structures produced by the ACC pathway are similar to geologically young Coorong dolomites, suggesting that this pathway may be responsible for naturally occurring high-Mg carbonates. The findings suggest a physical basis for shifts in textures and patterns of calcification may be rooted in mineralization pathways and their dependence upon environmental conditions.

2. Body

The Proterozoic Era (2500 - 542 Ma) is a unique interval of Earth history that marks the transition from an inorganic to biology-dominated world. This period is characterized by extensive carbonate sedimentation with the massive deposition of dolomites ($CaMg(CO_3)_2$), high-Mg carbonates, and limestones. Of particular interest is the widespread occurrences of stromatolites— attached and lithified carbonate structures that are widely associated with microbial activity (SPADAFORA et al., 2010). Stromatolites show distinct textures and compositions that change over a period of approximately 200

Ma (GROTZINGER and KNOLL, 1999) Some studies interpret these structures as responses to changes in microbial *communities* (SPADAFORA et al., 2010) while an alternative perspective argues the distinct textures are 'environmental dipsticks' or proxies for the evolution of environmental *conditions* (GROTZINGER and KNOLL, 1999). After almost 100 years of research, the need for a specific process-based model continues (GROTZINGER and KNOLL, 1999).

Another feature of many Proterozoic carbonates that has received considerable attention is their remarkably high-Mg contents. Enormous deposits exist of dolomite and 'calcites of dolomitic composition' containing 30-50 mol% Mg. Efforts to interpret their formation have centered upon the assumption that carbonate formation occurs by the ion-by-ion attachment of solutes to the step edges of mineral surfaces by the classical terrace-ledge-kink (TLK) model of crystal growth. While TLK theory (BURTON et al., 1951) has provided the foundation for designing and interpreting many studies of carbonate deposition, a long-standing enigma is the inability of this growth process to produce low temperature carbonates with more than 10-12 mol% Mg (FOLK and LAND, 1975; MORSE et al., 2007).

Similarly high Mg levels are found in many types of calcareous skeletons. Certain algae and echinoderm species produce carbonate biominerals with up to 30 mol% $MgCO_3$ (RAZ et al., 2003; WEBER, 1969; WEINER et al., 2003); while the teeth of sea urchins can contain as much as 50 mol% $MgCO_3$ (MA et al., 2008; ROBACH et al., 2006). Recent advances in our understanding of how biominerals are produced by organisms of diverse phyla show that many skeletal structures mineralize by a two-stage process that begins with the accumulation of an amorphous calcium carbonate (ACC) intermediate phase that later transforms into one or more crystalline carbonate polymorphs such as calcite or aragonite (BENIASH et al., 1997; RAZ et al., 2000). In vitro studies show this ACC material is readily produced under conditions of high supersaturations (BRECEVIC and NIELSEN, 1989). While pure ACC is highly unstable and rapidly transforms to calcite, the Mg-bearing ACC, such as found in calcifying tissues, is persistent as a metastable phase for substantial periods until the transformation is triggered by local changes in chemistry and/or conditions (TAO et al., 2009; WANG et al., 2009). High-resolution images show this ACC transforms into highly co-aligned nanocrystals to produce the

complex superstructures we know as skeletal biominerals (KILLIAN et al., 2009; OAKI et al., 2006). But also, many of these products contain Mg levels that are not possible through TLK classical crystal growth processes (STEPHENSON et al., 2008). Structural studies show these materials are assemblies of 5-100 nm nanoparticles that can have significant crystallographic co-alignment (OAKI and IMAI, 2006; OAKI et al., 2006; SETHMANN et al., 2006; VIELZEUF et al., 2010). A wide variety of minerals and other inorganic materials are now recognized to form by this two-step 'mesocrystal process' into structures similar to those found here from the high Mg conditions (COLFEN and ANTONIETTI, 2008; MELDRUM and COLFEN, 2008; SONG and COLFEN, 2010; ZHOU and O'BRIEN, 2008). Because these structures are reactive intermediates along the nonclassical crystallization pathway toward eventual fusion of nanoparticles, their occurrences have been largely overlooked.

Recent insights into dolomite formation suggest a similar ACC to mesocrystal pathway may be the missing link to interpreting origins and textures of high-Mg carbonate deposits. For example, an experimental study using X-ray diffraction coupled with morphological analysis reported highly ordered dolomites formed at 218°C began as disordered nanoparticle assemblies with ‘mound’ like morphologies (KACZMAREK and SIBLEY, 2007). Furthermore, studies that investigated these disordered materials of produced under lower temperatures emphasized the importance of amorphous precursors in such materials (KELLEHER and REDFERN, 2002; SCHMIDT et al., 2005). The presence of disordered crystalline and amorphous phases was noted by the authors as a plausible clue to why dolomites are difficult to form at low temperatures by classical growth process. In light of findings that high-Mg ACC is readily produced by organisms (ADDADI et al., 2003) and can be stabilized for significant periods (LEVI et al., 1998; RAZ et al., 2000), evidence from these studies raise the question of whether the formation of a high-Mg ACC phase is the requisite pathway to producing 'calcites of dolomitic composition' and eventually, to ordered dolomites. That is, the composition and textures of some sedimentary carbonates may be explained by a mineralization process that involves ACC formation and transformation by a nucleation-dominated pathway, similar to the process that occur in skeleton formation. Insights from these and other observations, lead us to hypothesize that i) sedimentary carbonates are formed by both classical and nonclassical

pathways; ii) the high-Mg carbonates that form at low temperatures are the products of a two step, nonclassical process involving ACC; and iii) the textures, compositions and morphologies of crystalline products reflect pathway-specific processes and conditions of formation.

To investigate the idea that a similar two-step process explains the formation of Mg-rich carbonates, we precipitated ACC onto silica coverslips using solutions that varied the Mg/Ca ratio from 0.0 to 6.0 (see Methods). Additional experiments were also conducted that contained aspartate ($C_4H_6NO_4^-$) or sulfate (SO_4^{2-}) at 0.05 M and 0.025 M because these molecules are implicated in promoting Mg content of the ACC (WANG et al., 2009) or inhibiting dolomite formation (BAKER and KASTNER, 1981. All ACC precipitates initially exhibited the typical spherical morphology and characteristic Raman spectra and later transformed to continuous sheets of ACC (**Fig S.3.1**). ACC transformed to crystalline products after aging for 3-5 days in closed vessels at 100% humidity at 40°C. When the Mg/Ca ratio was increased from 0.0 to 6.0, the time to transformation increased from 6 hours to 5 days. Calcites transformed from ACC in the absence of Mg exhibited the expected rhombic morphology typical of classical step growth (**Fig. 3.1A**). In the presence of aspartate and sulfate, similar but rounded rhombic structures (**Fig. 3.1BC**) also formed as reported previously (ORME et al., 2001). As Mg was introduced to the solution (Mg/Ca = 1.0 - 3.0), the ACC transformed into calcites with an elongated form (**Fig. 3.1DEF**) or spherical forms consistent with step-dominated growth (FALINI et al., 1998; HAN et al., 2005). Closer inspection, however, shows a composite of oriented 400-500 nm crystallites whose morphologies are similarly elongated (**inset 3.1BF**).

As the Mg/Ca of the initial solution is increased to ≥ 4.0, the transformation of ACC produces calcites with a distinctly different macromorphology and texture that indicate a change in the predominant mineralization process. Aggregates of nanoparticles are formed in low-relief, disc-shaped structures that lack evidence of crystallographic control. These 30-80 nm particles are 100X smaller than those produced in at lower Mg conditions, regardless of the presence of sulfate or aspartate.

Additional evidence for a transition in the mineralization process is seen in the compositions of the calcites that form. Calcites produced from low Mg/Ca solutions (0.0 to 3.0) show a linear increase in mol% $MgCO_3$ indicative of the fractionation behavior

predicted by thermodynamic theories for a $Ca_{1-x}Mg_xCO_3$ solid solution produced by classical crystal growth (**Fig 3.2A**). Compositions show a single trend in control and sulfate or the aspartate additive experiments (**Fig 3.2AB**). In contrast, as Mg/Ca of the mineralization environment exceeds >3.0-4.0, the Mg content of transformed calcites abruptly shifts to higher *plateau* values of 35-40% mol% $MgCO_3$ (**Fig 3.2A).** Similar compositions are measured in calcites that transform in the presence of aspartate (**Fig 3.2A**) or sulfate (**Fig 3.2B**) and the data suggest the possibility these molecules promote further Mg enrichment to 40-50 mol% $MgCO_3$.

Analysis of the data suggests the marked changes in morphology, particle size, and composition that occur when Mg/Ca levels exceed 3.0 are a consequence of Mg inhibiting calcite growth by step propagation. At higher Mg/Ca levels, calcite nucleates but the rate of growth is very slow compared to the rate of nucleation, causing a transition to the nucleation-dominated process. This interpretation is supported by a previous study showing that rates of calcite growth decline to zero as the resulting solid solution acquires a higher apparent solubility, resulting in a lower chemical driving force to step propagation (DAVIS et al., 2000; WASYLENKI et al., 2005a). By evaluating the Mg level that gives zero growth for experiments conducted across a series of supersaturation states, we find that step growth is inhibited at an Mg/Ca ratio of approximately 2-3 for conditions where the supersaturation state with respect to calcite is equal to ACC solubility. This value corresponds remarkably well with the Mg/Ca range of 3-4 where the change in mineralization mechcanism occurs in these experiments. This model for progressively Mg-inhibited calcite growth is also consistent with our experimental observations that the time to ACC transformation increases with Mg content and measurements showing an inverse relationship between the size of calcite crystals and their Mg content (**Fig S.3.2**).

Insights from previous studies and findings herein suggest a conceptual framework for understanding calcite mineralization processes in terms of supersaturation state and the Mg/Ca conditions. First, it is known that calcite growth occurs by the classical process of ion-by-attachment to step edges under conditions of low supersaturations and low-Mg levels (**Fig 3.4, lower left**) (DAVIS et al., 2000; STEPHENSON et al., 2008; WASYLENKI et al., 2005a; WASYLENKI et al., 2005b). As Mg

concentration increases, in situ experiments show the rate of growth by step propagation decreases to zero, effectively inhibiting calcite growth, at Mg/Ca ratios of approximately 0.9 (DAVIS et al., 2000; STEPHENSON et al., 2008) to 2.0. These values are consistent with extensive evidence that aragonite formation becomes favored over calcite when Mg/Ca is >2.0 in seawater (**Fig 3.4, lower right**) (HARDIE, 1996; LEE and MORSE, 2010).

When one considers that ACC forms as a reactive carbonate phase in highly supersaturated environments, additional pathways to calcification become possible as this intermediate transforms to crystalline products. The result is additional morphological texures and, under some conditions, very high-Mg calcites. The transformation of low Mg ACC produces calcite particles that grow at a rate that is inversely related to Mg content (**Fig 3.4**, **upper left**). Compositionally, these crystallites show a classical solid solution dependence on solution chemistry and in situ observations suggest the transformation occurs as an ACC dissolution/calcite growth process (**SI movie**). However, because their relatively small size and number of discrete particles leads us to describe this as a hybrid of the step growth and nucleation-dominated processes. In contrast, the combination of high Mg/Ca and a high supersaturation state environment produces calcite nanoparticles by a nucleation-dominated process indicative of a true mesocrystal pathway (**Fig 3.4**, **upper right**). Because subsequent growth of these nanoparticles is prohibited by the Mg-rich environment, their Mg signatures no longer obey the fractionation rules of step growth (**Fig 3.2AB)**. Given the transient nature of nucleation, we suggest the Mg signatures that result from this type of mineralization are likely governed by kinetic factors.

This qualitative 'map' of predominant mineralization processes (**Fig 3.4)** suggests the physical basis of some carbonate compositions and textures reported in experimental and field studies. First, extensive efforts to produce dolomites have been unsuccessful (LAND, 1998) because early studies favored conditions that promoted classical step growth. The formation of Mg-rich carbonates at low temperatures requires the ability to nucleate high-Mg nanoparticles whose subsequent growth is inhibited— an outcome that becomes possible under conditions of both high supersaturations and high Mg/Ca. Neither extreme levels of solution Mg/Ca = 20 - 40, or extreme salinities are required to produce carbonates that approach a dolomitic composition as previously suggested (FOLK

and LAND, 1975).

Another test is found in the structure and composition of natural disordered dolomites from the Coorong Lakes of Southern Australia (SKINNER, 1963). This locality, whose waters have Mg/Ca = 5-20 and very high supersaturations (WRIGHT and WACEY, 2005) can be thought of as the 'evolutionary link' between the disordered dolomites of geologically young sedimentary environments and ordered dolomites in the rock record. Coorong carbonates are comprised of 1-3 μM particles that express pseudo facets consistent with the dolomite structure (**Fig 3.3C**) and TEM analyses from a previous study (REEDER, 1992). SAED spot analysis shows the pseudofacets likely arise from partial ordering and co-alignment of the particles into 100-150 nm subdomains along two predominant (ROSEN et al., 1988) orientations (**Fig 3C inset**). These properties are consistent with **Fig 3.4 upper right** and suggest the transformation of this natural material to a true dolomite is underway, possibly by a two-step process (KASHCHIEV et al., 2005).

The distinctive calcite morphologies, particle sizes, and compositions that characterize the regions in **Fig 3.4** suggest that some of the textures and compositions recorded in Proterozic carbonates can be interpreted to constrain paleoenvironmental conditions that prevailed during that time. The idea is analogous to the concept of the 'environmental dipstick' that was proposed to interpret the structure and textures of stromatolite deposits (GROTZINGER and KNOLL, 1999). We ask if some of the textures recorded in carbonate rocks are the products of calcification by the two-step processes described herein. For example, the molar tooth deposits that uniquely characterize carbonate sediments worldwide over the 1.8 - 0.8 Ga period are comprised of an unusual crack-filling carbonate cement that is extremely fine grained, or microsparitic with a pelleted texture under cathodal luminescence. The spheroidal and optically syntaxial texture of infilled structures (GROTZINGER and KNOLL, 1999) suggests the that they were formed by a nucleation process analogous to the aggregates of nanoparticles and their high Mg levels described herein.

Similarly, the finely laminated carbonate deposits that become extensive by the Neoproterozoic (1000-542 Ma) (Knoll and Swett, 1990) may reflect a transition to calcification by a mesocrystalline process. Sheet-like aggregates of high-Mg

nanoparticles reported herein have morphological and compositional similar to the fine-grained lamellae that are extensively documented by petrographic studies. These comparisons are consistent with current models for the likely range of Mg/Ca values and their fluctuations during the Proterozic.

The most immediate obstacle to this interpretation is the issue of how the oceans could achieve the very high supersaturation states required to stabilize and precipitate large quantities of ACC. ACC solubility is approximately 120X that of calcite (BRECEVIC and NIELSEN, 1989). Although Mg^{2+} inhibits growth through shifts in thermodynamic driving force, low levels of Sr^{2+}, small molecules such as sulfate, and organics are true growth inhibitors that block step growth, in some cases at very low concentrations (ELHADJ et al., 2006; VAVOURAKI et al., 2008a; WASYLENKI et al., 2005b). These simple and preliminary comparisons suggest it may be time to revisit our 'understanding' of calcification. With the realization that nucleation-dominated mineralization processes should be considered in interpreting composition and textural patterns in geological deposits, a new view into the mechanistic basis for carbonate formation and possibly polymorph selection in geologic settings may emerge.

Finally, we note that sulfate has an insignificant influence on the composition or morphology of calcites formed by the classical or the two-step processes. This suggests the long-standing claim that dolomitic carbonates cannot form in high sulfate environments (BAKER and KASTNER, 1981) needs to be reassessed. Sulfate is known to inhibit the rate of calcite growth (VAVOURAKI et al., 2008b), but the data herein and anecdotal evidence from previous studies (KELLEHER and REDFERN, 2002; SANCHEZ-ROMAN et al., 2009; SCHMIDT et al., 2005) show that sulfate does not prohibit the formation of microbial and synthetic high-Mg carbonates that form via the mesocrystal pathway. It is also intriguing that aspartate, does not significantly influence the composition of the calcites that precipitate by the nucleation-dominated process. *To* further test this finding, an additional set of experiments were conducted on substrates terminated with charged carboxyl, COO^-, groups as simple proxies for charged bio-surfaces also increase the number (volume) of nanoparticles that nucleate (see **Methods**). For otherwise identical experimental conditions, compositions and macromorphology of these calcites were unchanged from the comparable experiments using silica glass

substrates. We did, however, find that charged substrates increased the particle density by approximately 100%. These findings show that direct microbial activity is not a requirement for producing high-Mg calcites, but raise the question of whether some organic-rich environments passively promote calcification (CARTER and MITTERER, 1978). In stromatolites for example, a significant increase in the quantity of calcite nanoparticles that are nucleated could locally produce extensive fine-grained deposits, thus providing a simple a self-reinforcing mechanism for rapidly extending these structures. In conclusion, while the simple conceptual model reported herein raises many unanswered questions, and suggests the potential of a mesocrystal pathway to calcification to reconcile a number of long-standing enigmas in the geological and experimental literature.

3. Methods

Preparation of Self Assembled Monolayers: Carboxyl terminated self-assembled monolayers were produced using the methods of Han and Aizenberg (2005). 5mM of mercapto-undecanoic acid (MUA) (Sigma Alrich, 95%) was dissolved in anhydrous ethanol (Sigma Aldrich, 99.5%) and sonicated for 30 minutes. Cleaved Au substrates (800nm Au/5nm Ti/Si (100) prepared using standard Electron beam PVD) were placed overnight in the MUA solution, which were rinsed in anhydrous ethanol and then rinsed in deionized (DI) water (18.2 mΩ, Barnstead Nanopure) water.

Mineralization: Solutions were varied from Mg/Ca of 0 to 6, with the concentration of Ca held constant at 10mM. Solutions were prepared with $CaCl_2 \cdot 2H_2O$ (Sigma Aldrich, 99+%) and $MgCl_2$ (Sigma Alrich, 99%). The precipitates were produced using the ammonium carbonate diffusion method by dissolving 10g of $(NH_4)_2CO_3$ (Sigma Aldrich) in 20mL DI water in incubators a 40°C. Six replicates were produced at each condition by pipetting 3mL of solution into 10% nitric acid washed 6 well plates (BD Falcon). The precipitates were grown on acid/peroxide washed 18mm glass coverslips (Fisher Scientific) or MUA-SAM. After 1 day the ammonium carbonate solutions were removed and 4 days the precipitates were removed and washed with anhydrous ethanol (Sigma Aldrich, 99.5%).

Coorong Dolomite: Natural samples of Coorong Dolomite were sonicated in 30% peroxide for two hours and centrifuged for 10 minutes and ethanol washed. The samples

were dispersed on glass slides for XRD analysis and silicon for SEM analysis and FIB preparation.

Raman Spectroscopy: The Raman spectra were acquired on a JY Horiba (800 mm) LabRam HR with a 100x objective (N.A. = 0.9) equipped with a 632.81 nm HeNe laser emitting 15mW power at the source. The instrument was calibrated using a neon lamp (Newport Instruments, model 6032).

Standardized X-Ray Diffraction (XRD): Samples were analyzed on a PANyntical X'PERT PRO with Cu $K\alpha_1$ radiation operated at 45kV and 40mA from 20° – 60° 2θ at a scan speed of 0.02°/sec. $MgCO_3$ compositions were determined using the methods of Lumdsen (LUMSDEN, 1979) using a linear approximation of the calcite (104) peak position to the dolomite (104) peak position correlated to the composition of calcite 100% $CaCO_3$ and dolomite 50% $CaCO_3$ and 50% $MgCO_3$ using the methods of Lumsden (1979). All sample (104) peaks were corrected by the silicon (111) peak at 28.439° 2θ using a powdered silicon internal standard (NIST 640D), deposited by ethanol dispersion.

SEM: The samples were sputter coated with Au/Pd and imaged at 5kV on a FEI Quanta F600 or carbon coated and imaged on a FEI Helios 600 Nanolab.

TEM sample preparation:

All TEM samples were by established Focused Ion Beam (FIB) methods (LI et al., 2009) on a FEI Helios 600 Nanolab.

TEM SAED: TEM Selective Area Electron Diffraction patterns were collected on a Philips 420 operated at 120kV.

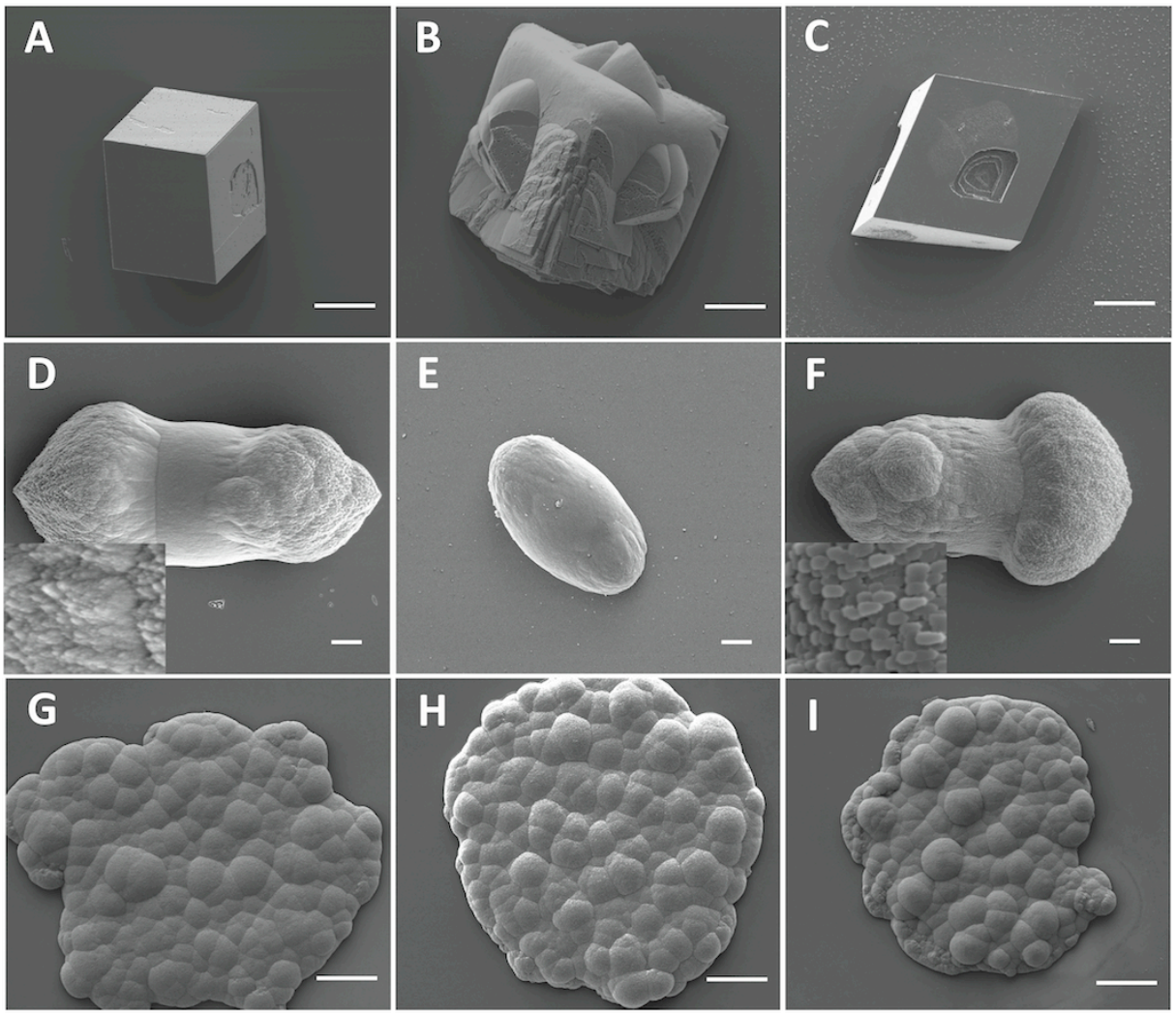

Fig. 3.1. Calcites transformed from ACC show a transition in morphology that demonstrate the change from a growth-dominated to nucleation-dominated process is primarily controlled by the Mg/Ca ratio of the mineralization environment. Calcites produced from solutions that contain Mg/Ca = 0 produce rhombic morphologies consistent with the classical calcite form in (**A**) control experiments (no additives); (**B**) 0.05 M Asp solutions that produce rhombs with rounded morphologies consistent with previous studies (ORME et al. 2001) and (C) 0.05 M sulfate solutions. In Mg/Ca = 2.0, calcite morphology shifts to elongated crystal assemblages in (**D**) control conditions that show xx nm 'needles' at the ends of the structures (**inset**); (**E**) solutions that also contain 0.05 M Asp; or (**F**) 0.05 M sulfate that produces discrete elongated calcite crystals about 500 nm in length (**inset)**. As Mg/Ca ratio is increased to 5.0, the transformed calcites show an abrupt change in morphology to disc-like aggregates of discrete nanoparticles in (**G**) control; (**H**) 0.05 M Asp; and (**I**) 0.05 M sulfate. All scale bars = 20μM.

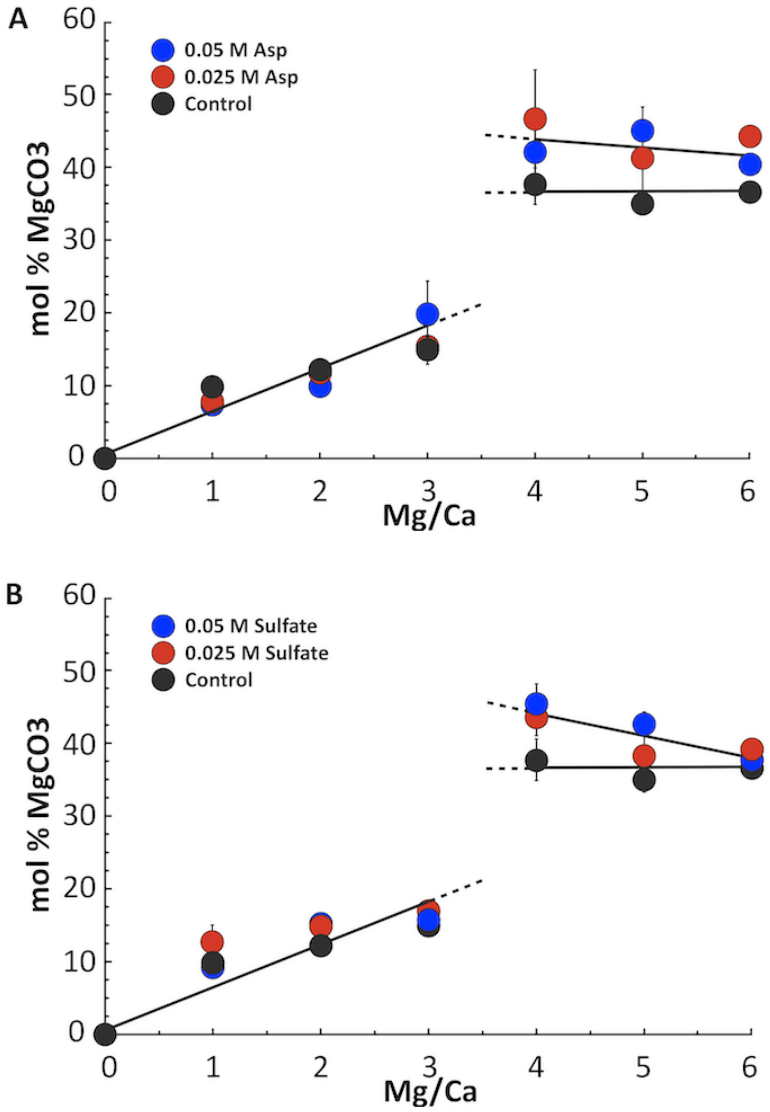

Fig 3.2. Mg uptake into calcite follows a linear partitioning relationship to the Mg/Ca ratio of the solution over the range of Mg/Ca = 0.0 - 3.0 that is consistent with classical crystal growth. At higher Mg levels, the . At Mg/Ca = 4 and greater, Mg contents of the solid are compositionally equivalent to dolomites and are no longer positively correlated to the Mg/Ca of the solution. The relationship is true in the controls (black symbols) and in (**A**) calcite mineralized with [Asp] = 0.05M (blue) and [Asp] = 0.025M (red), with a significant increase in Mg content of up to 10 mol% as compared to the control. (**B**) The same trend exist in [SO_4] = 0.05M (blue) and [SO_4] = 0.025M (red).

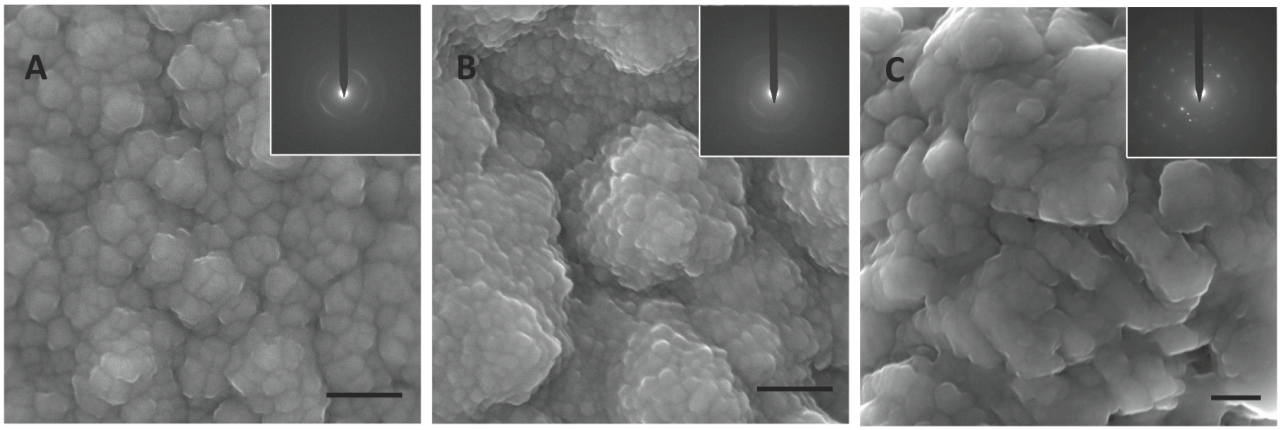

Fig 3.3. Surface morphology of synthetic and natural Ca-Mg carbonates illustrate aggregated nature of synthetic and modern dolomitic carbonates. All scale bars 200 nm. (**A**) Nanocrystal aggregates synthesized in control (no additives) solution at Mg/Ca = 5 are comprised of 58 ± 12 nm individual particles (35 mol% $MgCO_3$). (**B**) Sulfate solutions (0.05 M) produce smaller 33 ± 6.8 nm calcite nanoparticles (45 mol% $MgCO_3$), synthesized at solution Mg/Ca = 4, [SO4] = 0.05M, the discrete particle sizes are significantly smaller. (**Inset**) Arcs in SAED from both synthetic samples indicate partial co-alignment. (**C**) Coorong dolomite is similarly comprised of individual 1-3 μM particles with partial ordering into 100-150 nm subdomains that express macro-facets consistent with {104} termination. [452] zone axis SAED spot patterns (**inset**) confirm individual particles are highly co-aligned in two dominant orientations.

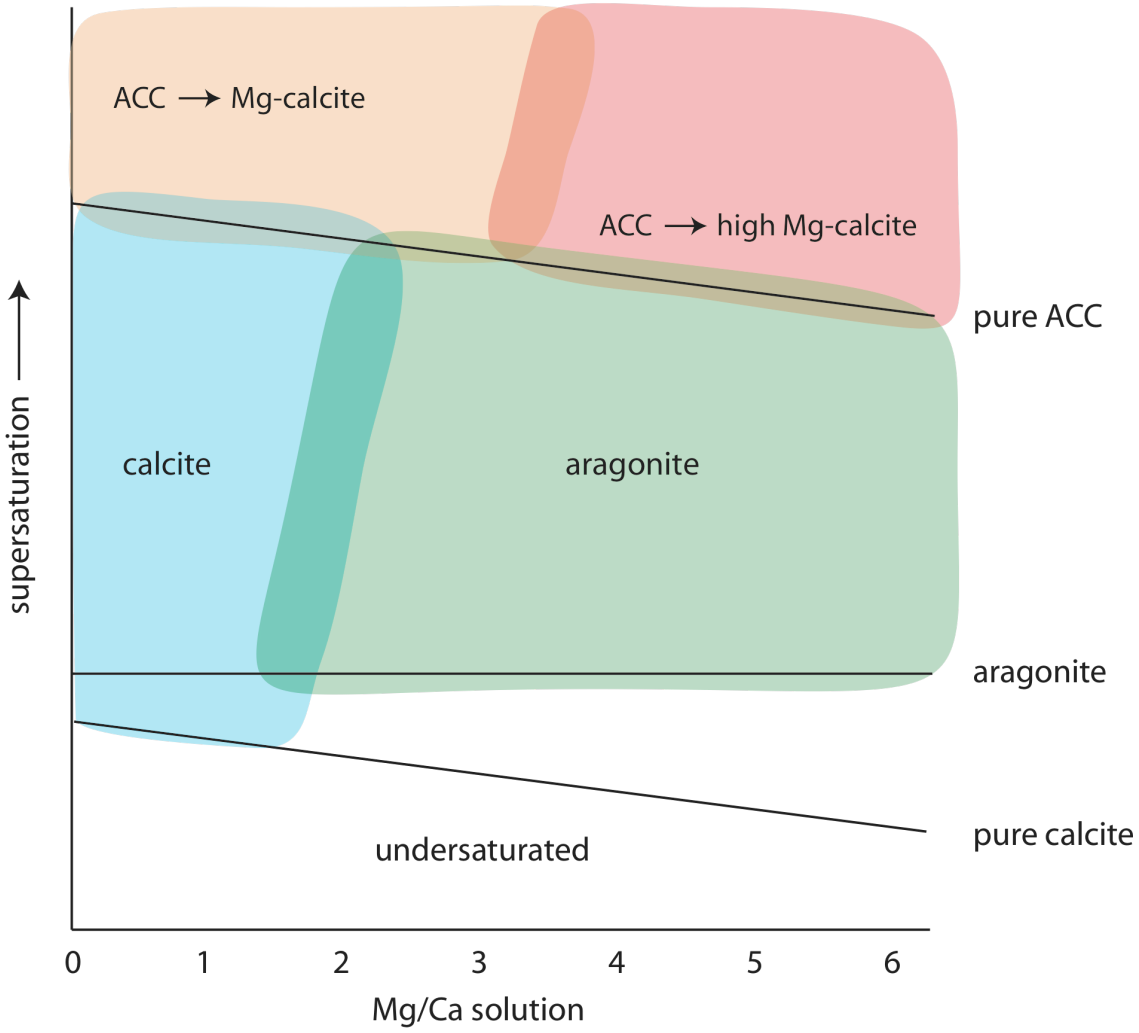

Fig 3.4. Qualitative 'process' diagram for calcium carbonates (**lower left**) Classical *growth* processes best described as ion-by-ion addition at terrace-ledge-kink sites of a calcite crystal. Mg/Ca ratios remain low enough to no completely inhibit calcite growth. Rates of growth greatly exceed nucleation rate. (**upper right**) Non-classical *nucleation* dominated processes that form mesocrystals of very high Mg-composition. Mg/Ca ratios are very high causing inhibition of calcite growth. Rates of growth are greatly exceeded by nucleation rates. (**upper left**) Hybrid processes occur, where ion-by-ion addition occurs along with nucleation processes. Rates of growth are similar to nucleation rate. (**lower right**) Aragonite nucleation and growth occurs. Mg/Ca ratios are high, inhibiting calcite growth, yet supersaturation is not high enough to nucleation a high Mg-calcite. Rates of aragonite nucleation exceed rate of calcite growth and nucleation.

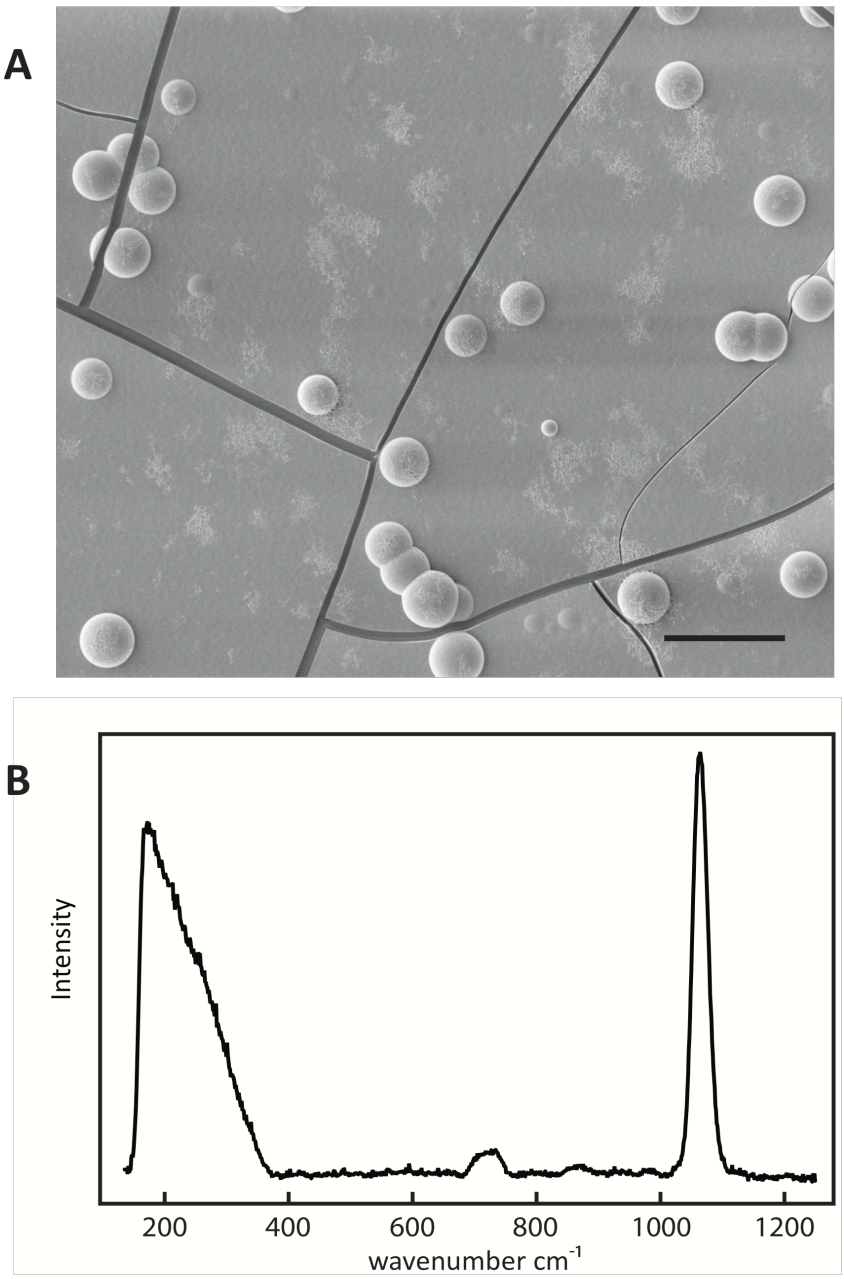

Fig 3.S.1. ACC film formed in Mg/Ca = 5, no additional impurities, characteristic of all samples formed in Mg/Ca > 3. SEM (**A**) shows characteristic sheets with mounds. Raman spectra (**B**) characteristic of Mg-ACC.

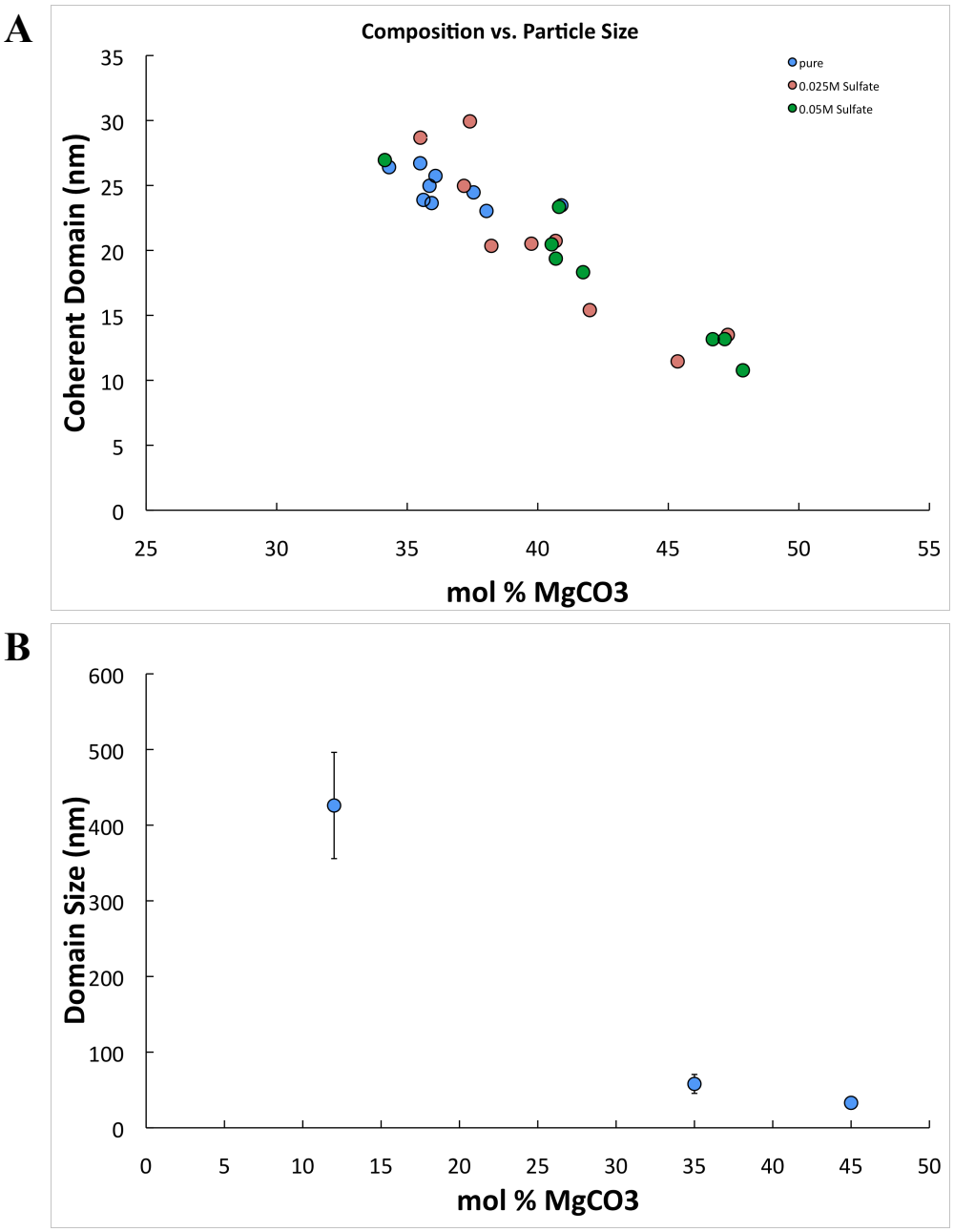

Fig 3.S.2 Composition of calcite is related to crystal size. (**A**) High Mg-calcites of 35-50 mol% $MgCO_3$, particle size is inversely related to magnesium content, that is particles with more Mg are smaller. Coherent domain size is calculated by Debye-Scherrer equation. (**B**) Mg-calcites of approximately 12 mol% mol% $MgCO_3$ representative of materials formed from a hybrid processes have much larger particle sizes (426 ± 76 nm), indicating that they still enlarge by growth processes. Particle size is directly obtained by SEM.

References

Addadi, L., Raz, S., and Weiner, S., 2003. Taking advantage of disorder: Amorphous calcium carbonate and its roles in biomineralization. *Advanced Materials* **15**, 959-970.

Baker, P. A. and Kastner, M., 1981. Constraints on the Formation of Sedimentary Dolomite. *Science* **213**, 214-216.

Beniash, E., Aizenberg, J., Addadi, L., and Weiner, S., 1997. Amorphous calcium carbonate transforms into calcite during sea urchin larval spicule growth. *Proceedings of the Royal Society of London Series B-Biological Sciences* **264**, 461-465.

Brecevic, L. and Nielsen, A. E., 1989. Solubility of amorphous calcium carbonate. *J. Cryst. Growth* **98**, 504-510.

Burton, W. K., Cabrera, N., and Frank, F. C., 1951. The growth of crystals and the equilibrium structure of their surfaces. *Philosophical Transactions of the Royal Society A* **243**, 299-358.

Carter, P. W. and Mitterer, R. M., 1978. Amino acid composition of organic matter associated with carbonate and non-carbonate sediments. *Geochim. Cosmochim. Acta* **42**, 1231-1238.

Colfen, H. and Antonietti, M., 2008. *Mesocrystal Systems*. John Wiley & Sons, Ltd.

Davis, K. J., Dove, P. M., and De Yoreo, J. J., 2000. The role of Mg2+ as an impurity in calcite growth. *Science* **290**, 1134-1137.

Elhadj, S., Salter, E. A., Wierzbicki, A., De Yoreo, J. J., Han, N., and Dove, P. M., 2006. Peptide controls on calcite mineralization: Polyaspartate chain length affects growth kinetics and acts as a stereochemical switch on morphology. *Cryst. Growth Des.* **6**, 197-201.

Falini, G., Fermani, S., Gazzano, M., and Ripamonti, A., 1998. Structure and morphology of synthetic magnesium calcite. *J. Mater. Chem.* **8**, 1061-1065.

Folk, R. L. and Land, L. S., 1975. Mg/Ca ratio and salinity - controls over crystallization of dolomite. *Bulletin-American Association of Petroleum Geologists* **59**, 60-68.

Grotzinger, J. P. and Knoll, A. H., 1999. Stromatolites in Precambrian carbonates: Evolutionary mileposts or environmental dipsticks? *Annu. Rev. Earth Planet. Sci.* **27**, 313-358.

Han, Y. J., Wysocki, L. M., Thanawala, M. S., Siegrist, T., and Aizenberg, J., 2005. Template-dependent morphogenesis of oriented calcite crystals in the presence of magnesium ions. *Angew. Chem.-Int. Edit.* **44**, 2386-2390.

Hardie, L. A., 1996. Secular variation in seawater chemistry: An explanation for the coupled secular variation in the mineralogies of marine limestones and potash evaporites over the past 600 my. *Geology* **24**, 279-283.

Kaczmarek, S. E. and Sibley, D. F., 2007. A Comparison of Nanometer-Scale Growth and Dissolution Features on Natural and Synthetic Dolomite Crystals: Implications for the Origin of Dolomite. *Journal of Sedimentary Research* **77**, 424-432.

Kashchiev, D., Vekilov, P. G., and Kolomeisky, A. B., 2005. Kinetics of two-step nucleation of crystals. *J. Chem. Phys.* **122**, 6.

Kelleher, I. J. and Redfern, S. A. T., 2002. Hydrous calcium magnesium carbonate, a possible precursor to the formation of sedimentary dolomite. *Mol. Simul.* **28**, 557-572.

Killian, C. E., Metzler, R. A., Gong, Y. U. T., Olson, I. C., Aizenberg, J., Politi, Y., Wilt, F. H., Scholl, A., Young, A., Doran, A., Kunz, M., Tamura, N., Coppersmith, S. N., and Gilbert, P., 2009. Mechanism of Calcite Co-Orientation in the Sea Urchin Tooth. *J. Am. Chem. Soc.* **131**, 18404-18409.

Land, L. S., 1998. Failure to precipitate dolomite at 25 degrees C from dilute solution despite 1000-fold oversaturation after 32 years. *Aquat. Geochem.* **4**, 361-368.

Lee, J. and Morse, J. W., 2010. Influences of alkalinity and pCO(2) on CaCO3 nucleation from estimated Cretaceous composition seawater representative of "calcite seas". *Geology* **38**, 115-118.

Levi, Y., Albeck, S., Brack, A., Weiner, S., and Addadi, L., 1998. Control over aragonite crystal nucleation and growth: An in vitro study of biomineralization. *Chem.-Eur. J.* **4**, 389-396.

Li, H., Xin, H. L., Muller, D. A., and Estroff, L. A., 2009. Visualizing the 3D Internal Structure of Calcite Single Crystals Grown in Agarose Hydrogels. *Science* **326**, 1244-1247.

Lumsden, D. N., 1979. Discrepancy between thin-section and X-Ray estimates of dolomite in limestone. *Journal of Sedimentary Petrology* **49**, 429-436.

Ma, Y., Cohen, S. R., Addadi, L., and Weiner, S., 2008. Sea urchin tooth design: An "All-Calcite" polycrystalline reinforced fiber composite for grinding rocks. *Advanced Materials* **20**, 1555-1559.

Meldrum, F. C. and Colfen, H., 2008. Controlling Mineral Morphologies and Structures in Biological and Synthetic Systems. *Chemical Reviews* **108**, 4332-4432.

Morse, J. W., Arvidson, R. S., and Luttge, A., 2007. Calcium carbonate formation and dissolution. *Chemical Reviews* **107**, 342-381.

Oaki, Y. and Imai, H., 2006. Nanoengineering in echinoderms: The emergence of morphology from nanobricks. *Small* **2**, 66-70.

Oaki, Y., Kotachi, A., Miura, T., and Imai, H., 2006. Bridged nanocrystals in biominerals and their biomimetics: Classical yet modern crystal growth on the nanoscale. *Adv. Funct. Mater.* **16**, 1633-1639.

Orme, C. A., Noy, A., Wierzbicki, A., McBride, M. T., Grantham, M., Teng, H. H., Dove, P. M., and DeYoreo, J. J., 2001. Formation of chiral morphologies through selective binding of amino acids to calcite surface steps. *Nature* **411**, 775-779.

Raz, S., Hamilton, P. C., Wilt, F. H., Weiner, S., and Addadi, L., 2003. The transient phase of amorphous calcium carbonate in sea urchin larval spicules: The involvement of proteins and magnesium ions in its formation and stabilization. *Adv. Funct. Mater.* **13**, 480-486.

Raz, S., Weiner, S., and Addadi, L., 2000. Formation of high-magnesian calcites via an amorphous precursor phase: Possible biological implications. *Advanced Materials* **12**, 38-42.

Reeder, R. J., 1992. Carbonates; growth and alteration microstructures. *Reviews in Mineralogy and Geochemistry* **27**, 380-424.

Robach, J. S., Stock, S. R., and Veis, A., 2006. Mapping of magnesium and of different protein fragments in sea urchin teeth via secondary ion mass spectroscopy. *J. Struct. Biol.* **155**, 87-95.

Rosen, M. R., Miser, D. E., and Warren, J. K., 1988. Sedimentology, mineralogy and isotopic analysis of pellet lake, Coorong region, South Australia. *Sedimentology* **35**, 105-122.

Sanchez-Roman, M., McKenzie, J. A., Wagener, A. D. R., Rivadeneyra, M. A., and Vasconcelos, C., 2009. Presence of sulfate does not inhibit low-temperature dolomite precipitation. *Earth Planet. Sci. Lett.* **285**, 131-139.

Schmidt, M., Xeflide, S., Botz, R., and Mann, S., 2005. Oxygen isotope fractionation during synthesis of CaMg-carbonate and implications for sedimentary dolomite formation. *Geochim. Cosmochim. Acta* **69**, 4665-4674.

Sethmann, I., Hinrichs, R., Worheide, G., and Putnis, A., 2006. Nano-cluster composite structure of calcitic sponge spicules - A case study of basic characteristics of biominerals. *J. Inorg. Biochem.* **100**, 88-96.

Skinner, H. C. W., 1963. Precipitation of calcian dolomites and magnesian calcites in the southeast of South Australia. *Am. J. Sci.* **261**, 449-472.

Song, R. Q. and Colfen, H., 2010. Mesocrystals-Ordered Nanoparticle Superstructures. *Advanced Materials* **22**, 1301-1330.

Spadafora, A., Perri, E., McKenzie, J. A., and Vasconcelos, C., 2010. Microbial biomineralization processes forming modern Ca:Mg carbonate stromatolites. *Sedimentology* **57**, 27-40.

Stephenson, A. E., DeYoreo, J. J., Wu, L., Wu, K. J., Hoyer, J., and Dove, P. M., 2008. Peptides Enhance Magnesium Signature in Calcite: Insights into Origins of Vital Effects. *Science* **322**, 724-727.

Tao, J., Zhou, D., Zhang, Z., Xu, X., and Tang, R., 2009. Magnesium-aspartate-based crystallization switch inspired from shell molt of crustacean. *Proc. Natl. Acad. Sci. U. S. A.* **106**, 22096-22101.

Vavouraki, A. I., Putnis, C. V., Putnis, A., and Koutsoukos, P. G., 2008a. An Atomic Force Microscopy study of the growth of calcite in the presence of sodium sulfate. *Chem. Geol.* **253**, 243-251.

Vavouraki, A. I., Putnis, C. V., Putnis, A., Oelkers, E. H., and Koutsoukos, P. G., 2008b. Macro- to nanoscale study of the effect of aqueous sulphate on calcite growth. *Mineral. Mag.* **72**, 141-144.

Vielzeuf, D., Floquet, N., Chatain, D., Bonnete, F., Ferry, D., Garrabou, J., and Stolper, E. M., 2010. Multilevel modular mesocrystalline organization in red coral. *Am. Mineral.* **95**, 242-248.

Wang, D. B., Wallace, A. F., De Yoreo, J. J., and Dove, P. M., 2009. Carboxylated molecules regulate magnesium content of amorphous calcium carbonates during calcification. *Proc. Natl. Acad. Sci. U. S. A.* **106**, 21511-21516.

Wasylenki, L. E., Dove, P. M., and De Yoreo, J. J., 2005a. Effects of temperature and transport conditions on calcite growth in the presence of Mg2+: Implications for paleothermometry. *Geochim. Cosmochim. Acta* **69**, 4227-4236.

Wasylenki, L. E., Dove, P. M., Wilson, D. S., and De Yoreo, J. J., 2005b. Nanoscale effects of strontium on calcite growth: An in situ AFM study in the absence of vital effects. *Geochim. Cosmochim. Acta* **69**, 3017-3027.

Weber, J. N., 1969. The incorporation of magnesium into the skeletal calcites of echinoderms. *Am. J. Sci.* **267**, 537-566.

Weiner, S., Levi-Kalisman, Y., Raz, S., and Addadi, L., 2003. Biologically formed amorphous calcium carbonate. *Connective Tissue Research* **44**, 214-218.

Wright, D. T. and Wacey, D., 2005. Precipitation of dolomite using sulphate-reducing bacteria from the Coorong Region, South Australia: significance and implications. *Sedimentology* **52**, 987-1008.

Zhou, L. and O'Brien, P., 2008. Mesocrystals: A New Class of Solid Materials. *Small* **4**, 1566-1574.

Raman spectroscopic characterization of the magnesium content of amorphous calcium carbonate based on spectral properties of the CO_3^{2-} Raman υ_1 stretch

Dongbo Wang, Laura Hamm, Robert J. Bodnar, and Patricia M. Dove

Department of Geosciences, Virginia Tech, Blacksburg VA 24061 USA

A manuscript in preparation for submission to *The Journal of Raman Spectroscopy*

1. Abstract

A series of Mg-bearing synthetic amorphous calcium carbonates (ACC) were characterized by Raman spectroscopy. The spectra show a systematic increase in υ_1 peak position from the control samples containing 0.0 mol % $MgCO_3$ to a sample that contains 43 mol % $MgCO_3$, best described by the function:

mol % $MgCO_3 = (\upsilon_1 - 1079.66) / 0.2017$

The Mg content is equally well predicted by υ_1 full width half maximum, best described by the function:

mol % $MgCO_3 = (\upsilon_1 - 23.40) / 0.1964$

Analysis of Raman data for ACC combined with insights from crystalline materials suggests the compositional dependencies arise from local metal-oxygen bonds. The calibrations described here provide a rapid laboratory-based means of determining Mg content of ACC, with the additional advantages of minimal sample preparation and a high lateral spatial resolution of approximately 1 micron.

2. Introduction

With the realization that amorphous calcium carbonates (ACC) are ubiquitous in calcification environments (ADDADI et al., 2003), recent studies are focusing on the formation and transformation of this reactive intermediate phase into crystalline products (WEINER et al., 2005). *In vitro* and *in vivo* investigations of biomineralization processes show that ACC acts as a 'moldable' precursor that is essential for the formation of complex hierarchical assemblages by providing a means of storing Ca^{2+} and CO_3^{2-} ions until such time that these constituents are needed for rapid mineralization (MELDRUM and COLFEN, 2008). As a result, carbonate biomineralizing systems are able to produce highly tuned functional materials of complex morphologies and enhanced mechanical properties.

One factor that influences stability and the pathway to crystal transformation of ACC is magnesium content (RAZ et al., 2003; RAZ et al., 2000). A recent study shows calcifying eukaryotic organisms use Mg to regulate the kinetics and pathway to ACC mineralization by slowing the amorphous to crystalline transformation (TAO et al., 2009). Yet, there are few reports of Mg contents of ACC from biological tissues or environmental samples, possibly because the community does not have a direct and

simple chemical probe with small spatial resolution that is sensitive only to ACC. One limitation to developing such a probe is the overwhelmingly strong signature of crystalline components observed using standard characterization techniques, such as XRD and aqueous analysis. Here we show that Raman spectroscopy can be used to determine the magnesium content of amorphous calcium carbonates. This technique offers significant advantages for ACC analysis as a rapid laboratory-based technique that requires minimal sample preparation and provides a high lateral spatial resolution (approximately 1 micron).

As a brief review, in addition to ACC there are three common anyhydrous phases of calcium carbonate: calcite, aragonite, and vaterite. There are also two hydrated crystalline phases, monohydrocalcite and ikaite. (TLILI et al., 2001). Calcite is the only crystalline form of calcium carbonate that accommodates substantial amounts of structural Mg (BISCHOFF et al., 1983; FALINI et al., 1998; FINCH and ALLISON, 2007), where Mg contents of up to 25 mol % are common. The crystalline carbonates typically exhibit six vibrational modes by Raman spectroscopy (**table 4.1**). Two are lattice modes that are observable in all crystalline carbonates, but not in ACC, a translation mode, and a higher frequency libation. The carbonate ion has four internal modes, although only two modes are known to be observable in ACC, the symmetric stretch (υ_1) and an antisymmetric stretch (υ_3) (TLILI et al., 2001).

A recent Raman spectroscopic study correlated the Mg concentration in calcite with peak position (RIVIDI et al., 2010). We use a similar approach to develop two calibrations relating either peak position or peak width at half maximum of the υ_1 peak to Mg content in amorphous calcium carbonate. Recognizing the absence of the lattice Raman modes in ACC, the strongest carbonate internal mode (υ_1 symmetric stretch) is characterized in this study. The resulting calibration holds promise for applications in heterogeneous biological and environmental specimens where the simultaneous identification of the phase and determination of its Mg content in amorphous calcium carbonate is desired.

3. Experimental

ACC was synthesized using the ammonium carbonate diffusion method (HAN and AIZENBERG, 2008; WANG et al., 2009). Samples containing from 0 to approximately 43

mol% $MgCO_3$ were produced using solution Mg/Ca ratios of 0 to 10 by holding [Ca^{2+}] constant at 25 mM ($CaCl_2$; 99.9%; Sigma) and adjusting Mg concentrations ($MgCl_2$; 99.9%; Sigma). Six mL of solution was pipetted into a glass Petri dish and then sealed in a desiccator with 0.6-0.7 g of ammonium carbonate salt [$(NH_4)_2CO_3$; Sigma]. For each solution Mg/Ca ratio, three replicates were prepared from single solutions for both compositional analysis and corresponding Raman analyses.

To prepare these materials, acid/peroxide washed glass slides were first placed in the glass petri dishes and then the solutions were introduced and incubated with ammonium carbonate. Each experiment was carefully monitored until the solutions became visually cloudy, after which the glass slides were removed and washed in anhydrous ethanol (99.5%; Sigma), dried and stored under vacuum until Raman analysis. The remaining solution with suspended ACC was prepared for chemical analysis by vacuum filtering the solutions through 0.2 μM nylon membranes (Whatman). The filtrate was then rinsed in ethanol and dried overnight under vacuum. The filter membranes were placed in 0.1M nitric acid (99.999%; Sigma) for 30 min and then removed prior to analysis by Inductively Coupled Plasma – Optical Emission Spectrometry (ICP-OES) using a Sectro CirOS VISION. The Mg and Ca concentrations were determined from calibration curves that were prepared from plasma-grade single element standards (SPEX CertiPreps).

The Mg and Ca molar concentrations of ACC measured by ICP-OES were converted into mol % $MgCO_3$ by assuming the stoichiometry (WANG et al., 2009):

$$yMg^{2+} + zCa^{2+} + y+z(CO_3^{2-}) = (Ca_zMg_y(CO_3)_{y+z}) \quad (1)$$

where mol % $MgCO_3$ is given by y/(y+z)*100. The resulting materials contained 0.0 to approximately 43 mol % $MgCO_3$.

Raman spectra were acquired for each of the corresponding samples using a JY Horiba (800 mm) LabRam HR spectrometer with a 632.81 nm He-Ne laser emitting 15 mW power at the source and focused through an Olympus 100x objective (N.A. = 0.9). The spectrograph had a 600 groves/mm grating. The detector was a Peltier cooled charged coupled device (CCD), optimally operating at -70°C. Three 180 sec spectra were collected and averaged for each of the samples analyzed and reported in this study.

To correct for drift and the non-linearity of the spectrometer to obtain true peak positions, two Ne emission lines at 914.90 cm^{-1} and 1371.26 cm^{-1} bounding the υ_1 peak of carbonate were collected simultaneously with the ACC spectrum as shown in **Fig 4.1**. The measured position of the υ_1 peak for carbonate was corrected using the known positions of the Ne lines according to:

(2)

$$\upsilon_{1,\ \text{corrected}}^{\text{carbonate}} = \frac{1}{2}\left\{\left[\upsilon_{1,\text{measured}}^{\text{carbonate}} + \left(\upsilon_{\text{standard}}^{\text{Ne},914.90} - \upsilon_{\text{measured}}^{\text{Ne},914.90}\right)\right] + \left[\upsilon_{1,\text{measured}}^{\text{carbonate}} + \left(\upsilon_{\text{standard}}^{\text{Ne},1371.28} - \upsilon_{\text{measured}}^{\text{Ne},1371.28}\right)\right]\right\}$$

As noted by other workers, over time Raman peaks will show some variability in measured position as the temperature in the laboratory, laser intensity, microscope focus, etc. vary (LIN et al., 2007a; LIN et al., 2007b). In our study, the Ne emission lines drifted to higher wavenumbers during the course of our experiments. We observed shifts of up to two wavenumbers over 12 hours, demonstrating the necessity to collect reference Raman lines simultaneously with the spectrum of the unknown (ACC) in order to compare and correlate Raman peak positions measured at different times within a single analytical session and in different analytical sessions. While the measured positions of the individual Ne lines vary during an analytical session for the reasons mentioned above, their relative positions remained fixed at 456.3 cm^{-1} ± .09, which suggests that the linear interpolation used in **equation 2** above is valid. It should also be noted that in an earlier study in this laboratory in which two other Ne lines were used for peak position calibration, a total of 231 analyses of the peak positions were made, and the measured position of the higher wavenumber Ne line varied from 2972.91 cm^{-1} to 2972.44 cm^{-1}, or a range of 0.47 cm^{-1}. Similarly, the measured position of the lower wavenumber Ne line ranged from 2851.86 cm^{-1} to 2851.40 cm^{-1}, for a total variation of 0.46 cm^{-1}. However, the difference in peak positions showed a range of only 0.05 cm^{-1}, with standard deviation of 0.012 cm^{-1} (LIN et al., 2007a; LIN et al., 2007b).

The Ne peak positions and the carbonate peak positions and widths were estimated using a summed Gaussian/Lorentzian peak-fitting routine after baseline corrections were made using JY Labspec version 4 software. A neon calibration lamp (model 6032; Newport instruments) positioned within the optical path of the Raman spectrometer made it possible to collect the Raman spectra for the Ne calibration lines

and for the ACC simultaneously.

4. Results

Representative morphologies of ACC materials that contain 0 - 43 mol % $MgCO_3$ are shown in **Figures 4.1A-D**. Mg-free ACC is comprised of discrete spherical particles (**Fig. 4.1A**). This morphology is maintained over the compositional range from 0 - 10 mol % $MgCO_3$ (solution Mg/Ca = 2) and perhaps higher (**Fig. 4.1B**). As the Mg content of ACC increases to 34 mol% $MgCO_3$ (**Fig. 4.1C**) (solution Mg/Ca = 5) and 43 mol% $MgCO_3$ (**Fig 4.1D**) (solution Mg/Ca = 10), the morphology evolves to produce a texture comprised of smaller aggregated particles. The change in morphology with increasing Mg content is consistent with a previous investigation that showed that ACC with $MgCO_3$ contents >20 mol % exist as coalesced particles (AJIKUMAR et al., 2005).

The corresponding Raman spectra for the ACC shown in **Fig. 4.1A-D** (**Fig. 4.1 E-H)** show systematic shifts in peak position, full width at half maximum, and intensity with increasing Mg content. These variations form the basis for the method reported here. These variations are also consistent with analyses of Mg-bearing calcites that show a decrease in peak intensity, peak broadening and red shifts in the Raman υ_1 carbonate symmetric stretch (BISCHOFF et al., 1985) with increasing Mg content.

To establish the correlation between Mg content of ACC and Raman spectral properties, we first determined the υ_1 peak position of the Mg-free control materials. The average corrected peak position of the υ_1 band is 1079.87 cm^{-1} +/- 0.04 cm^{-1}, where n = 3. These positions are in general agreement with the literature values of 1077 cm^{-1} in synthetic samples (TLILI et al., 2001) and 1085 cm^{-1} for biological samples (RAZ et al., 2000). We combined the control measurements of the υ_1 peak with the analyses of the Mg-bearing ACC materials to obtain the relationship shown in **Fig. 4.2.** A linear regression fit of the υ_1 peak position versus the measured $MgCO_3$ contents gives the following relationship:

$$\text{mol \% } MgCO_3 = \frac{\upsilon_1 - b}{m} \qquad (3)$$

where the b (intercept) and m (slope) parameters of **equation 3** are listed in **table 4.2**. Proportional error based upon Raman measurements gives the relationship (SCHROEDER et al., 2003):

$$\text{error mol \% } MgCO_3 = \upsilon_1 \sqrt{\left(\frac{s_m}{m}\right)^2 + \left(\frac{s_b}{b}\right)^2} \qquad (4)$$

and values for s_m and s_b are tabulated in **table 4.2**.

Further analysis of the data shows that the full width at half maximum (FWHM) of the υ_1 peak is related to peak position (**Fig. S.4.1**) and may provide an equally useful predictor of Mg content in ACC. For those workers who are unable to collect Raman spectra for peak position calibration lines (i.e., a Ne, Hg, or Ar lines, or the laser lines) simultaneously with the spectrum for the ACC owing their Raman microprobe configuration, the FWHM calibration might be preferred because that calibration is independent of peak position. The linear regression fit of FWHM versus mol % $MgCO_3$ in ACC (**Fig. 4.3** and **Table 4.2**) yields a coefficient of determination equal to 0.947, a value identical to that obtained for the peak position fit (**Fig. 4.2**).

5. Discussion

To understand the relationships between Raman spectral features and the Mg content of Mg-ACC shown in **Figs. 4.2 and 4.3**, we will first consider how Mg content influences the Raman spectra of calcite because the effect of Mg incorporation into crystalline calcite on the crystal structure is better understood. For compositions up 25 mol% $MgCO_3$, Mg substitutes for Ca in calcite and forms a solid solution (PAQUETTE and REEDER, 1990). Accommodation of the smaller Mg^{2+} ion causes significant disorder (strain) in the calcite structure (R-3c) resulting in a decrease in the average length of the metal-oxygen bond and a relative decrease in the length of the c-axis (FALINI et al., 1998). The decrease in the average metal-oxygen bond length is due to the presence of shorter Mg-O bonds (2.11 Å by EXAFS) compared to Ca-O bonds (2.39 Å by EXAFS) (POLITI et al., 2009; POLITI et al., 2006). Changes in metal-oxygen bond length have been attributed to differences in the polarizability of Ca versus Mg, which controls both the length of metal-oxygen bonds and Raman vibrational frequencies in the carbonate internal mode (BOOKER and BREDIG, 1973; WHITE, 1974b).

The effect of metal-oxygen bonds on carbonate vibrational modes is demonstrated in the υ_1 internal mode of free aqueous carbonate. This mode is predicted to be located at 1049 cm^{-1} (KLOPROGGE et al., 2002), but experimental values for this mode in concentrated alkali carbonate solutions are centered between 1064 and 1069 cm^{-1} (WHITE, 1974b). As an example of the change in υ_1 modes caused by metal – oxygen bonding, the υ_1 positions in calcite and magnesite are red shifted to 1085 cm^{-1} and 1094 cm^{-1}, respectively as compared to the free carbonate ion. The greater υ_1 red shift of magnesite compared to calcite is expected, as the shorter Mg – O bonds cause a greater change in carbonate C – O vibrational frequency.

For Mg-bearing calcites, Bischoff et al. (1985) report a continuous red shift and concurrent peak broadening for the carbonate υ_1 mode as $MgCO_3$ content increases from 0 to 25 mol %. This continuous red shift observed in Mg-bearing calcites is indicative of random substitution in solid solutions, where no phase separation occurs (WHITE, 1974a). Unlike the red shift, the trend in peak broadness was not directly attributed to the increase in the proportion of Mg – O bonds with increasing Mg substitution. Peak broadening is instead interpreted in terms of Mg – induced positional disorder of the carbonate ion, an explanation that has been challenged in recent studies of Mg – calcites (FALINI et al., 1998; ZOLOTOYABKO et al., 2010). Although the exact cause of peak broadening may be disputed, it remains clear that random substitution of Mg for Ca in the calcite lattice increases the distribution of metal – oxygen bond lengths, a phenomenon known to increase Raman peak widths (LIN et al., 2007b).

We observe that changes in the Mg content of ACC cause both a red shift and peak broadening of the υ_1 carbonate symmetric stretch. Structurally, the coordination environment about Ca in ACC is significantly decreased compared to calcite. The coordination number for Ca = 5-7 in ACC, as determined by EXAFS, while Ca coordination in calcite is 6(POLITI et al., 2006). The absence of lattice modes in the spectra of ACC and broadening of the υ_1 peak in pure (0 mol %) ACC (FWHM = 22.5 cm^{-1}), compared to calcite (FWHM = 4.1 cm^{-1}), suggests that ACC represents a disordered solid. Such an interpretation is also supported by X-ray total scattering experiments showing that ACC contains 'local order' but lacks measurable order beyond 15 Å (MICHEL et al., 2008).

Crystalline calcite, like all crystalline phases, exhibits long-range order, and the continuous shift in υ_1 peak position with increasing $MgCO_3$ content is considered to represent a substitutional solid solution (BISCHOFF et al., 1985). A similar interpretation cannot be entirely validated for ACC without evidence for an amorphous magnesium carbonate (AMC) end member. Assuming an AMC solid exists, the interpretation of the continuous υ_1 peak shift in Mg-calcite based upon increases in the number of Mg – O bonds with random Mg substitution can be applied to the peak shifts observed in Mg-bearing ACC. The increase in ACC υ_1 peak width from 22.5 cm^{-1} (0 mol % $MgCO_3$) to 32 cm^{-1} (43 mol % $MgCO_3$) can be explained by the presence of shorter Mg-O bonds in ACC. As in Mg-calcite, increasing the variability of metal – oxygen bond lengths would lead to υ_1 peak broadening.

We recognize that the υ_1 carbonate symmetric stretch shows evidence of some asymmetry that becomes more pronounced as the peak broadens with increasing Mg contents (above 30 mol%) (**Fig. 4.1C, D**). This observation suggests that the υ_1 peak could be a convolution of multiple discrete peaks, potentially invalidating the assumption that a solid solution model could explain the data. Recall that a single Gaussian-Lorentzian peak was used to fit the υ_1 peak. The data could also be fit to a more complex model that assumes the υ_1 peak consists of two (or more) discrete peaks and would suggest that high-Mg ACC is better described as a heterogeneous material comprised of both ACC and an amorphous magnesium carbonate, rather than as a solid solution. Circumstantial evidence suggests that ACC is heterogeneous at the nanometer scale, and that the initial stage of ACC formation is the formation of 2 nm prenucleation clusters that subsequently aggregate and coalesce (GEBAUER et al., 2008; POUGET et al., 2009). At high Mg concentrations, $MgCO_3$ prenucleation clusters may form and combine with $CaCO_3$ clusters. The resultant aggregates would contain discrete $MgCO_3$ and $CaCO_3$ domains and represent a physical mixture that would account for two υ_1 peaks. Although this is an intriguing and interesting concept, the possibility of a heterogenous amorphous Mg-Ca-CO_3 phase cannot be proven at this time and requires further investigation.

The findings herein show that the Mg content of ACC can be estimated based on the peak position or on the peak width of the Raman υ_1 carbonate symmetric stretch. The Raman technique thus provides a useful and reliable analytical tool that represents a

simple and direct probe for Mg-content in both synthetic and biological samples, without requiring extensive sample preparation beyond what is necessary for optical microscopy.

Table 4.1. Peak positions for Raman active modes in calcite, dolomite, magnesite from Bischoff et al.(1985) and Amorphous Calcium Carbonate (ACC) from this study.

Carbonate phase	Raman active modes	Peak position (cm^{-1})			
		Calcite	Dolomite	Magnesite	ACC
Lattice	Translation	154	175	213	-
	Libration	281	299	329	-
Internal	υ_1 (symmetric)	1085	1097	1094	1080
	υ_2 (out of plane bend)	1748	1750	1762	-
	υ_3 (anti-symmetric)	1434	1439	1444	-
	υ_4 (in plane bend)	711	724	738	714

Table 4.2. Parameters for calculating $MgCO_3$ content of ACC from carbonate υ_1 peak position or carbonate υ_1 FWHM, and errors associated with calculations (in cm^{-1}).

Measurement	m	b	s_m	s_b
υ_1 peak position	0.2017	1079.66	0.0087	0.243
υ_1 FWHM	0.1964	23.40	0.0084	0.235

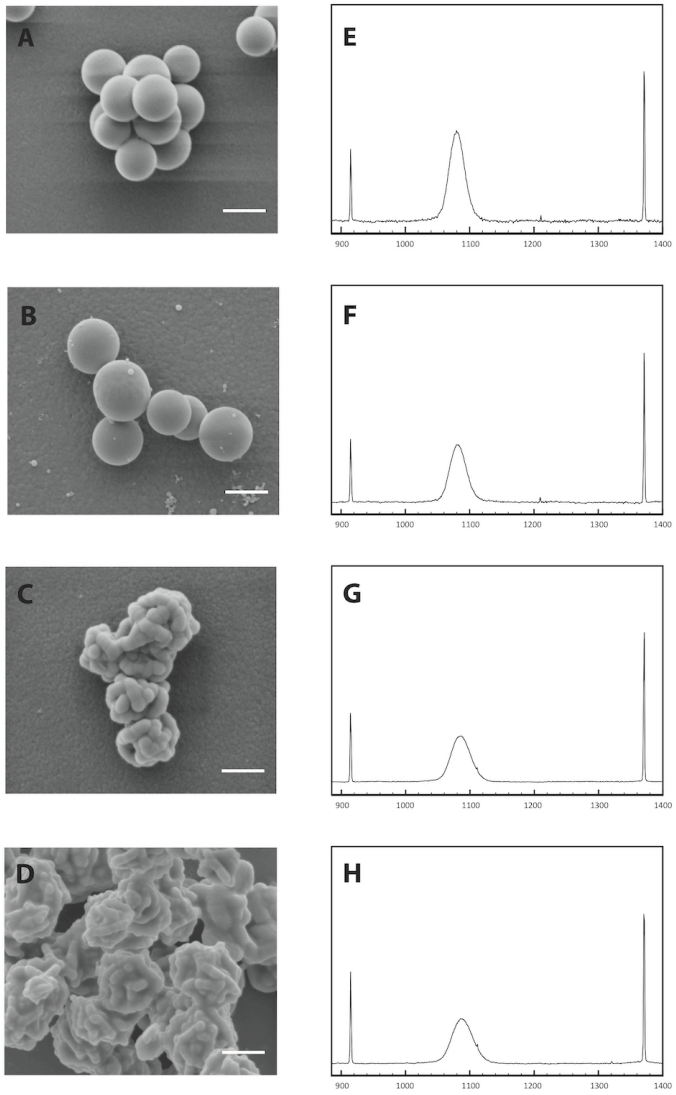

Fig. 4.1. SEM images of characteristic morphologies of amorphous calcium carbonate (ACC) precipitates and Raman spectra of carbonate υ_1 peak (center) and Ne emission lines at 914.90 cm^{-1} and 1371.26 cm^{-1}. (**A, E**) ACC containing 0 mol % $MgCO_3$. (**B, F**) ACC containing 10 mol % $MgCO_3$. (**C, G**) ACC containing 34 mol % $MgCO_3$. (**D,H**) ACC containing 43 mol % $MgCO_3$.

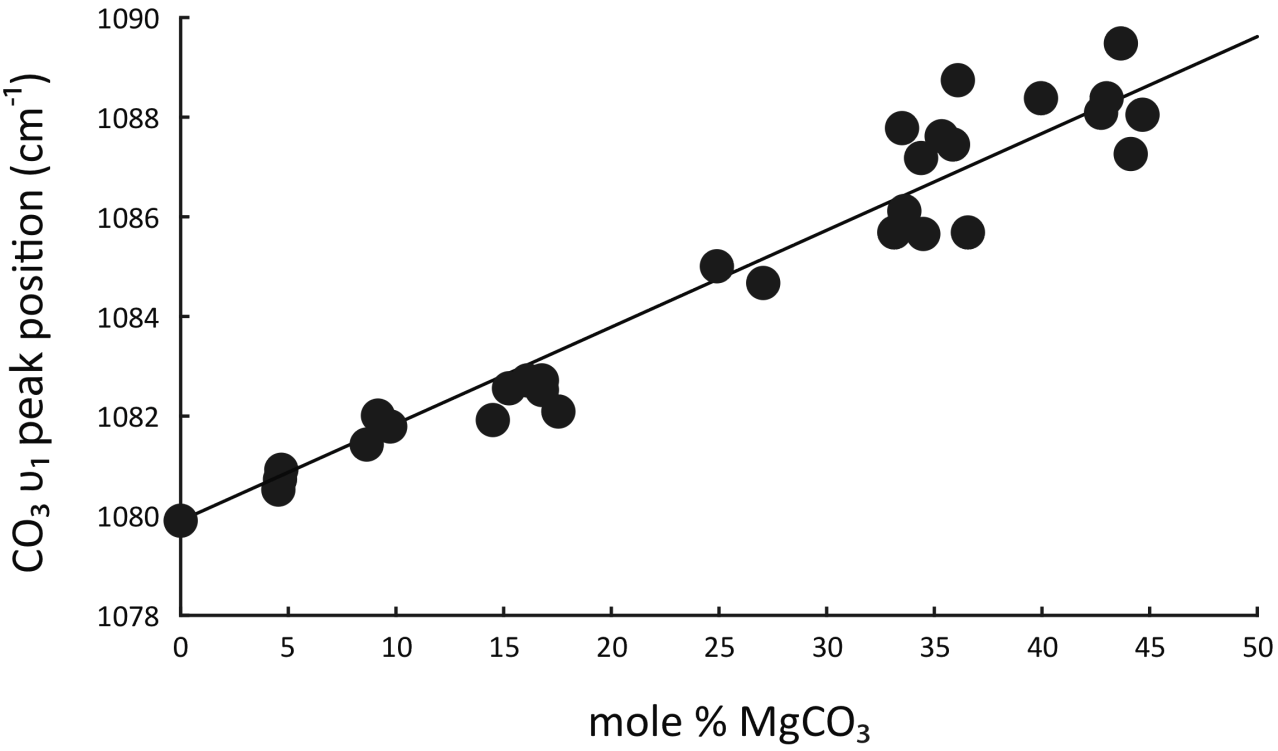

Fig. 4.2. Carbonate υ_1 peak position vs. $MgCO_3$ content of ACC (mol %). Line represents least squares fit with a R^2 value of 0.945.

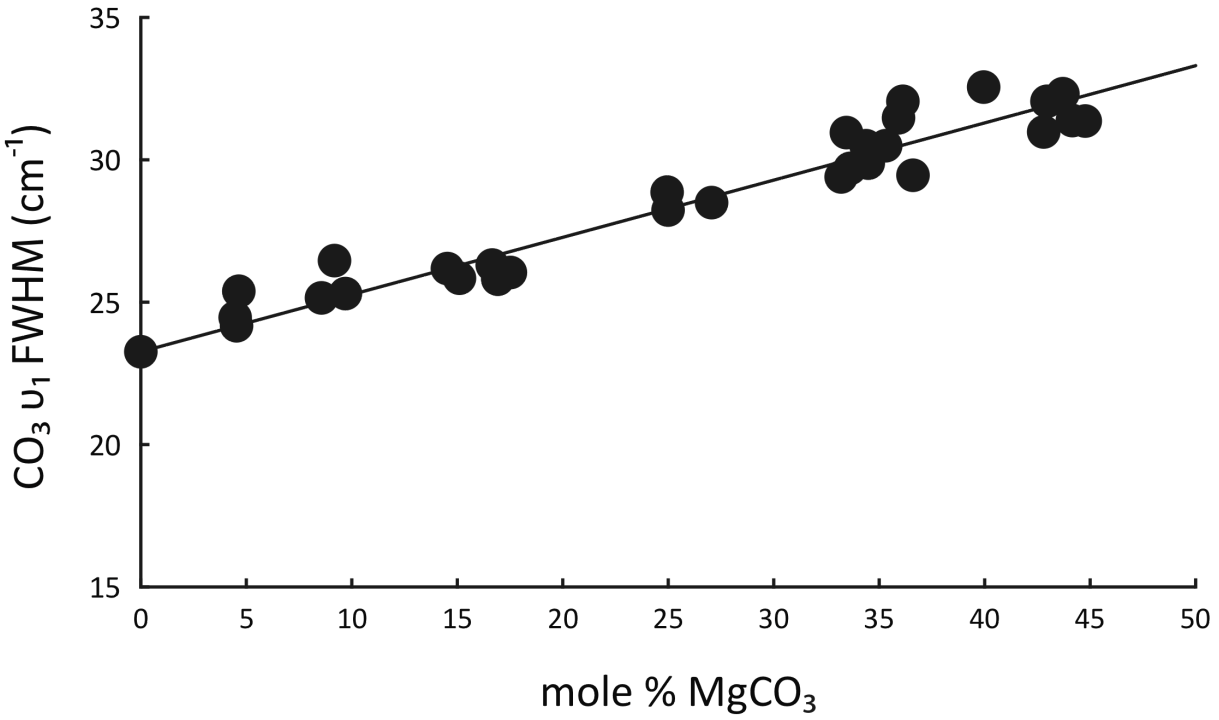

Fig. 4.3. Carbonate υ_1 full width at half maximum (FWHM) vs. $MgCO_3$ content (mol %) of ACC. Line represents least squares fit with an R^2 value of 0.946.

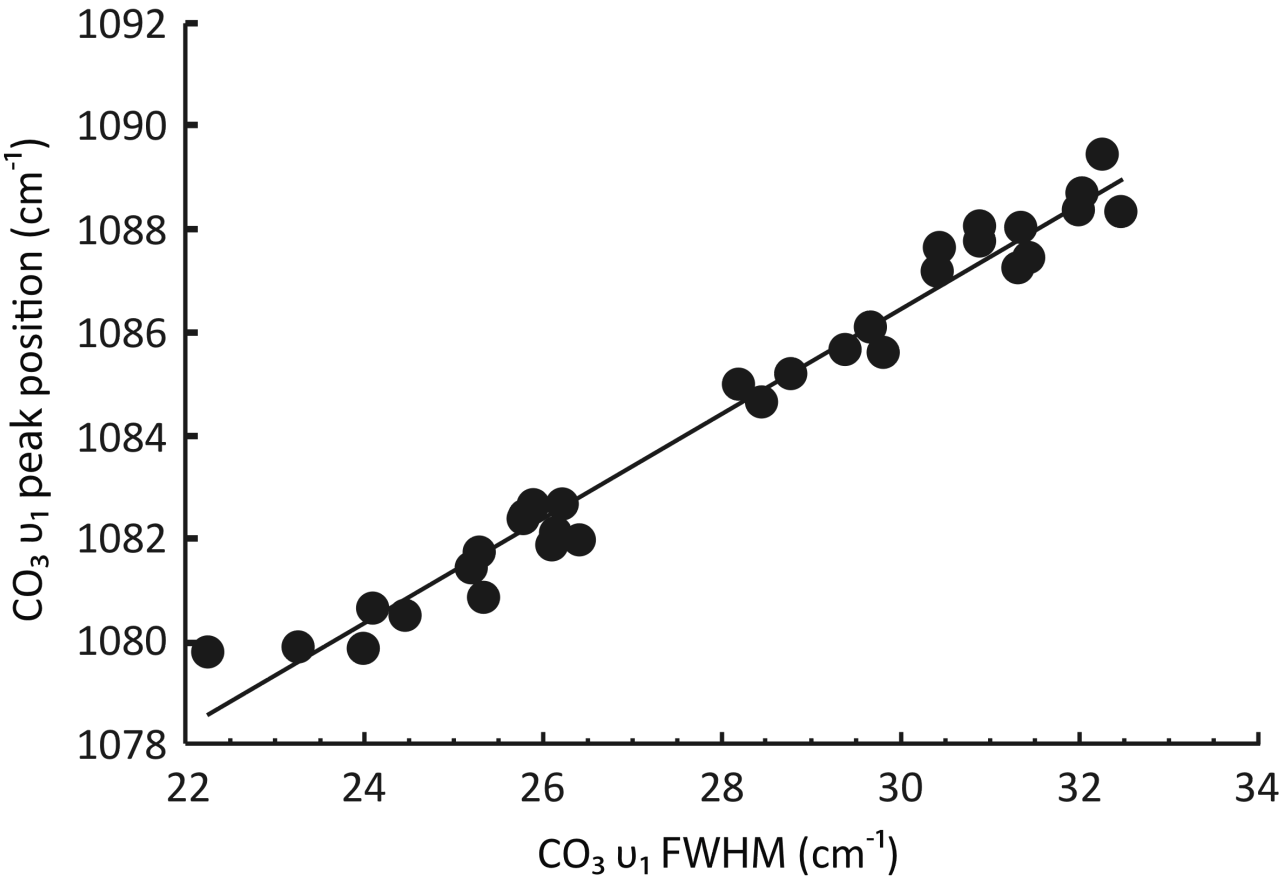

Fig. 4.S.1 Carbonate υ_1 peak position vs. carbonate υ_1 FWHM for ACC. Line represents least squares fit with an R^2 value of 0.975.

6. References

Addadi, L., Raz, S., and Weiner, S., 2003. Taking advantage of disorder: Amorphous calcium carbonate and its roles in biomineralization. *Advanced Materials* **15**, 959-970.

Ajikumar, P. K., Wong, L. G., Subramanyam, G., Lakshminarayanan, R., and Valiyaveettil, S., 2005. Synthesis and characterization of monodispersed spheres of amorphous calcium carbonate and calcite spherules. *Cryst. Growth Des.* **5**, 1129-1134.

Bischoff, W. D., Bishop, F. C., and Mackenzie, F. T., 1983. Biogenically produced magnesian calciteL inhomogeneities in chemical and phyiscal properties; comparison with synthetic phases. *Am. Mineral.* **68**, 1183-1188.

Bischoff, W. D., Sharma, S. K., and Mackenzie, F. T., 1985. Carbonate ion disorder in synthetic and biogenic magnesian calcite - A Raman spectral study. *Am. Mineral.* **70**, 581-589.

Booker, M. H. and Bredig, M. A., 1973. Significance of both polarizability and polarizing power of cations in nitrate vibrational spectra. *The Journal of Chemical Physics* **58**, 5319-5321.

Falini, G., Fermani, S., Gazzano, M., and Ripamonti, A., 1998. Structure and morphology of synthetic magnesium calcite. *J. Mater. Chem.* **8**, 1061-1065.

Finch, A. A. and Allison, N., 2007. Coordination of Sr and Mg in calcite and aragonite. *Mineral. Mag.* **71**, 539-552.

Gebauer, D., Volkel, A., and Colfen, H., 2008. Stable Prenucleation Calcium Carbonate Clusters. *Science* **322**, 1819-1822.

Han, T. Y. J. and Aizenberg, J., 2008. Calcium carbonate storage in amorphous form and its template-induced crystallization. *Chem. Mater.* **20**, 1064-1068.

Kloprogge, J. T., Wharton, D., Hickey, L., and Frost, R. L., 2002. Infrared and Raman study of interlayer anions CO32-, NO3-, SO42- and ClO4- in Mg/Al-hydrotalcite. *Am. Mineral.* **87**, 623-629.

Lin, F., Bodnar, R. J., and Becker, S. P., 2007a. Experimental determination of the Raman CH4 symmetric stretching (v(1)) band position from 1-650 bar and 0.3-22 degrees C: Application to fluid inclusion studies. *Geochim. Cosmochim. Acta* **71**, 3746-3756.

Lin, F., Sum, A. K., and Bodnar, R. J., 2007b. Correlation of methane Raman nu(1) band position with fluid density and interactions at the molecular level. *J. Raman Spectrosc.* **38**, 1510-1515.

Meldrum, F. C. and Colfen, H., 2008. Controlling Mineral Morphologies and Structures in Biological and Synthetic Systems. *Chemical Reviews* **108**, 4332-4432.

Michel, F. M., MacDonald, J., Feng, J., Phillips, B. L., Ehm, L., Tarabrella, C., Parise, J. B., and Reeder, R. J., 2008. Structural characteristics of synthetic amorphous calcium carbonate. *Chem. Mater.* **20**, 4720-4728.

Paquette, J. and Reeder, R. J., 1990. Single crystal X-Ray structure refinements of two biogenic magnesian calcite crystals. *Am. Mineral.* **75**, 1151-1158.

Politi, Y., Batchelor, D. R., Zaslansky, P., Chmelka, B. F., Weaver, J. C., Sagi, I., Weiner, S., and Addadi, L., 2009. Role of Magnesium Ion in the Stabilization of Biogenic Amorphous Calcium Carbonate: A Structure-Function Investigation. *Chem. Mater.* **22**, 161-166.

Politi, Y., Levi-Kalisman, Y., Raz, S., Wilt, F., Addadi, L., Weiner, S., and Sagi, I., 2006. Structural characterization of the transient amorphous calcium carbonate precursor phase in sea urchin embryos. *Adv. Funct. Mater.* **16**, 1289-1298.

Pouget, E. M., Bomans, P. H. H., Goos, J., Frederik, P. M., de With, G., and Sommerdijk, N., 2009. The Initial Stages of Template-Controlled CaCO3 Formation Revealed by Cryo-TEM. *Science* **323**, 1555-1458.

Raz, S., Hamilton, P. C., Wilt, F. H., Weiner, S., and Addadi, L., 2003. The transient phase of amorphous calcium carbonate in sea urchin larval spicules: The involvement of proteins and magnesium ions in its formation and stabilization. *Adv. Funct. Mater.* **13**, 480-486.

Raz, S., Weiner, S., and Addadi, L., 2000. Formation of high-magnesian calcites via an amorphous precursor phase: Possible biological implications. *Advanced Materials* **12**, 38-42.

Rividi, N., van Zuilen, M., Philippot, P., Menez, B., Godard, G., and Poidatz, E., 2010. Calibration of Carbonate Composition Using Micro-Raman Analysis: Application to Planetary Surface Exploration. *Astrobiology* **10**, 293-309.

Schroeder, P. A., Melear, N. D., and Pruett, R. J., 2003. Quantitative analysis of anatase in Georgia kaolins using Raman spectroscopy. *Appl. Clay Sci.* **23**, 299-308.

Tao, J., Zhou, D., Zhang, Z., Xu, X., and Tang, R., 2009. Magnesium-aspartate-based crystallization switch inspired from shell molt of crustacean. *Proc. Natl. Acad. Sci. U. S. A.* **106**, 22096-22101.

Tlili, M. M., Ben Amor, M., Gabrielli, C., Joiret, S., Maurin, G., and Rousseau, P., 2001. Characterization of CaCO3 hydrates by micro-Raman spectroscopy. *J. Raman Spectrosc.* **33**, 10-16.

Wang, D. B., Wallace, A. F., De Yoreo, J. J., and Dove, P. M., 2009. Carboxylated molecules regulate magnesium content of amorphous calcium carbonates during calcification. *Proc. Natl. Acad. Sci. U. S. A.* **106**, 21511-21516.

Weiner, S., Sagi, I., and Addadi, L., 2005. Choosing the crystallization path less traveled. *Science* **309**, 1027-1028.

White, W. B., 1974a. Order-disorder effects. In: Farmer, V. C. (Ed.), *The Infra-red Spectra of Minerals*. Mineralogical Society, London.

White, W. B., 1974b. The carbonate minerals. In: Farmer, V. C. (Ed.), *The Infra-red Spectra of the Minerals*. Mineralogical Society, London.

Zolotoyabko, E., Caspi, E. N., Fieramosca, J. S., Von Dreele, R. B., Marin, F., Mor, G., Addadi, L., Weiner, S., and Politi, Y., 2010. Differences between Bond Lengths in Biogenic and Geological Calcite. *Cryst. Growth Des.* **10**, 1207-1214.

Appendix A: ICP-OES compositional data (Chapter two)

Sample	Solution Mg/Ca	Mg/Ca solid
0.025M-ODA	1	0.500
0.025M-ODA	1	0.370
0.025M-ODA	1	0.418
0.025M-ODA	1	0.459
0.025M-ODA	1	0.511
0.025M-ODA	2	0.869
0.025M-ODA	2	0.673
0.025M-ODA	2	0.754
0.025M-ODA	2	0.695
0.025M-ODA	2	0.872
0.025M-ODA	3	0.768
0.025M-ODA	3	0.816
0.025M-ODA	3	1.220
0.025M-ODA	3	0.998
0.025M-ODA	3	0.991
0.025M-ODA	4	1.302
0.025M-ODA	4	1.252
0.025M-ODA	4	1.050
0.025M-ODA	4	1.230
0.025M-ODA	4	1.270
0.025M-ODA	5	1.305
0.025M-ODA	5	1.194
0.025M-ODA	5	1.118
0.025M-ODA	5	1.023
0.025M-ODA	5	1.016
0.025M-ODA	6	1.336
0.025M-ODA	6	1.385
0.025M-ODA	6	1.516
0.025M-TDA	2	0.165
0.025M-TDA	2	0.146
0.025M-TDA	2	0.138
0.025M-TDA	4	0.316
0.025M-TDA	4	0.269
0.025M-TDA	4	0.307
0.025M-TDA	5	0.344
0.025M-TDA	5	0.370
0.025M-TDA	5	0.347
0.025M-IDA	2	0.189
0.025M-IDA	2	0.177
0.025M-IDA	2	0.192
0.025M-IDA	4	0.380
0.025M-IDA	4	0.391
0.025M-IDA	4	0.347
0.025M-IDA	5	0.321
0.025M-IDA	5	0.326
0.025M-IDA	5	0.306

0.01M-ODA	1	0.158
0.01M-ODA	1	0.097
0.01M-ODA	1	0.085
0.01M-ODA	1	0.086
0.01M-ODA	2	0.161
0.01M-ODA	2	0.182
0.01M-ODA	2	0.181
0.01M-ODA	2	0.253
0.01M-ODA	3	0.279
0.01M-ODA	3	0.290
0.01M-ODA	3	0.306
0.01M-ODA	3	0.377
0.01M-ODA	4	0.400
0.01M-ODA	4	0.394
0.01M-ODA	4	0.380
0.01M-ODA	4	0.387
0.05M-ODA	1	0.719
0.05M-ODA	1	0.572
0.05M-ODA	1	0.755
0.05M-ODA	1	0.759
0.05M-ODA	1	0.619
0.05M-ODA	2	1.330
0.05M-ODA	2	1.461
0.05M-ODA	2	1.385
0.05M-ODA	2	1.521
0.05M-ODA	2	1.255
0.025M-Glu	1	0.289
0.025M-Glu	1	0.252
0.025M-Glu	1	0.271
0.025M-Glu	2	0.371
0.025M-Glu	2	0.378
0.025M-Glu	2	0.417
0.025M-Glu	3	0.592
0.025M-Glu	3	0.483
0.025M-Glu	3	0.528
0.025M-Glu	4	0.552
0.025M-Glu	4	0.691
0.025M-Glu	4	0.690
0.025M-Glu	5	0.843
0.025M-Glu	5	0.841
0.025M-Glu	5	0.791
0.025M-Glu	6	0.916
0.025M-Glu	6	0.837
0.025M-Glu	6	0.815
0.05M-Glu	1	0.438
0.05M-Glu	1	0.541
0.05M-Glu	1	0.512
0.05M-Glu	2	0.828
0.05M-Glu	2	0.819

0.05M-Glu	2	1.003
0.05M-Glu	3	1.267
0.05M-Glu	3	1.047
0.05M-Glu	3	1.152
0.05M-Glu	4	1.152
0.05M-Glu	4	1.330
0.05M-Glu	4	0.966
0.05M-Glu	5	1.682
0.05M-Glu	5	1.674
0.05M-Glu	5	1.540
0.05M-Glu	6	1.605
0.05M-Glu	6	1.634
0.05M-Glu	6	1.729
0.1M-Glu	1	0.748
0.1M-Glu	1	0.700
0.1M-Glu	1	0.712
0.1M-Glu	2	1.425
0.1M-Glu	2	1.262
0.1M-Glu	2	1.207
0.1M-Glu	3	1.974
0.1M-Glu	3	1.729
0.1M-Glu	3	1.840
0.1M-Glu	4	2.099
0.1M-Glu	4	2.424
0.1M-Glu	4	2.516
0.1M-Glu	5	2.823
0.1M-Glu	5	2.411
0.1M-Glu	5	2.507
0.1M-Glu	6	2.427
0.1M-Glu	6	2.214
0.1M-Glu	6	3.219
0.01M-Asp	1	0.090
0.01M-Asp	1	0.087
0.01M-Asp	1	0.101
0.01M-Asp	2	0.295
0.01M-Asp	2	0.379
0.01M-Asp	2	0.218
0.01M-Asp	3	0.219
0.01M-Asp	3	0.214
0.01M-Asp	3	0.239
0.01M-Asp	4	0.486
0.01M-Asp	4	0.304
0.01M-Asp	4	0.324
0.01M-Asp	5	0.369
0.01M-Asp	5	0.411
0.01M-Asp	5	0.461
0.01M-Asp	6	0.469
0.01M-Asp	6	0.466
0.01M-Asp	6	0.463

0.025M-Asp	1	0.197
0.025M-Asp	1	0.216
0.025M-Asp	1	0.205
0.025M-Asp	2	0.292
0.025M-Asp	2	0.272
0.025M-Asp	2	0.303
0.025M-Asp	3	0.449
0.025M-Asp	3	0.449
0.025M-Asp	3	0.359
0.025M-Asp	4	0.487
0.025M-Asp	4	0.538
0.025M-Asp	4	0.481
0.025M-Asp	5	0.542
0.025M-Asp	5	0.650
0.025M-Asp	5	0.521
0.025M-Asp	6	0.625
0.025M-Asp	6	0.599
0.025M-Asp	6	0.482
0.05M-Asp	1	0.537
0.05M-Asp	1	0.656
0.05M-Asp	1	0.556
0.05M-Asp	2	0.846
0.05M-Asp	2	0.742
0.05M-Asp	2	0.864
0.05M-Asp	3	0.918
0.05M-Asp	3	1.046
0.05M-Asp	3	0.819
0.05M-Asp	4	0.993
0.05M-Asp	4	1.039
0.05M-Asp	4	1.184
0.05M-Asp	5	1.117
0.05M-Asp	5	1.226
0.05M-Asp	5	1.208
0.05M-Asp	6	1.152
0.05M-Asp	6	1.365
0.05M-Asp	6	1.318
0.1M-Asp	1	0.617
0.1M-Asp	1	0.822
0.1M-Asp	1	1.026
0.1M-Asp	2	1.536
0.1M-Asp	2	1.812
0.1M-Asp	2	1.488
0.1M-Asp	3	1.735
0.1M-Asp	3	1.775
0.1M-Asp	3	2.194
0.1M-Asp	4	1.763
0.1M-Asp	4	2.003
0.1M-Asp	4	2.095
0.1M-Asp	5	2.041

0.1M-Asp	5	2.366
0.1M-Asp	5	2.568
0.1M-Asp	6	2.627
0.1M-Asp	6	2.813
0.1M-Asp	6	2.577
0.1M-Asp	0	0.002
0.025M-DTA	0	0.002
0.025M-DTA	0	0.000
0.025M-DTA	1	0.302
0.025M-DTA	1	0.401
0.025M-DTA	1	0.401
0.025M-DTA	2	0.429
0.025M-DTA	2	0.436
0.025M-DTA	2	0.584
0.025M-DTA	3	0.788
0.025M-DTA	3	0.828
0.025M-DTA	3	0.662
0.025M-DTA	4	1.025
0.025M-DTA	4	0.898
0.025M-DTA	4	0.988
0.025M-DTA	5	1.149
0.025M-DTA	5	1.173
0.025M-DTA	5	1.130
0.025M-DTA	6	1.509
0.025M-DTA	6	1.548
0.025M-DTA	6	1.555
0.025M-DTA	0	0.001
0.025M-MA	0	0.000
0.025M-MA	0	0.000
0.025M-MA	1	0.191
0.025M-MA	1	0.129
0.025M-MA	1	0.148
0.025M-MA	2	0.227
0.025M-MA	2	0.326
0.025M-MA	2	0.188
0.025M-MA	3	0.284
0.025M-MA	3	0.330
0.025M-MA	3	0.364
0.025M-MA	4	0.332
0.025M-MA	4	0.391
0.025M-MA	4	0.476
0.025M-MA	5	0.404
0.025M-MA	5	0.372
0.025M-MA	5	0.489
0.025M-MA	6	0.599
0.025M-MA	6	0.583
0.025M-MA	6	0.580

Appendix B: XRD data (Chapter three)

sample_id	std_Si	measured_Si	measured_Si k_alpha	delta_Si	104_peak	104_width	104 peak k_alpha	Corrected 104_peak	mol % Mg
100316-3-pure-2	28.44	28.48	28.46	-0.02	29.83	0.31	29.80	29.81	13.43
100316-3-pure-3	28.44	28.49	28.48	-0.04	29.95	0.37	29.92	29.91	16.43
100316-2-pure-3	28.44	28.44	28.42	0.02	29.75	0.29	29.72	29.78	12.33
100317-2-pure-4	28.44	28.47	28.46	-0.02	29.79	0.30	29.76	29.77	12.04
100317-1-pure-1	28.44	28.45	28.44	0.00	29.69	0.36	29.64	29.69	9.54
100318-1-pure-5	28.44	28.42	28.41	0.03	29.68	0.37	29.68	29.71	10.14
6-pure40C-100415-1	28.44	28.48	28.47	-0.03	30.54	0.49		30.51	35.62
6-pure40C-100415-2	28.44	28.43	28.42	0.02	30.51	0.46		30.53	36.08
6-pure40C-100415-6	28.44	28.46	28.45	-0.01	30.60	0.50	30.57	30.59	38.04
5-pure40C-100415-1	28.44	28.44	28.43	0.01	30.46	0.45	30.46	30.47	34.30
5-pure40C-100415-5	28.44	28.43	28.42	0.02	30.49	0.45		30.51	35.50
5-pure40C-100415-6	28.44	28.47	28.46	-0.02	30.54	0.47		30.52	35.85
4-pure40C-100415-2	28.44	28.43	28.42	0.02	30.51	0.49	30.51	30.52	35.94
4-pure40C-100415-3	28.44	28.45	28.44	0.00	30.57	0.48	30.56	30.57	37.54
4-pure40C-100415-6	28.44	28.44	28.43	0.01	30.67	0.49	30.63	30.68	40.90
100316-40C-10mM-1-005M-Asp-1	28.44	28.42	28.41	0.03	29.60	0.28	29.57	29.63	7.73
100316-40C-10mM-1-005M-Asp-2	28.44	28.42	28.41	0.03	29.58	0.28	29.54	29.61	7.18
100316-40C-10mM-1-005M-Asp-4	28.44	28.44	28.43	0.01	29.62	0.26	29.59	29.63	7.59
100316-40C-10mM-2-005M-Asp-1	28.44	28.44	28.43	0.01	29.71	0.22	29.69	29.73	10.74
100316-40C-10mM-2-005M-Asp-2	28.44	28.45	28.44	0.00	29.68	0.14	29.66	29.68	9.24
100316-40C-10mM-2-005M-Asp-5	28.44	28.43	28.42	0.02	29.68	0.19	29.66	29.70	9.84
100316-40C-10mM-3-005M-Asp-2	28.44	28.42	28.41	0.03	29.88	0.36	29.85	29.91	16.48
100316-40C-10mM-3-005M-Asp-3	28.44	28.44	28.43	0.01	30.17	0.72	30.13	30.17	24.94
100316-40C-10mM-3-005M-Asp-4	28.44	28.46	28.46	-0.02	29.97	0.35	29.96	29.96	18.06

100316-40C-10mM-4-005M-Asp-2	28.44	28.44	28.43	0.01	30.68	0.66		30.69	41.11
100316-40C-10mM-4-005M-Asp-3	28.44	28.45	28.44	0.00	30.33	0.91	30.30	30.30	28.90
100316-40C-10mM-4-005M-Asp-4	28.44	28.44	28.43	0.01	30.74	0.86	30.70	30.74	42.87
100316-40C-10mM-5-005M-Asp-1	28.44	28.41	28.40	0.04	30.80	0.83	30.76	30.83	45.78
100316-40C-10mM-5-005M-Asp-4	28.44	28.45	28.44	-0.01	30.81	0.90	30.78	30.80	44.83
100316-40C-10mM-5-005M-Asp-5	28.44	28.46	28.44	-0.01	30.77	0.86		30.77	43.75
100316-40C-10mM-6-005M-Asp-2	28.44	28.44	28.43	0.01	30.67	0.87	30.63	30.68	40.90
100316-40C-10mM-6-005M-Asp-3	28.44	28.45	28.43	0.01	30.65	0.78	30.62	30.66	40.21
100316-40C-10mM-6-005M-Asp-4	28.44	28.42	28.41	0.03	30.61	0.73	30.58	30.64	39.62
100316-40C-10mM-0-0025M-Asp-5	28.44		28.44	0.00	29.36			29.36	-0.78
100316-40C-10mM-1-0025M-Asp-1	28.44	28.43	28.43	0.01	29.64	0.31	29.61	29.65	8.46
100316-40C-10mM-1-0025M-Asp-3	28.44	28.43	28.42	0.02	29.62	0.28	29.59	29.64	7.96
100316-40C-10mM-1-0025M-Asp-4	28.44	29.62	28.43	0.01	29.62	0.32	29.58	29.63	7.62
100316-40C-10mM-2-0025M-Asp-1	28.44	28.43	28.43	0.01	29.71	0.24	29.68	29.72	10.65
100316-40C-10mM-2-0025M-Asp-2	28.44	28.46	28.45	-0.01	29.81	0.34	29.77	29.80	13.05
100316-40C-10mM-2-0025M-Asp-6	28.44	28.47	28.46	-0.02	29.76	0.27	29.73	29.74	11.34
100316-40C-10mM-3-0025M-Asp-1	28.44	28.45	28.45	-0.01	29.90	0.27	29.88	29.89	16.04
100316-40C-10mM-3-0025M-Asp-2	28.44	28.44	28.43	0.01	29.83	0.22	29.81	29.84	14.43
100316-40C-10mM-3-0025M-Asp-3	28.44	28.44	28.43	0.01	29.89	0.24	29.87	29.90	16.43
100316-40C-10mM-4-0025M-Asp-1	28.44	28.46	28.46	-0.02	31.05	0.81	30.97	31.03	51.97
100316-40C-10mM-4-0025M-Asp-4	28.44	28.47	28.46	-0.02	30.95	0.57	30.89	30.93	48.76
100316-40C-10mM-4-0025M-Asp-6	28.44	28.46	28.45	-0.01	30.63	1.06	30.67	30.62	38.97

100316-40C-10mM-5-0025M-Asp-1	28.44	28.45	28.44	0.00	30.82	0.66	30.79	30.82	45.24
100316-40C-10mM-5-0025M-Asp-3	28.44	28.45	28.44	0.00	30.81	0.64	30.81	30.81	45.16
100316-40C-10mM-5-0025M-Asp-6	28.44	28.44	28.43	0.01	30.42	0.91	30.39	30.43	32.97
100316-40C-10mM-6-0025M-Asp-2	28.44	28.47	28.46	-0.02	30.75	0.67	30.72	30.73	42.56
100316-40C-10mM-6-0025M-Asp-4	28.44		28.46	-0.02	30.82	0.76		30.80	44.77
100316-40C-10mM-6-0025M-Asp-6	28.44	28.49	28.47	-0.04	30.84	0.75	30.81	30.80	44.83
3-005M-SO4-40C-4	28.44	28.45	28.44	0.00	29.88	0.42		29.88	15.58
2-005M-SO4-40C-1	28.44	28.45	28.45	-0.01	29.83	0.41	29.80	29.82	13.81
2-005M-SO4-40C-2	28.44	28.45	28.44	-0.01	29.90	0.72	29.88	29.89	16.07
2-005M-SO4-40C-3	28.44	28.43	28.43	0.01	29.80	0.54	29.80	29.81	13.55
1-005M-SO4-40C-1	28.44	28.44	28.43	0.00	29.68	0.41	29.65	29.68	9.36
1-005M-SO4-40C-2	28.44	28.44	28.43	0.01	29.66	0.41	29.63	29.67	9.16
1-005M-SO4-40C-6	28.44	28.50	28.49	-0.05	29.71	0.39	29.68	29.65	8.49
0-005M-SO4-40C-2	28.44	28.46	28.45	-0.01	29.38	0.17	29.36	29.37	-0.34
0-005M-SO4-40C-5	28.44	28.45	28.43	0.01	29.36	0.16	29.33	29.37	-0.60
0-005M-SO4-40C-6	28.44	28.42	28.41	0.03	29.35	0.16	29.32	29.37	-0.36
3-0025M-SO4-40C-6	28.44	28.46	28.45	-0.01	29.94	0.19		29.92	17.06
2-0025M-SO4-40C-1	28.44	28.45	28.44	0.00	29.85	0.38	29.81	29.84	14.47
2-0025M-SO4-40C-3	28.44	28.43	28.42	0.02	29.84	0.38	29.81	29.86	14.91
2-0025M-SO4-40C-4	28.44	28.44	28.43	0.01	29.86	0.27	29.83	29.87	15.21
1-0025M-SO4-40C-2	28.44	28.44	28.43	0.01	29.72	0.50	29.69	29.73	10.84
1-0025M-SO4-40C-3	28.44	28.45	28.42	0.02	29.81	0.29	29.70	29.83	14.21
1-0025M-SO4-40C-4	28.44	28.43	28.42	0.02	29.72	0.36		29.74	11.24
0-0025M-SO4-40C-1	28.44	28.45	28.44	0.00	29.47	0.09	29.46	29.47	2.65
0-0025M-SO4-40C-6	28.44	28.45	28.45	-0.01	29.42	0.09	29.42	29.41	0.67
100809-4-0025M-SO4-40C-2	28.44	28.47	28.46	-0.02	30.91	0.75	30.87	30.88	47.28
100809-4-0025M-SO4-40C-4	28.44	28.45	28.43	0.00	30.64	0.55	30.59	30.59	38.22
100809-4-0025M-SO4-40C-5	28.44	28.44	28.43	0.01	30.81	0.86	30.79	30.82	45.36
100809-5-0025M-SO4-40C-1	28.44	28.46	28.45	-0.01	30.73	0.68	30.71	30.71	41.99

100809-5-0025M-SO4-40C-3	28.44	28.45	28.44	0.00	30.51	0.43	30.48	30.51	35.51
100809-5-0025M-SO4-40C-4	28.44	28.45	28.44	-0.01	30.58	0.42	30.56	30.57	37.40
100809-6-0025M-SO4-40C-1	28.44	28.45	28.44	-0.01	30.57	0.47	30.54	30.56	37.17
100809-6-0025M-SO4-40C-2	28.44	28.45	28.44	0.00	30.64	0.54	30.62	30.64	39.76
100809-6-0025M-SO4-40C-3	28.44	28.44	28.43	0.01	30.66	0.54	30.63	30.67	40.68
100809-4-005M-SO4-40C-1	28.44	28.46	28.45	-0.01	30.89	0.77	30.91	30.88	47.16
100809-4-005M-SO4-40C-5	28.44	28.40	28.39	0.05	30.85	0.91	30.82	30.90	47.85
100809-4-005M-SO4-40C-6	28.44	28.46	28.45	-0.01	30.71	0.59	30.69	30.71	41.74
100809-5-005M-SO4-40C-2	28.44	28.50	28.48	-0.04	30.72	0.57	30.69	30.67	40.69
100809-5-005M-SO4-40C-3	28.44	28.45	28.44	-0.02	30.69	0.49	30.67	30.68	40.81
100809-5-005M-SO4-40C-5	28.44	28.45	28.44	0.00	30.87	0.77	30.86	30.86	46.70
100809-6-005M-SO4-1	28.44	28.46	28.44	0.00	30.47	0.45	30.44	30.47	34.14
100809-6-005M-SO4-4	28.44	28.45	28.43	0.00	30.66	0.54	30.64	30.67	40.53

Appendix C: Raman data (Chapter four)

sample	914.9	v1	1371.28	corrected	width	Mg/Ca	mol % MgCO3
0.0-1	914.96	1079.98	1371.54	1079.82	22.23	0.000	0.000
0.0-2	915.13	1080.15	1371.54	1079.91	23.26	0.000	0.000
0.0-3	915.34	1080.32	1371.71	1079.89	24.00	0.000	0.000
1.0-1	914.95	1080.93	1371.34	1080.88	25.36	0.049	0.046
1.0-2	914.99	1080.63	1371.4	1080.53	24.46	0.048	0.045
1.0-3	915.08	1080.85	1371.45	1080.68	24.10	0.048	0.045
2.0-1	915.11	1081.94	1371.47	1081.74	25.30	0.107	0.097
2.0-2	915.14	1082.21	1371.47	1082.00	26.44	0.101	0.092
2.0-3	915.13	1081.68	1371.52	1081.45	25.22	0.095	0.086
3.0-1	915.12	1082.31	1371.49	1082.10	26.14	0.211	0.174
3.0-2	915.09	1082.74	1371.48	1082.55	25.87	0.180	0.152
3.0-3	915.14	1082.17	1371.53	1081.93	26.12	0.170	0.145
4.0-1	915.17	1082.91	1371.55	1082.64	25.92	0.203	0.169
4.0-2	915.15	1082.93	1371.56	1082.67	26.25	0.199	0.166
4.0-3	915.16	1082.72	1371.53	1082.47	25.84	0.204	0.169
5.0-1	915.08	1084.88	1371.5	1084.68	28.49	0.371	0.271
5.0-2	915.1	1085.41	1371.49	1085.21	28.81	0.332	0.249
5.0-3	915.05	1085.17	1371.46	1085.01	28.24	0.332	0.249
6.0-1	914.93	1087.81	1371.31	1087.78	30.95	0.504	0.335
6.0-2	914.9	1085.68	1371.28	1085.68	29.43	0.497	0.332
6.0-3	914.96	1087.22	1371.31	1087.18	30.46	0.525	0.344
7.0-1	915.87	1087.06	1372.21	1086.11	29.71	0.507	0.336
7.0-2	916.34	1086.98	1372.52	1085.64	29.85	0.527	0.345
7.0-3	916.53	1087.23	1372.7	1085.71	29.43	0.576	0.366
8.0-1	916.71	1090.45	1372.89	1088.74	32.10	0.565	0.361
8.0-2	916.72	1089.19	1372.95	1087.45	31.49	0.561	0.359
8.0-3	916.74	1089.39	1372.98	1087.62	30.49	0.546	0.353
9.0-1	916.75	1089.85	1372.99	1088.07	30.94	0.749	0.428
9.0-2	915.16	1088.24	1371.42	1088.04	31.40	0.808	0.447
9.0-3	915.22	1087.51	1371.47	1087.26	31.36	0.792	0.442
10.0-1	915.37	1089.86	1371.61	1089.46	32.32	0.775	0.437
10.0-2	915.45	1088.86	1371.72	1088.37	32.06	0.755	0.430
10.0-3	915.43	1088.86	1371.72	1088.38	32.56	0.666	0.400